Mid-infrared Dual Comb Spectroscopy with Asynchronous Optical Parametric Oscillators

Oguzhan Kara

Submitted for the degree of Doctor of Philosophy

Heriot-Watt University

School of Engineering and Physical Sciences

January 2018

ABSTRACT

Dual-comb spectroscopy (DCS) is a novel approach that uses asynchronous broadband coherent sources to achieve Fourier-transform-like spectroscopy but with no moving parts and at kHz acquisition rates. To date, fully resolved and accurate dual-comb spectrometers have been demonstrated in the near-infrared and applied to broadband spectroscopy for precise measurement of molecular centerlines, spectral lidar, and greenhouse gases from the near- to mid-IR.

This thesis describes DCS with asynchronous optical parametric oscillators and explores their applications in rapid, high-resolution broadband spectroscopy in the mid-infared. Initially a dual-comb spectrometer was designed with two identical optical parametric oscillators (OPOs) pumped by two identical Yb:fibre lasers and its stability performance was characterized measuring relative intensity noise. First experiments were accomplished by using free-running independent MgO:PPLN based OPOs with a repetition-rate difference of 500 Hz, achieving resolutions of 0.2 cm^{-1} across a wavelength range 3.1 to 3.5 μm; an absolute wavelength calibration technique was employed to allow registration and averaging of consecutively acquired dual-comb spectra. Then experiments were repeated with a dual-comb source for the spectral fingerprint region based on a pair of entirely free-running OPOs, each pumped by a 1-μm femtosecond laser and utilizing the new gain medium orientation-patterned gallium phosphide (OPGaP) to produce broadband idler pulses tunable from 6–8 μm. Methane absorption spectroscopy in the deep infrared region was demonstrated with the same wavelength calibration approach for both dual-comb spectrometers, leading to a high quality and low-noise absorbance measurement with spectral coverage simultaneously spanning the methane P, Q and R branches in good agreement with the Hitran database.

DECLARATION STATEMENT

(Research Thesis Submission Form should be placed here)

Acknowledgements

The work presented in this thesis would not have succeeded without the help and support of many people for whom these acknowledgements would not be enough to appreciate at all.

Firstly, I would like to thank to my supervisor, Derryck T. Reid for his precious mentorship and advising all the way through my PhD story. He gave me a chance to work for such an exciting work at this stimulating and vibrant institute. His limitless knowledge and enthusiasm guided me with endless patience for my all hardest time during this work. Having such a mentor is a big opportunity that dare to push my knowledge forward. So I always appreciate his support and guidance.

I am also grateful to Richard A. McCracken who helped and guided me for not just about optical parametric oscillators but also everything at HWU. He is an amazing person that always answers my endless questions patiently.

I am also thankful to Carl Farrell for his all remarkable discussions and advices about fibre lasers. I admired his skills and I definetely learnt many valuable tips on fibre laser from his experiences.

I would also like to thank to Dr. Tom Gardiner from NPL for all discussions and suggestions about mid-infrared spectroscopy and Prof. Robert R. J. Maier who helped me to fill gas cell many times.

My colleagues, Marius Rutkauskas and Luke Maidment whom I shared same lab with pleasure over three years deserve my thanks as well. Our motivating conversations and travels were always unforgattable. I feel very lucky to accompany you in this adventure.

My other colleagues, Hollie Wright, Jake Charsley, Jinghua Sun and Toby Mitchell who joined the abroad short while ago brought dynamism and coziness. My thanksgiving is with them for being a large part of such an awesome team.

Lastly, I deeply feel appreciation for my family who support me with their hope and love continuously. I am proud of being a member of such a great family and I always bear responsibility of deserving their love deeply.

CONTENTS

LIST OF PUBLICATIONS BY THE CANDIDATE

Peer-reviewed journal articles

O. Kara, Z. Zhang, T. Gardiner, and D. T. Reid, "Dual-comb mid-infrared spectroscopy with free-running oscillators and absolute optical calibration from a radio-frequency reference," Opt. Express 25, 16072-16082 (2017).

O. Kara, L. Maidment, T. Gardiner, P. G. Schunemann and D. T. Reid, "Broadband Dual-comb spectroscopy in the spectral fingerprint region," arXiv:1706.08445 (2017).

O. Kara, L. Maidment, T. Gardiner, P. G. Schunemann and D. T. Reid, "Broadband Dual-comb spectroscopy in the spectral fingerprint region," Opt. Express 25, 32713-32721 (2017)

Peer-reviewed conference articles

O. KARA, Z. Zhang, T. Gardiner, and D. T. Reid, "Broadband Mid-Infrared Dual Comb Spectroscopy with Independent Asynchronous Optical Parametric Oscillators," in *Conference on Lasers and Electro-Optics* (Optical Society of America) (2016)

J. Sun, R. A. McCracken, Z. Zhang, K. Balskus, L. Maidment, **O. Kara**, K. Sun, J. Li, Z. Lin, J. Sun, Z. Zhang, L. Jin, and D. Reid, "Optical Frequency Combs Based on Femtosecond Optical Parametric Oscillators," in *The 8th International Symposium on Ultrafast Phenomena and Terahertz Waves*, (Optical Society of America) (2016)

O. Kara, Z. Zhang, T. Gardiner, and D. T. Reid, "Dual-comb mid-infrared spectroscopy with free-running oscillators and complete optical calibration from a radio-frequency reference," in *Conference on Lasers and Electro-Optics* (Optical Society of America) (2017).

O. Kara, Z. Zhang, T. Gardiner, and D. T. Reid, "Dual-comb mid-infrared spectroscopy with free-running oscillators and complete optical calibration from a radio-frequency reference," in *Conference on Lasers and Electro-Optics - Europe* (Optical Society of America) (2017).

Chapter 1 – Introduction

1.1 Motivation

Molecular spectroscopy has made significant leaps forward in guiding us to examine the characteristics of materials in the gas, liquid and solid phases since the discovery of the laser. Before this invention incoherent sources were employed in combination with interferometric methods, to investigate electronic, vibrational and rotational transitions from the UV to MIR region. At this point, lasers become prominent for sensing molecules with high sensitivity and selectivity, taking advantage of their high spectral resolution and the ability to make measurements over long optical path lengths due to their excellent spatial coherence properties.

Even before the advent of laser spectroscopy, the Fourier transform spectrometer (FTS) has become the instrument of choice for precision spectroscopic measurements and the most efficient approach to record highly consistent, well resolved spectra over a wide wavelength range, covering the UV, visible, near- and MIR wavelength regions. The FTS dominates the field of spectroscopy as the versatility of this technique has proved highly appropriate for the determination of the structure of molecules [1-4], the quantitative analysis of complex mixtures [5-7], and the investigation of dynamic systems [8,9]. However, the FTS has a number of drawbacks such that measurement times are limited by the speed of the scanning mirror, and the incoherent sources typically used in FTS have low-brightness which limits sensitivity with a limited optical path length.

As optical frequency combs have emerged as sources which can enable very precise measurements, revolutionising optical metrology, the FTS has been combined with optical frequency comb technology by means of a technique called dual-comb spectroscopy (DCS). Frequency comb based FTS makes it possible to reach high sensitivity, by taking advantage of the brightness and robustness of laser sources. Unlike FTS, long averaging times are not necessary to obtain high signal-to-noise ratios, and well-resolved molecular spectra are acquired within tens of milliseconds. Despite such advantages, there remains a challenge to generate stable MIR to LWIR frequency combs with the wavelength coverage of an incoherent source (2–20 μm) and sufficient optical power. The MIR wavelength region is needed to identify molecules' fingerprints with high selectivity and sensitivity. Another issue with standard FTS is that it is sensitive to mechanical perturbations of the scanning mirror during the time that the spectral data is

recorded. The Michelson interferometer within the spectrometer experiences the modulation of input radiation at a frequency equal to the product of the wavenumber of the radiation and the constant optical path difference (OPD) velocity associated with the moving mirror. Particularly with incoherent sources, mechanical disturbances can cause a misalignment of the wavefronts which distorts the spectrum [10,11].

1.2 Thesis aim

In response to the limitations of the FTS, the optical parametric oscillator frequency comb (OPO-FC) presents an opportunity to overcome such issues. Because the output from an OPO has a broad infrared bandwidth and the spatial coherence of a laser, it has the potential to permit free-space propagation over long distances. Thus, an OPO brings an opportunity for implementing free-space FTIR across very long measurement paths and understanding the characteristic absorption lines of many chemical species from a single measurement.

To overcome the constraints of systematic errors and low speed associated with mechanically scanned FTS, the technique of DCS is considered to implement a robust, no-moving-parts FTIR system. The concept is based on using two asynchronous, phase-coherent mid-IR pulse sequences derived from identical OPOs to mimick a mechanically-scanned optical delay line. Uniquely, this approach offers the means to acquire a high resolution spectrum (< 0.1 cm^{-1}) in only a few milliseconds. This technique also has great potential to provide excellent spectral discrimination and able to simultaneously probe for multiple gases, and even atmospheric sensing for greenhouse gases.

1.3 Thesis outline

The research presented in this thesis demonstrates mid-infrared dual-comb spectroscopy with asynchronous OPOs across a wavelength range from 3 to 8 μm. This describes both the technical construction of two identical asynchronous OPOs pumped by Yb:fibre lasers and the implementation of this system for infrared gas spectroscopy.

Chapter 2 describes the fundamental principles and state of art of optical frequency comb molecular spectroscopy with Fourier transform spectrometers. Then dual-comb

spectroscopy is discussed in the context of the progress of their wavelength range and spectral resolution. This discussion also introduces comparisons of different light sources that are used to extend the wavelength region through the mid-infrared.

Chapter 3 presents design concepts of the first generation MgO:PPLN based OPOs pumped by home made Yb:fibre lasers to deliver a broad wavelength range, covering from 2.7 μm to 4.2 μm, and their passive and active stability are compared to understand such novelty and robustness for gas spectroscopy in mid-infrared region.

Chapter 4 demonstrates how dual-comb spectroscopy is accomplished with asynchronous MgO:PPLN based OPOs. Their limitations are analyzed with the stabilized OPOs being used for gas absorption spectroscopy of methane. Using this system a novel absolute wavelength calibration technique is introduced to overcome some of the identified limitations. Both measurement approaches are discussed and compared in terms of their spectroscopic results. This chapter has also been published in [12].

Chapter 5 describes the extension of DCS to the long-wave infrared region through the development of a dual-comb spectrometer based on orientation-patterned gallium phosphide (OPGaP) to access the fingerprint region of molecules. The gas absorption spectroscopy of methane and water vapor are performed with these second generation OPOs in the 6 - 8 μm region and the spectroscopic performance of this system is investigated. This chapter has been published in [13] and [14].

Chapter 6 concludes this thesis and develops a point of view for future directions of mid-infrared dual-comb spectroscopy using OPOs.

1.4 References

1. P. L. Richards, "High-Resolution Fourier Transform Spectroscopy in the Far-Infrared," J. Opt. Soc. Am. 54, 1474-1484 (1964).

2. Pines, M. G. Gibby, and J. S. Waugh. "Proton-enhanced nuclear induction spectroscopy. A method for high resolution NMR of dilute spins in solids." *The Journal of Chemical Physics* 56.4, 1776-1777 (1972).

3. Steven C. Beu, Michael W. Senko, John P. Quinn, Francis M. Wampler, and Fred W. McLafferty. "Fourier-transform electrospray instrumentation for tandem high-

resolution mass spectrometry of large molecules." *Journal of the American Society for Mass Spectrometry* 4, no. 7, 557-565 (1993).

4. Witold K. Surewicz, Henry H. Mantsch, and Dennis Chapman, "Determination of protein secondary structure by Fourier transform infrared spectroscopy: a critical assessment." *Biochemistry* 32.2: 389-394 (1993).

5. John Strassburger, and Miklos M. Breuer. "Quantitative Fourier transform infrared spectroscopy of oxidized hair." *J. Soc. Cosmet. Chem* 36, no. 1, 61-74 (1995).

6. Jose Luis R. Arrondo, Arturo Muga, Jose Castresana, and Felix M. Goñi. "Quantitative studies of the structure of proteins in solution by Fourier-transform infrared spectroscopy." *Progress in biophysics and molecular biology* 59, no. 1, 23-56 (1993).

7. Z. Malik, , D. Cabib, R. A. Buckwald, A. Talmi, Y. Garini, and S. G. Lipson. "Fourier transform multipixel spectroscopy for quantitative cytology." *Journal of microscopy* 182, no. 2, 133-140 (1996).

8. Dale McMorrow, and William T. Lotshaw. "Intermolecular dynamics in acetonitrile probed with femtosecond Fourier-transform Raman spectroscopy." *The Journal of Physical Chemistry* 95, no. 25, 10395-10406 (1991).

9. Reginald H. Wilson, Andrew C. Smith, Marta Kačuráková, Paul K. Saunders, Nikolaus Wellner, and Keith W. Waldron. "The mechanical properties and molecular dynamics of plant cell wall polysaccharides studied by Fourier-transform infrared spectroscopy." *Plant Physiology* 124, no. 1, 397-406 (2000).

10. Peter R. Griffiths, James A. de Haseth, Fourier transform infrared spectrometry, Wiley, 2nd edition (2007).

11. Luca Palchetti and Davide Lastrucci, "Spectral noise due to sampling errors in Fourier-transform spectroscopy," Appl. Opt. 40, 3235-3243 (2001).

12. O. Kara, Z. Zhang, T. Gardiner, and D. T. Reid, "Dual-comb mid-infrared spectroscopy with free-running oscillators and absolute optical calibration from a radio-frequency reference," Opt. Express 25, 16072-16082 (2017).

13. O. Kara, L. Maidment, T. Gardiner, P. G. Schunemann and D. T. Reid, "Broadband Dual-comb spectroscopy in the spectral fingerprint region," arXiv:1706.08445 (2017).

14. O. Kara**,** L. Maidment, T. Gardiner, P. G. Schunemann and D. T. Reid, "Broadband Dual-comb spectroscopy in the spectral fingerprint region," Opt. Express 25, 32713-32721 (2017).

Chapter 2 – Optical Frequency Comb Spectroscopy

Optical frequency combs, a form of ultrashort pulse laser experimentally achieving a sustained fixed phase relationship across a broad spectrum of frequencies, have made it possible to accurately measure optical frequencies with a precision much higher than any other techniques [1,2].

Optical frequency combs are coherent light sources with a broad spectrum consisting of a series of discrete, equally spaced narrow lines whose absolute frequency can be measured to within the accuracy of an atomic clock [3]. Frequency metrology has been well-developed to deliver numerous unexpected opportunities in other fields such as astronomy and attosecond science in the near-infrared and visible domains (Fig. 2.1).

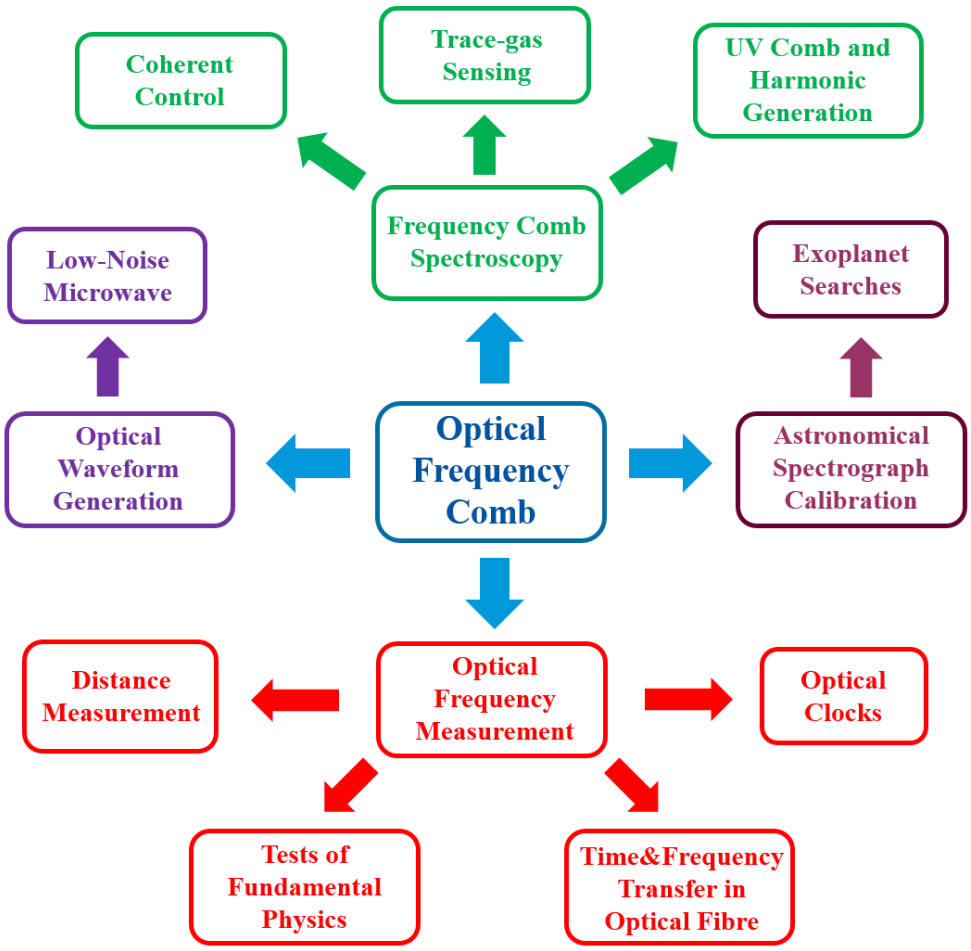

Figure 2.1: The broad range of optical frequency comb applications.

2.1 Fundamentals of optical frequency combs

A mode-locked laser delivering a spectrum that consists of a discrete, regularly spaced series of sharp lines in the frequency domain, is known as a frequency comb. However, mode-locked lasers and their applications are generally discussed in the time domain. To understand the connection between the time-domain and frequency-domain descriptions of the pulse train from a mode-locked laser, the carrier-envelope phase of a pulse train is introduced here as a primary concept.

The decomposition of the pulses into an envelope function $E(t)$ is superimposed on a continuous carrier wave with frequency ω_c, so that the electric field of the pulse is given:

$$\boldsymbol{E(t)} = \hat{\mathrm{E}}(\boldsymbol{t})\boldsymbol{e}^{\boldsymbol{i}\omega_c \boldsymbol{t}} \tag{2.1}$$

The spectrum of a single pulse is formed by the Fourier transform of $E(t)$ and centered at the optical frequency of its carrier, ω_c. The carrier-envelope phase, ϕ_{ce}, is the phase shift between the peak of the envelope and the closest peak of the carrier wave, as illustrated in Fig. 2.2. The number of emitted pulses per second, or the inverse temporal pulse spacing is described as the pulse repetition rate frequency, $f_{rep}=1/T_{pulse}$. Here, the frequency comb is basically the optical spectrum of the pulse train if the pulse train is regular and the pulses are mutually coherent with a fixed phase interval separating adjacent pulses.

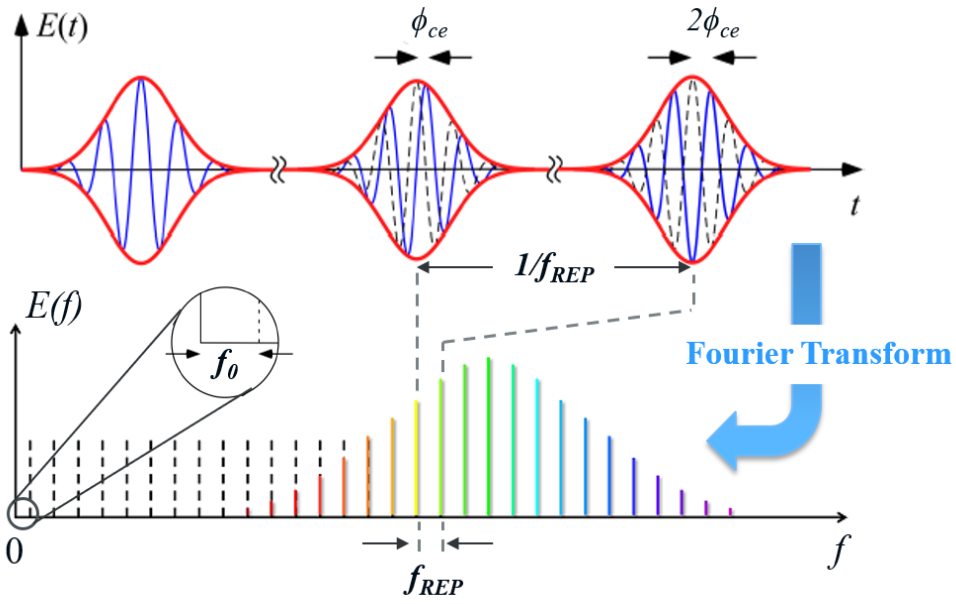

Figure 2.2: The optical pulse train in the time and frequency domains.

The optical frequencies f_n of the comb lines can be written as

$$f_n = f_0 + nf_{rep} \tag{2.2}$$

where n is an integer indexing the comb line, and f_0 is the comb offset due to pulse-to-pulse phase shift. The offset frequency f_0 is related to the evolution of the carrier-envelope phase, $\emptyset_{ce}$, by

$$f_0 = \frac{1}{2\pi}\frac{d\emptyset_{ce}}{dt} \tag{2.3}$$

The carrier-envelope phase change accumulated during one round trip in the laser cavity is derived from Eq. 2.3:

$$\Delta\emptyset_{ce} = 2\pi\frac{f_0}{f_{rep}} \tag{2.4}$$

As the pulse propagates in a dispersive laser cavity, the carrier-envelope phase is evolved by the difference between group and phase velocities of the pulse. Since the pulse is sampled once per round trip when it hits the output coupler, it is only the phase change modulated by 2π that matters. Specifically

$$\Delta\emptyset_{ce} = \left(\frac{1}{v_g} - \frac{1}{v_p}\right) l_c \omega_c 2\pi n \tag{2.5}$$

where v_g and v_p are the mean group and phase velocities in the laser cavity respectively, l_c is the length of the laser cavity, n is the mode number describing comb lines, and ω_c is the carrier frequency.

From Eq. 2.2 the absolute optical frequencies of the femtosecond comb are determined by f_{rep} and f_0 . The f_{rep} can be directly detected with a fast photodiode, but the f_0 requires a more complex technique. The measurement of f_0 is typically obtained with an interferometer. If the optical spectrum of the mode-locked laser span can be made to an

octave in the frequency domain, the highest frequencies become a factor of two larger than the lowest frequencies. The optical spectrum is broadened as optical pulses propagate through a strongly nonlinear medium (such as tapered fibre, photonic crystal fibre, semiconductor waveguide etc.) [4-9]. Then comb lines in the lowest frequency portion of the spectrum are doubled by using a second harmonic crystal and then approach approximately the same frequency as the comb lines on the high-frequency side of the spectrum [10-12]. The frequency f_0 is obtained by measuring the heterodyne beat frequency between these frequencies as accomplished in practice by using an $f-2f$ interferometer:

$$2f_n - f_{2n} = 2(nf_{rep} + f_0) - (2nf_{rep} + f_0) = f_0 \tag{2.6}$$

Once f_{rep} and f_0 are detected, there are a few ways to stabilize these frequencies with a feedback system. For f_{rep} stabilization, the straightforward method is to stabilize laser cavity length by using piezo or motorized stage inside cavity [13,14]. The f_{ceo} of the laser can be managed via the pump power, by slightly tilting a resonator mirror, or by inserting a glass wedge to a variable extent [10,15-17].

2.2 Optical frequency comb synthesis in mid-infrared region

Mid-infrared comb sources have been successfully established within the cycle of development and exploitation of a variety of other broadband mid-infrared coherent sources such as laser and optical parametric oscillators. However, a few technical challenges such as material qualities of laser gain media has delayed the maturation of those sources in this spectral region. Over the past few years, the mid-infrared frequency comb generators have succeeded remarkably. A variety of smart solutions, including novel laser gain media, nonlinear frequency conversion, Kerr comb generators and optical parametric oscillation, offer a wide choice of comb sources covering vast ranges of repetition frequency and spectral span [18] (Fig. 2.3). Mid-infrared radiation with such spectral properties can be generated through several techniques. Still, optical parametric oscillators are the most advanced tool among them in terms of wavelength coverage and power output in the mid-infrared. Commercially available phasematching crystals make them commonly used for many applications in which standard lasers do not work in the mid-infrared region.

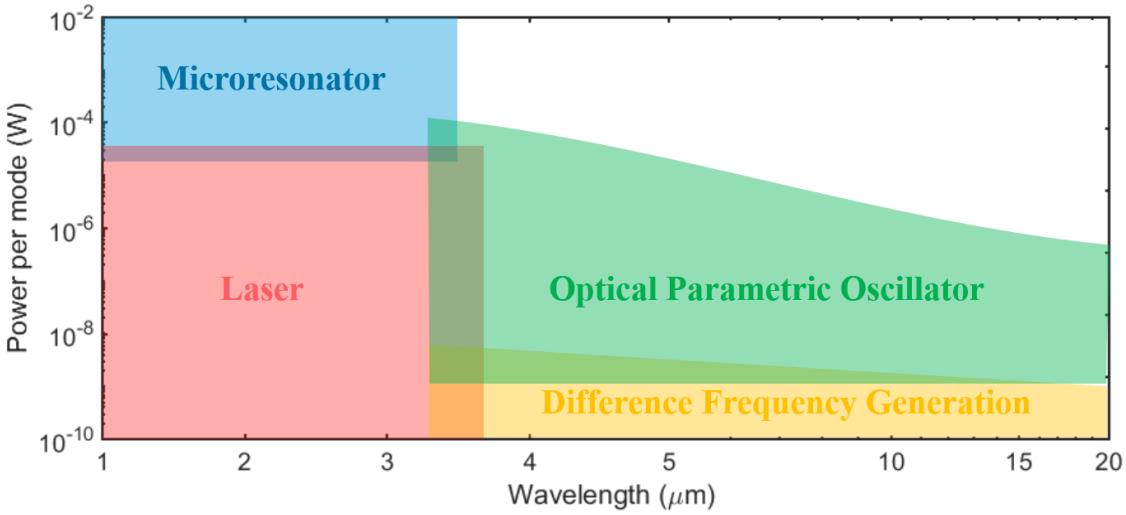

Figure 2.3: The wavelength coverage and range of power per mode of optical comb sources [18].

2.2.1 *The optical parametric oscillator*

An optical parametric oscillator (OPO) [19,20] is a coherent light source, using a resonator based optical gain from parametric amplification in a nonlinear crystal. The parametric oscillation in such devices emerges over a threshold for the pump power, below which there is negligible output power to contribute some parametric fluorescence. The parametric light called the signal and idler wavelengths determined by a phase-matching condition are converted from the pump wavelength and tuned across broad ranges. This feature enables it to access wavelengths from the mid-infrared to even the terahertz spectral region which are very challenging to obtain from any laser directly and wide wavelength tunability is also often possible by modifying the phase-matching condition. These attractions make OPOs very beneficial for laser spectroscopy.

Transparent crystalline materials exhibit different kinds of optical nonlinearities associated with a nonlinear polarization. Such parametric nonlinearities are the manifestation of the near-instantaneous response of optical nonlinearities based on $\chi^{(2)}$ or $\chi^{(3)}$ susceptibilities in materials and are useful for generating frequency doubling, sum and difference frequency generation, parametric amplification and oscillation, and four-wave mixing [21]. In such processes, the phasematching condition in the nonlinear material determines the conversion efficiency which can be obtained and this occurs only in a limited optical bandwidth. However, in order to manipulate the parameters influenced by the phasematching, it is possible to shift the wavelength range where the nonlinear interaction becomes stronger for example by using angle or grating tuning. Parametric

processes also usually depend on polarization in terms of the nonlinearity where such media exhibit birefringence at least in cases with a $\chi^{(2)}$ nonlinearity.

The phasematching condition is identified as a phase relationship between the interacting waves for efficient nonlinear frequency conversion retained along the propagation direction. By assuming a plane wave propagating in the z-direction:

$$E = A_1 \cos\{\omega t - k_1 z\} \tag{2.7}$$

where the angular wave number of the input beam (or called pump) is $k_1 = n_1\omega/c$, and n_1 is the refractive index of medium. The optical response of the medium describes an instantaneous nonlinear polarization (P) and solving Maxwell's equations lead to:

$$\nabla^2 E - \frac{n^2}{c^2}\frac{\partial^2 E}{\partial t^2} = \frac{1}{\varepsilon_0 c^2}\frac{\partial^2 P}{\partial t^2} \tag{2.8}$$

Eq. 2.8 is simplified in the condition that the incident waves travel in only one direction and only three frequencies are involved, namely as $\omega_1 \leq \omega_2 < \omega_3$. The solution of this equation produces three coupled wave equations:

$$\frac{\partial E_{1i}}{\partial z} = -\frac{i\omega_1}{cn_1} d'_{ijk} E_{3j} E^*_{2k} e^{-(i\Delta kz)} \tag{2.9}$$

$$\frac{\partial E_{2k}}{\partial z} = +\frac{i\omega_2}{cn_2} d'_{kij} E_{1i} E^*_{3j} e^{+(i\Delta kz)} \tag{2.10}$$

$$\frac{\partial E_{3j}}{\partial z} = -\frac{i\omega_3}{cn_3} d'_{jik} E_{1i} E^*_{2k} e^{-(i\Delta kz)} \tag{2.11}$$

where i, j and k refer to Cartesian coordinates and d_{ijk} is the tensor describing the relation of nonlinear coupling in the fields. Δk is the wave-vector mismatch, given by

$$\Delta k = k_3 - k_2 - k_1 \tag{2.12}$$

where

$$k_m = \frac{2\pi n(\lambda_m)}{\lambda_m} \tag{2.13}$$

The efficiency of nonlinear optical processes is achieved only if $\Delta k = 0$ where propagation directions of the waves is satisfied as shown in Fig. 2.4. In other words, this condition is only accomplished while amplitude contributions from different locations to the product wave (also called signal) are all in phase (is known as the phasematching) at the end of the nonlinear crystal. However, optical materials generally cause a non-zero phase mismatch due to chromatic dispersion of medium. The phase-mismatch issue can be accomplished by choosing a different polarization in a birefringent medium. The phasematching based on a birefringence of optical material is known as the birefringent phasematching.

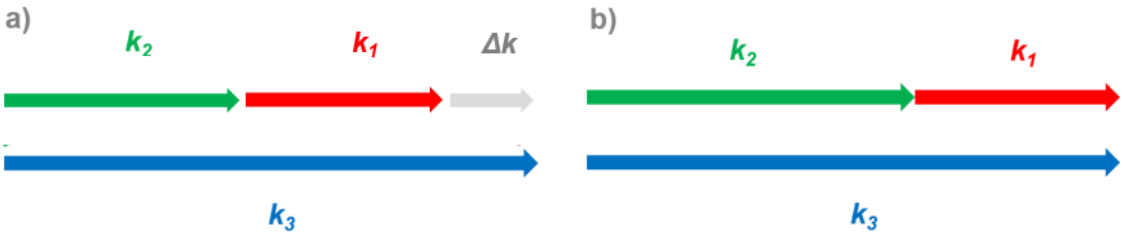

Figure 2.4: The phasematching in the conditions of $\Delta k \neq 0$ (a) and $\Delta k = 0$ (b). The optimal energy conversion efficiency is achieved under $\Delta k = 0$.

The significance level of the phase-mismatch is basically quantified by considering the distance over which a π radians phase slip occurs between the electric fields propagating in the nonlinear medium. This is also known as the coherence length, given by:

$$L_{coh} = \frac{\pi}{|\Delta k|} \tag{2.14}$$

Alternatively, phasematching can be achieved by using an optical material with spatially modulated nonlinear properties in particular for nonlinear frequency conversion. This technique is called quasi-phase matching (QPM). In contrast to the birefringent phasematching, QPM is able to use the same polarization direction for all interacting waves by using a stronger element of the nonlinear tensor. This phenomenon is accomplished in the form of a phase step of π being added to the interacting fields by periodically flipping the polarity of the nonlinear coefficient tensor d_{ijk} with a characteristic spatial period of Λ_g:

$$\Lambda_g = \frac{2\pi}{|\Delta k|} \tag{2.15}$$

When Eq. (2.15) is modified with Eq. (2.13), QPM is satisfied by varying the length of the grating period, given by

$$\Lambda_g = \left[\frac{n(\lambda_3)}{\lambda_3} - \frac{n(\lambda_2)}{\lambda_2} - \frac{n(\lambda_1)}{\lambda_1}\right]^{-1} \tag{2.16}$$

or alternatively represented in terms of the phase-mismatch:

$$\Delta k = k_3 - k_2 - k_1 - \frac{2\pi}{\Lambda_g} \tag{2.17}$$

Periodic orientation in a nonlinear crystal has been developed in order to change the sign of the nonlinear coefficient of medium by periodic poling technique (Fig. 2.5a) [22,23]. The poling period of a periodically poled medium is determined by two coherence lengths ($2L_{coh} = \Lambda_g$) explaining how the phasematching condition is defined in Eq. (2.15). The intensity growth of converted photons under QPM conditions is presented in Fig. (2.5b).

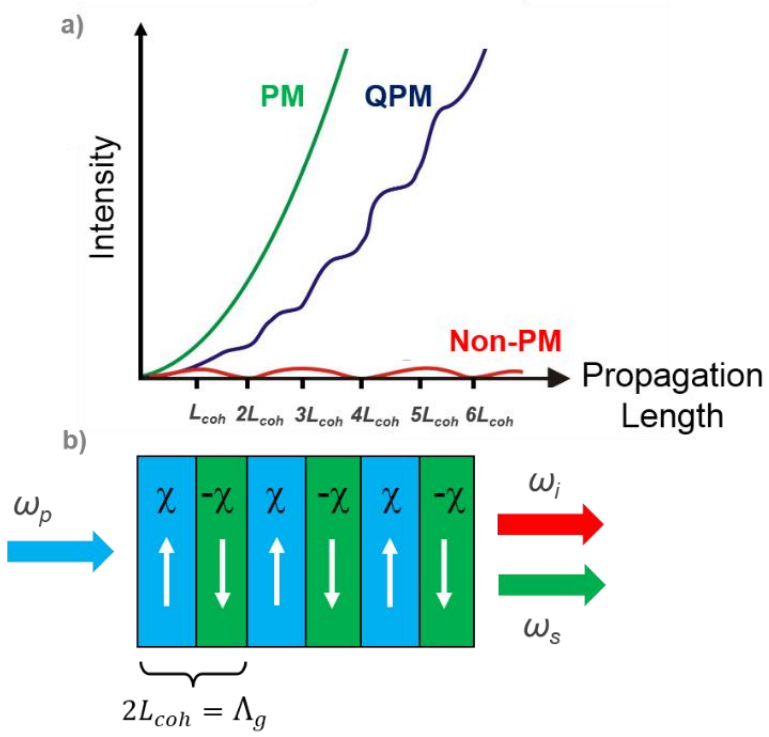

Figure 2.5: The phasematching in the nonlinear crystal. **(a)** The phasematched case occurs in the direction of material and **(b)** the quasi phasematching is achieved by the periodic poled crystals.

The $\chi^{(2)}$ nonlinearity can be also used to amplify weak optical signals. The basic configuration involves an input "signal" at ω_2 which is incident on a nonlinear crystal with an intense pump wave at ω_3 where $\omega_3 > \omega_1$. The amplification of the ω_1 wave is accompanied by the generation of an "idler" wave at $\omega_1 = \omega_3 - \omega_2$.

The fundamental amplification process describes how some of the pump photons are converted to signal and idler photons. More precisely, for each incident pump photon (ω_p), one signal photon (ω_s) and one idler photon (ω_i) is generated. By considering Eq. (2.9) - (2.11) and (2.12), a new equation is defined with phasematching ($\Delta k = 0$) in terms of intensity of interacting waves as:

$$\frac{dI_1}{dz} + \frac{dI_2}{dz} = -\frac{dI_3}{dz} \tag{2.18}$$

Eq. (2.18) is modified with a statement of conservation energy among incident pump photons, signal photons and idler photons. This is described by the Manley-Rowe equation [24]:

$$\frac{dN_i}{dz} = \frac{dN_s}{dz} = -\frac{dN_p}{dz} \tag{2.19}$$

where N is the number of photons stating that, for every pump photon gained (or lost) at ω_p, one photon is lost (or gained) at both ω_s and ω_i. The sum of the signal and idler frequencies equal the pump frequency, given by

$$\omega_p = \omega_s + \omega_i \tag{2.20}$$

Then this equation can be also modified to

$$\frac{1}{\lambda_p} = \frac{1}{\lambda_s} + \frac{1}{\lambda_i} \tag{2.21}$$

Considering that these three waves are pulsed fields, each wave has different group velocity in general. Therefore, group velocity mismatch becomes critical to determine the

character of three waves interaction. If Eq. 2.12 is derived and simplified for the phasematching as a function of frequency, It is given by

$$\Delta k = \left(\frac{\partial k_p}{\partial \omega_p} - \frac{\partial k_s}{\partial \omega_s}\right)\Delta\omega_p - \left(\frac{\partial k_i}{\partial \omega_i} - \frac{\partial k_s}{\partial \omega_s}\right)\Delta\omega_i \tag{2.22}$$

Since $\partial k/\partial\omega = (v_g)^{-1}$ the phase mismatch in the inverse group velocities is an important parameter for the frequency variation of the phase mismatch and the terms of each parenthesis are described as $\Delta(v_g^{-1})$. When Eq. 2.9-2.11 are modified by considering the phasematching and the group velocities as a function of time and the depleted pump is assumed to be negligible, the pump beam in the electric field is again described as

$$\frac{\partial E_3}{\partial z} + \frac{1}{v_{g,3}}\frac{\partial E_3}{\partial t} = -i\frac{\omega_3 d'_{jik}}{cn_3}E_1\left(t - \frac{z}{v_{g,1}}\right)E_2\left(t - \frac{z}{v_{g,2}}\right) \tag{2.23}$$

where $\omega_3 d'_{jik}/cn_3$ is the coupling constant κ. The intensity of the pump beam is also given by

$$I_3(L, t'_3) = \frac{\omega_3^2 d_{jik}^2}{2c^3\varepsilon_0 n_1 n_2 n_3} I_1(t'_3) I_2(t'_3) L^2 \tag{2.24}$$

where $t'_3 = t - z/v_{g,3}$ is the retarded time corresponding to a reference frame moving with group velocity of E_3. Here, the propagation equation is rewritten by using retarded time frame as

$$\frac{\partial E_3(z, t'_3)}{\partial z} = -i\kappa_3 E_1(t'_3 - \eta_{13} z) E_2(t'_3 - \eta_{23} z) \tag{2.25}$$

where η_{ij} has been introduced as

$$\eta_{ij} = \frac{1}{v_{g,i}} - \frac{1}{v_{g,j}} \tag{2.26}$$

As a solution of Eq. 2.19, it is generalized for undepleted pump waves as given by

$$E_3(L, t_3') = -i\kappa_3 \int_0^L E_1(t_3' - \eta_{13}z)E_2(t_3' - \eta_{23}z)dz \tag{2.27}$$

During the interaction in the nonlinear material, the phasematching bandwidth is evaluated on the magnitude of the group delay difference, $\left|\Delta\left(v_g^{-1}\right)\right|L$ where L is the interaction length of crystal, in comparison to the input pulse width $\Delta\tau$. There are two cases resulting the nonlinear conversion in the crystal:

- $\left|\Delta\left(v_g^{-1}\right)\right|L \ll \Delta\tau$: The group delay difference is much less than the pulse width and negligable. If the input pulses are bandwidth-limited, the phasematching bandwidth is much wider than input spectrum.

- $\left|\Delta\left(v_g^{-1}\right)\right|L \gg \Delta\tau$: The group delay mismatch is greater than the pulse width and this condition satisfies that the phasematching bandwidth is much narrower than the input spectrum.

To consider these cases, the temporal walkoff length l_T is defined in the case of $\left|\Delta\left(v_g^{-1}\right)\right|L = \Delta\tau$ and shown as

$$l_T = \frac{\Delta\tau}{\left|\Delta\left(v_g^{-1}\right)\right|} \tag{2.28}$$

for which the temporal walkoff is related to the pulse width. As a consequence of Eq. 2.28, the interaction inside the thick crystal generates large group velocity mismatch and this can be compensated with a longer pulse width.

Although the idler photons generated after the nonlinear crystal are often not oscillated, these are essential in the amplification process: for a material with strong absorption of the idler wave, the amplifier performance can be strongly degraded. If a nonlinear crystal

is placed within an optical cavity which provides resonances for the signal or the idler waves or both, parametric gain at pumping threshold intensity generates simultaneous oscillation called optical parametric oscillation at both the signal and idler frequencies (Fig. 2.6). The threshold of this oscillation is surpassed once the parametric gain exceeds the losses of the signal and idler waves. This phenomenon is the physical basis of optical parametric oscillation. Similar to a laser, a finite signal beam is initially composed from the noise, with a portion of the signal intensity transmitted out of the cavity by using output coupler. Unlike a laser, the gain can be set of transitions, which are limited in their optical bandwidth and tuning range of parametric oscillation by the phasematching condition. An idler wave is also generated although usually it is not resonated inside cavity. This is called a singly resonant optical parametric oscillator. If both the signal and idler are fed back into the cavity, this is called a doubly resonant optical parametric oscillator.

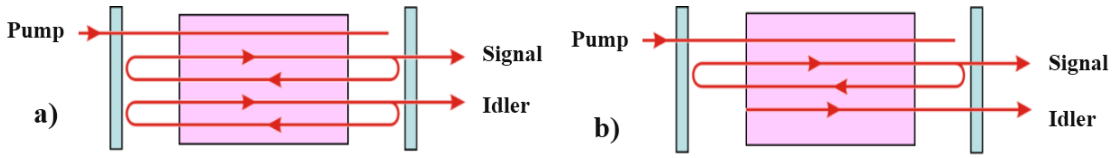

Figure 2.6: Schematic of an optical parametric oscillator. The idler and signal are resonant together called doubly resonant in a same cavity (a). There is also possibility for singly resonator which is resonant at either the signal or the idler wavelength (b).

2.2.2 *Mid-infrared optical parametric oscillator combs*

OPOs are coherent light sources and, like lasers can be used to generate frequency combs, whose applications are chosen with appropriate consideration of bandwidth and wavelength coverage, as for example in spectroscopy and frequency metrology. Unlike laser media, the parametric frequency conversion process of OPOs allows their wavelengths to be both widely tunable and have a broad spectral bandwidth, only limited by the absorption characteristics of the nonlinear gain material. Due to the instantaneous gain process of OPOs, the parametric fluorescence in OPOs does not contribute as parasitic noise. By using a short crystal, the coupling of intensity fluctuations into phase noise can be reduced as well. Using low-noise pump lasers, OPO frequency combs can be supporterd with carrier-envelope-offset (CEO) frequency beat linewidths of a few Hz [25].

The first femtosecond OPO comb was demonstrated at Heriot-Watt University in 2007 [26]. Since its beginning, remarkable results have been accomplished with the few-cycles pulses [25], the demonstration of high power powers delivering 1 W [27], zero-offset combs extending phase coherence among all the parametrically related fields [28], GHz operation [29], tunability into the visible [30] and mid-infrared [31], Hz-level offset-frequency linewidths [26] and sub-50 attosecond timing jitter between pulses in the same parametrically related comb [32].

Principally, a pump beam is converted to a signal and an idler beam in the parametric process with the optical phase relationship between all three waves given (modulo 2π) by [32]:

$$\theta_p = \theta_s + \theta_i + \frac{\pi}{2} \tag{2.29}$$

where θ_p, θ_s, and θ_i are the phases of the pump, signal, and idler, respectively. Here, the cavity length and the intracavity dispersion are critical to associate the optical phase of the signal and idler. As a result of the phase relationship in Eq. 2.29, oscillation occurs when the cavity length of the OPO is matched with that of the pump laser which means the pulse repetition frequencies of both the pump and signal need to be matched [36]. The optical phase of a femtosecond OPO is also related to the phase difference of the carrier wave relative to the pulse envelope.

In the frequency domain, a pulse train is defined by a series of equally spaced spectral lines and forms a frequency comb localized with a CEO frequency that corresponds to the carrier-envelope phase slip of successive pulses. The optical frequencies of individual comb lines in the pump, f_p, signal, f_s, and idler, f_i, beams are written

$$f_p = f_{0,p} + l f_{REP} \tag{2.30}$$

$$f_s = f_{0,s} + m f_{REP} \tag{2.31}$$

$$f_i = f_{0,i} + n f_{REP} \tag{2.32}$$

where *l*, *m*, *n* are integers, f_{REP} is the pulse repetition frequency and $f_{0,p}$, $f_{0,s}$ and $f_{0,i}$ are the CEO frequencies of the pump, signal and idler beams, respectively. These three optical frequencies also exhibit agreement with the simple equation of energy conservation, and their CEO frequency relation is described by

$$f_{0,p} = f_{0,s} + f_{0,i} \tag{2.33}$$

For any wave, *j*, with its CEO frequency, $f_{0,j}$ the CEP slips of successive pulses ($\Delta\theta j$) are linked together by

$$f_{0,j} = \frac{\Delta\theta_j}{2\pi} f_{REP} \tag{2.34}$$

From Eq. 2.29, the CEP slip relation between the parametric beams then is expressed as

$$\Delta\theta_p = \Delta\theta_s + \Delta\theta_i \tag{2.35}$$

Thus, the relative CEP slips can be controlled by actuating just two of the CEO frequencies from pump, idler, and signal. For the same reason, the CEO frequency of the signal (or idler) pulses can be identified by using interference between a pump supercontinuum and the pump + signal (or pump + idler) sum frequency mixing (SFM) light (Fig 2.7). The pump super-continuum (pSC) comb, f_{pSC} ($=lf_{REP}+f_{0,p}$) and the comb corresponding to the pump + idler SFM light, f_{SFM} ($=(m+n)f_{REP}+f_{0,p}+f_{0,i}$) are heterodyned to substract the idler carrier-envelope offset frequency $f_{0,i}$ and harmonics of the laser repetition frequency, f_{REP}. Then the idler offset frequency can be controlled by making a slight cavity-length change with (for example) a piezoelectric transducer (PZT) to cause the phase relation to change in the OPO [26]. This approach is also applicable to control the signal offset by beating pump + signal sum-frequency light with the pump super-continuum. However, every optical mode can be precisely investigated when all offset frequencies are fully stabilized with additionally stabilizing the pump laser repetition frequency.

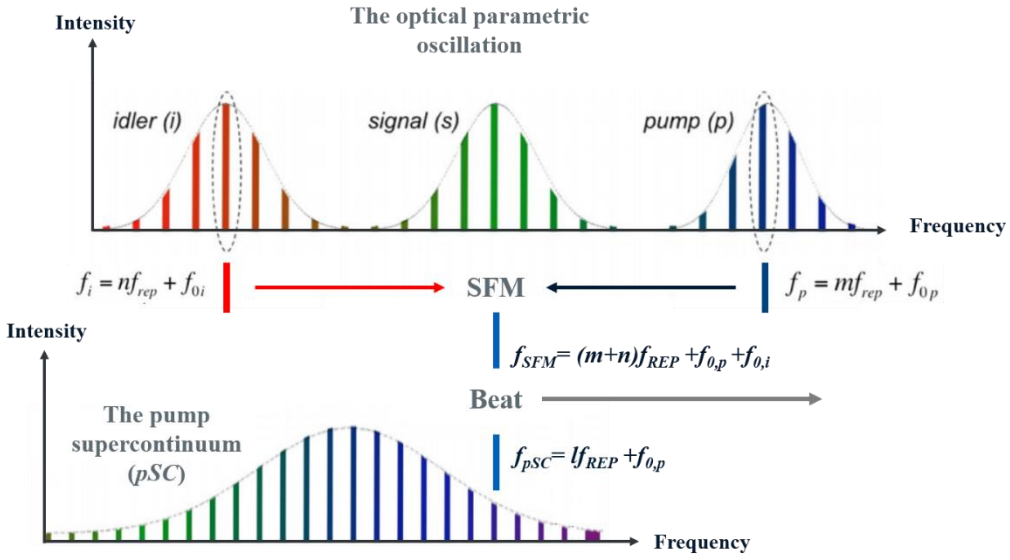

Figure 2.7: The detection of the idler offset frequency, $f_{0,i}$. Beating the $p + i$ sum frequency mixing (SFM) light with pump super-continuum light of the same wavelength including the pump offset frequency reveals only frequencies at the harmonics of the repetition rate and $\pm f_{0,i}$.

2.3 Molecular spectroscopy in the mid-infrared region

Spectroscopy is an essential tool to investigate molecular structure, dynamics, and properties in the qualitative and quantitative analysis of many species. Therefore molecular spectroscopy aims to analyze the spectral response of molecules interacting with electromagnetic radiation in various frequencies and energy (from UV to infrared region). Electromagnetic radiation is employed to induce transitions between molecular energy levels (Fig. 2.8).

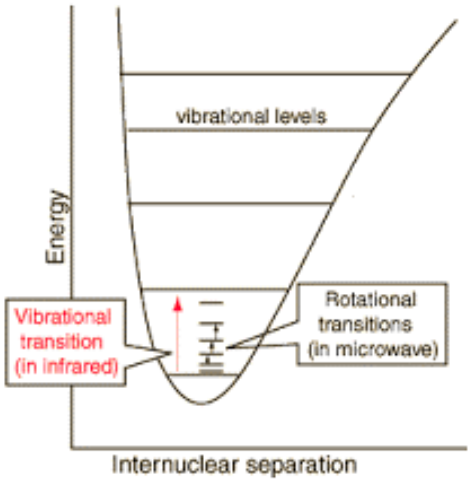

Figure 2.8: The energy levels of a diatomic molecule. Typical energy levels of electronic states, vibrational states, rotational states are ~10^{-19}, ~10^{-20} and ~10^{-23} J respectively [33].

The energy, *hν*, of the emitted or absorbed photon, and the frequency *ν* of the emitted or absorbed radition is described in the Bohr frequency condition:

$$\Delta E = h\nu = |E_1 - E_2| \tag{2.36}$$

The absorption or emission of radiation occurs at specific frequencies corresponding to energy level differences [34]. Such frequencies are described as the transition frequencies containing information about rotational, vibrational, or electronic energy separations. In the Born-Oppenheimer approximation the energy of a molecule is written as the sum of electronic energy E_{el}, vibrational energy E_{vib} and rotational energy E_{rot} energy:

$$E_{molecule} = E_{el} + E_{vib} + E_{rot} \tag{2.37}$$

where these energies are ranged as $h\nu_{el} \gg h\nu_{vib} \gg h\nu_{rot}$.Thus each frequency is uniquely affected by radiation of a specific wavelength. Particularly, infrared spectra of the sample can be identified with quantized vibrational energy states. Molecular vibrations are a result of motions from the coupled motion of the two atoms of a diatomic molecule to the more complex motion of every single atom of a large polyfunctional molecule with respect to the *x*, *y* and *z* axes. All atoms vibrate at a certain characteristic frequency, ν_i and each harmonic displacement of the atoms can be associated with a mode, *i*. The vibrational energy states of molecular bonds vibrating with simple harmonic motion can be written as:

$$E_{vib}(i) = h\nu_i \left(v_i + \frac{1}{2}\right) \tag{2.38}$$

where *h* is Planck's constant and v_i is the vibrational quantum number of i^{th} mode (v_i = 0, 1, 2, …). Vibrational frequencies here are given in units of wavenumber (cm^{-1}) and the energy difference for transitions between the ground state (v_i = 0) and the first excited state (v_i = 1) of most vibrational modes corresponds to the energy of radiation in the mid-infrared spectrum (400 to 4000 cm^{-1} or 2.5 to 25 μm). Since every molecule has slightly different vibrational modes from all other molecules, the infrared spectrum of a sample molecule is unique and identifies that molecule. The spectra of molecules in the

different phases (gases, liquids, and solids) have different characteristics as well. The transitions of molecules in different phases occur between the quantized rotational energy levels at the same time as vibrational transitions. The rotational energy levels of diatomic molecules are depicted by a single rotational quantum number, *J* and given by

$$E_{rot}(J) = \frac{h}{8\pi^2 Ic} J(J+1) \tag{2.39}$$

where *I* is the moment of inertia of the molecule and *c* is the velocity of light. The transitions between rotational energy states for linear molecules are determined by a rule of $\Delta J = \pm 1$ and ΔE_{rot} becomes $2h/8\pi^2 Ic$ for a transition between adjacent energy states.

For most molecules, the pure rotation spectrum is analyzed in the microwave region. However, light molecules such as HCl, H_2O, or CO are active for rotational transitions in the far infrared.

For diatomic molecules in the gas phase, their vibrational transitions are accompanied with rotational transtions ($\Delta v_i = \pm 1$ and $\Delta J = \pm 1$). Therefore, the vibration-rotation spectrum of diatomic molecule consists of a series of equally spaced lines around transition frequencies corresponding to $\Delta J = +1$ and $\Delta J = -1$. The series of lines below frequency corresponding $\Delta J = -1$ are known as the *P* branch of the band, while the series of lines above frequency corresponding $\Delta J = +1$ are known as the *R* branch of the band. If $\Delta J = 0$, there is a strong line called *Q* branch in the spectrum (Fig. 2.9).

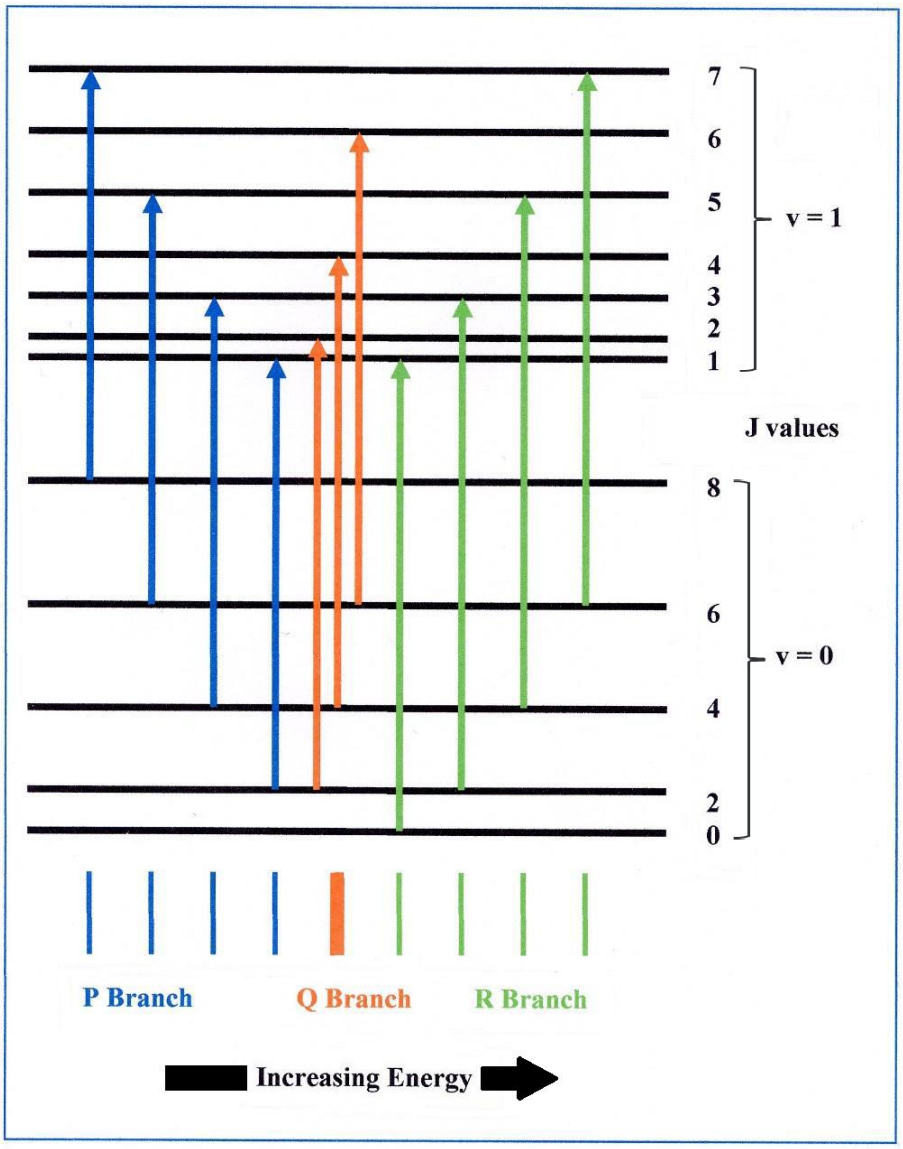

Figure 2.9: Energy level diagram described with atomic transitions of a molecule in the infrared spectroscopy.

Returning to consider the absorption of radiation by a sample again, the ratio of the transmitted intensity I to incident intensity I_0 is called the transmittance and is given by

$$T = \frac{I}{I_0} \tag{2.40}$$

Alternatively, the absorbed intensity is described by the inverse of the transmittance ($1/T$). According to the Beer-Lambert law, the transmitted intensity I varies with the length, L of the sample:

$$I = I_0 e^{-\sigma NL} \tag{2.41}$$

where σ is an absorption cross section and N is the number of molecules per volume (concentration). The units of these components are expressed in cm^2 for σ, cm^{-3} for N and cm for L. The optical density of the sample is obtained empirically

$$\ln\left(\frac{I}{I_0}\right) = -\sigma NL \tag{2.42}$$

where the I and σ are the function of the radiation frequency. This equation is also modified in terms of molar absorption coefficient ε and molar concentration c ($c=N/N_A$; N_A is the Avogadro number, $N_A \approx 6.022\text{x}10^{-23}$ mol^{-1}):

$$\ln\left(\frac{I}{I_0}\right) = -\varepsilon cL \tag{2.43}$$

The absorbance or transmittance of any component is proportional to the concentration of the sample and commonly measured by Fourier transform spectroscopy in the infrared region.

2.4 Fourier transform spectroscopy

Fourier transform spectroscopy (FTS) was developed using incoherent light sources (thermal sources, sunlight etc.) in the mid-20th century [35], and soon became the most used infrared spectrometer [36]. Fourier transform spectrometers measure interferograms, from which a single beam spectrum is evaluated. The intensity of the single beam spectrum is proportional to the power of the radiation detected by the detector. Then the ratio of the single beam spectra of the sample is calculated to measure the absorbance of spectrum of that sample.

The design of the Fourier transform spectrometer is based on that of two beam interferometers also known Michelson interferometers. The Michelson interferometer is a device that divides a beam of radiation into two paths and then recombines the two beams with a path difference (Fig. 2.10). The variation of intensity of the beam at the

output of the interferometer is measured as a function of path difference by a suitable detector.

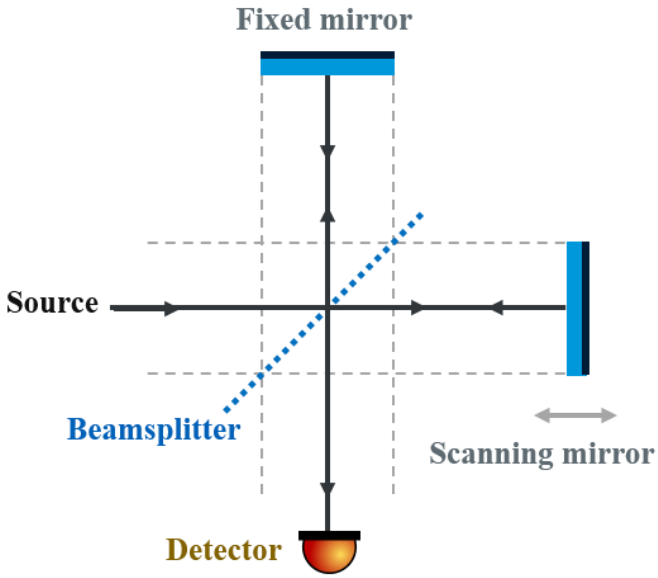

Figure 2.10: Michelson interferometer in Fourier transform spectrometer.

For a monochromatic input wave, frequency v_0 , the intensity of the beam at the detector is measured a quantity, given by

$$I'(\delta) = \frac{1}{2} I(v_0)(1 + \cos(2\pi v_0 \delta)) \tag{2.44}$$

where $\delta = n/v_0$ (n is an integer) is retardation that is equal to the intensity of the source $I(v_0)$. $I'(\delta)$ is composed of a constant (dc) component corresponding to $0.5I(v_0)$ and a modulated (ac) component corresponding to $0.5I(v_0)\cos(2\pi\ v_0\delta)$. This modulated component becomes very important and is called the interferogram. When a continuum source is used instead of a single frequency source (v_0), the amplitude term of interferogram ($0.5I(v_0)$) is replaced with $B(v_0)$ modified by the intrumental characteristics and the interferogram is represented by the integral

$$S(\delta) = \int_{-\infty}^{+\infty} B(v)\cos(2\pi v\delta)dv \tag{2.45}$$

The interferograms are not entirely meaningful by themselves. The interferogram is a function of time whereas a spectrum is a function of frequency (or wavelength). A spectrum is obtained by computing the cosine Fourier transform of the interferogram, $S(\delta)$. From Eq. 2.45, $B(v_0)$ is obtained with the theory of Fourier transformations to give the spectrum itself with the result of

$$B(\delta) = 2\int_0^{+\infty} S(\delta)\cos(2\pi v\delta)d\delta \tag{2.46}$$

which integrates the complete spectrum from 0 to ∞ cm^{-1}. This means that interferogram is composed by an infinite number, N of data points in theory. Thus interferograms must be sampled discretely. Then acquired data is computed with discrete Fourier transformation in a resonably fast computer. The transformed data is a power spectrum including the ratio between the background and the sample. This ratio is expressed as transmittance.

2.4.1 *Sampling and aliasing in Fourier transform spectroscopy*

The sampling rate of FTS is determined by the Nyquist criterion which describes the digitization of an analogue signal without any loss of information. The Nyquist sampling theorem states a convenient condition for a sample rate that allows a discrete sequence of samples to acquire all the information from a continuous-time signal of finite bandwidth. A sufficient sample-rate is therefore $2N$ samples per second, or anything larger. Equivalently, for a given sample frequency f_s, perfect reconstruction is acomplished for a bandwidth $N < f_s/2$. If the maximum frequency in the signal exceeds $f_s/2$, the reconstruction exhibits imperfections known as aliasing.

Aliasing is very critical for high-resolution spectrometry where large data sets require avoiding excessive oversampling. To consider the detector that sees the highest wavenumber v_{max} in a spectrum, the frequency of the cosine wave in the interferogram which corresponds to v_{max} is Vv_{max} where V is the optical velocity determined by variation of optical path difference in the Michelson interferometer. Therefore, the interferogram must be digitized at a frequency of $2Vv_{max}$. When the spectrum restricted from v_{min} to v_{max} is required at a resolution of Δv, the number of points that must be recored to avoid aliasing is

$$N_s = \frac{2(v_{max} - v_{min})}{\Delta v} \tag{2.47}$$

The Nyquist criterion is physically satisfied when the bandwidth of spectrum is limited with an optical or electronic filter. Then the interferogram is measured over a limited retardation of the scan.

2.4.2 *Instrument line shape and apodization*

Apodization is used to moderate discontinuities at the beginning and end of the sampled time record. By considering the maximum retardation of interferogram to Δ, the complete interferogram (between δ= ∞ and δ=-∞) is multiplied with a truncation function *D*(δ), given by

$$D(\delta) = f(x) = \begin{cases} 1, & if \ -\Delta \leq \delta \leq +\Delta \\ 0, & if \quad \Delta > |\Delta| \end{cases} \tag{2.48}$$

By analogy to Eq. 2.9, spectrum is modified as

$$B(v) = \int_{-\infty}^{+\infty} S(\delta) D(\delta) \cos(2\pi v \delta) d\delta \tag{2.49}$$

If the product of any two functions is Fourier transformed, the convolution of the Fourier transformation of each function is resulted here. To use this approach, the Fourier transform of *D*(δ) is evaluated as we know that the Fourier transform of *S*(δ) is *B*(δ) and it is given by

$$f(v) = 2\Delta \text{sinc} 2\pi v \Delta \tag{2.50}$$

Mathematically, the convolution of *B*(δ) and *f*(ν) is described by:

$$G(v) = B(v) * f(v) = \int_{-\infty}^{+\infty} B(v') f(v - v') dv' \tag{2.51}$$

where ν' is the displacement increments of the scan and $f(\nu)$ is the instrument line shape function. When the sinc function in Eq. 2.50 is convolved with a single spectral line of wavenumber ν_1, the resulting spectrum is given by

$$B(\nu) = 2\Delta B(\nu_1)\text{sinc}2\pi(\nu_1 - \nu)\Delta \tag{2.52}$$

However, the sinc function is not a particularly right lineshape for infrared spectrometry due to its relatively large amplitude at wavenumber of infrared region. For that reason, a simple triangular weighting function is a better choice instead of the truncation function, $D(\delta)$ and it has a form of

$$A_1(\delta) = f(x) = \begin{cases} 1 - \left|\frac{\delta}{\Delta}\right|, & if\ -\Delta \leq \delta \leq +\Delta \\ 0, & if\ \ \Delta > |\Delta| \end{cases} \tag{2.53}$$

The spectrum is then convolved with the Fourier transform of $A_1(\delta)$ and instrument function for infrared spectroscopy is

$$f_1(\nu) = \Delta\text{sinc}^2\pi\nu\Delta \tag{2.54}$$

This function helps to suppress sidelobes appearing away from the line centre. This technique is known as apodization and $A_1(\delta)$ is apodization function here [37]. Such functions are very critical to determine real spectral characteristics of species measured by FTS.

2.5 Dual-comb spectroscopy

Dual-comb spectroscopy (DCS) associates tunable laser spectroscopy with the strengths of conventional broadband spectroscopy [38-53]. Although conventional Fourier transform infrared (FTIR) spectrometers with incoherent sources suffer from low signal:noise as a result, laser spectrometers have high frequency resolution and accuracy set by the laser rather than the instrument, and their spatially coherent mode outputs allow long interaction paths for obtaining high sensitivity. Since the first demonstrations, DCS has attracted substantial attention in many challenging experiments [38,54]. DCS has been rapidly enhanced to enable comb-tooth-resolved spectra with a high signal-to-noise ratio (SNR) over broad optical bandwidths in the near-IR [55]. From its beginning, DCS

has been explored at longer wavelengths, where spectroscopic signatures are more significant [39]. Many applications with DCS have been demonstrated for ultrabroadband near-IR spectroscopy [56], to near-field microscopy for subwavelength spatial resolution [57], precision metrology of molecular line centers [55], a spectral lidar [58], and greenhouse gas monitoring [59].

2.5.1 *Principles of dual comb spectroscopy*

DCS is a concept that two identical combs with slightly different repetition rates are interfered on a photodiode generating an RF comb composed of individiual beats between pairs of optical comb teeth (Fig. 2.11). This RF comb containing the relevant spectral information in the optical comb spectra is easily processable in similar way to conventional FTS with RF electronics. DCS is applied to spectroscopy when a sample is introduced into one or both optical beam paths and then immediately the comb light which has interacted with the sample is detected. If both combs are combined and then transmitted through the sample, this symmetric approach is similar to the typical FTIR configuration and measures the sample's absorption without turbulence across the measurement paths. In contrast to the symmetric approach, only one comb can be transmitted through the sample and then interfered with the second "local oscillator" comb after sample. This asymmetric approach is similar to the "dispersive" FTIR technique, and the full phase and amplitude response of the sample is also measured [60]. To precisely measure the sample, the intrinsic noise in the comb spectrum must be removed by suitable normalization.

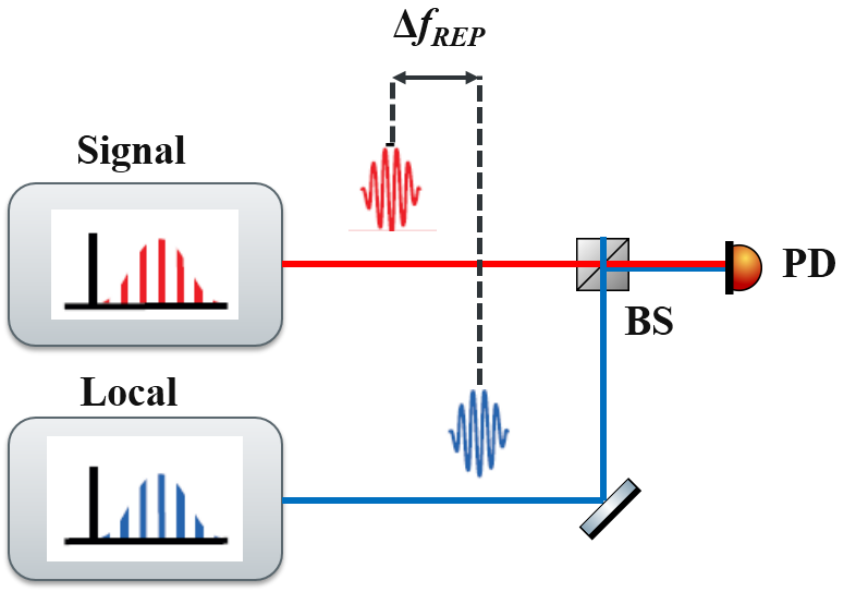

Figure 2.11: The generic picture of dual-comb spectroscopy.

In the frequency domain shown in Fig. 2.12a, the DCS signal is extracted as an RF comb whose intensity and phase are proportional to the product of the electric fields of the two adjacent comb lines. Electric fields of both frequency combs are given as

$$E_1(t) = \sum_n A_{1,n} e^{-i2\pi\{f_{ceo,1}+n(f_{REP}+\Delta f_{REP})\}t} + c.c. \tag{2.55}$$

$$E_2(t) = \sum_n A_{2,n} e^{-i2\pi\{f_{ceo,2}+nf_{REP}\}t} + c.c. \tag{2.56}$$

where $A_{i,n}$ is the amplitude of a pulse envelope and $f_{ceo,i}$ is the carrier-envelope offset (CEO) frequency of each comb.The combination of both pulse trains is considered only for the nearest comb modes of comb 1 and comb 2. Then the interfered comb modes called interferograms are written in time domain:

$$S(t) \sim \sum_n A_{1,n} A_{2,n}^* \, e^{-i2\pi(\Delta f_{ceo}+n\Delta f_{REP})t} + c.c. \tag{2.57}$$

where Δf_{ceo} is the difference of offset frequencies of comb 1 and comb 2. The Fourier transform of the interferogram is used to obtain the spectrum as

$$B(\nu) \sim \sum_n A_{1,n} A_{2,n}^* \, \Delta\{\nu - (\Delta f_{ceo} + n\Delta f_{REP})\} + c.c. \tag{2.58}$$

All products of the nearest modes in Eq. 2.58 are mapped in the RF spectrum of width, $\Delta\nu$, where the optical spectrum is now composed of

$$\Delta\nu_{RF} = \frac{\Delta\nu_{opt}}{m} \tag{2.59}$$

where $m=f_{rep}/\Delta f_{rep}$ is the down-conversion factor follows that f_{rep} is the comb repetition frequency and Δf_{rep} is the repetition frequency difference between the two combs. Conversion factors, m is typically a magnitude of between 30,000–1,000,000 , and several hundred thousand comb modes, spanning tens to hundreds of THz, can be mapped into a RF band and digitized easily.

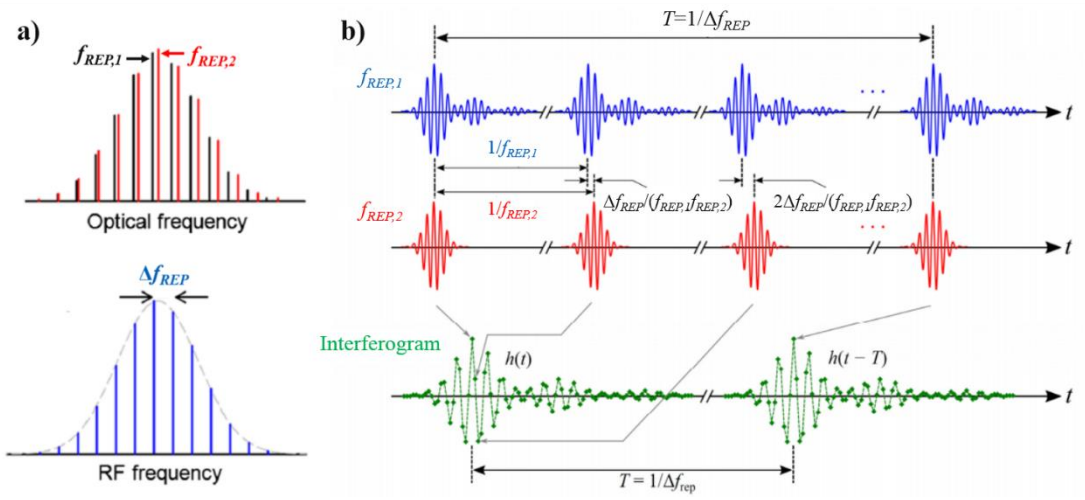

Figure 2.12: The DCS configuration, where consecutive comb modes are mapped are mapped in the optical RF spectrum of width, $\Delta\nu$, where an RF spectrum is composed of, $\Delta\nu/m$, where $m=f_{rep}/\Delta f_{rep}$.

As shown in Fig. 2.12, every two consecutive modes mapped onto RF domain from the optical domain is only restricted in case of the optical spectral bandwidth satisfying as:

$$\Delta\nu \leq \frac{mf_{rep}}{2} = \frac{f_{rep}^2}{2\Delta f_{rep}} \tag{2.60}$$

Fig. 2.12b also illustrates a distinctive time-domain picture of DCS. Here, the two adjacent comb modes are sampled with very fine time delays between each consecutive pair of pulses given by

$$\Delta T = \frac{\Delta f_{rep}}{f_{rep}(f_{rep}+\Delta f_{rep})} \approx \frac{1}{mf_{rep}} \tag{2.61}$$

which is in the picosecond to femtosecond range. This is analogous to linear optical sampling or a sampling scope in which the repetitive pulse train of one comb is captured in the sampling gate determined by the femtosecond pulses of other comb asynchronously, making it possible to downsample that comb. The resulting time-domain signal is formed as an "interferogram" in the same way as in FTS. From inspection of Eq. 2.60, the Nyquist condition for sampling as in FTS is described for sampling a time step per point of ΔT. Furthermore, the RF comb modes are only resolved in a minimum time of $1/\Delta f_{REP}$. Therefore, acquisition speed providing that Eq. 2.61 is limited by the optical bandwidth of combs...

As discussed how interferograms are transformed into meaningful structures in Section 2.4.2, the interferogram are apodized to digitize finite number of acquired points. Thus, the acquisition time of a particular single spectrum is reduced nominally, while the acquisition rate of consecutive spectra is still Δf_{REP}. Moreover, the frequency comb structure is distorted by being smoothed across comb teeth due to the apodization function. Although such spectral smoothing significantly enhances SNR per spectral point, the comb modes are resolved at low resolution. For this reason, SNR should be improved with independent smoothing techniques.

The sensitivity of DCS is determined by the SNR in the normalized optical RF spectrum, which is related to SNR in time domain as

$$\langle SNR \rangle_f = \langle SNR \rangle_f \frac{\sqrt{N}}{M} \tag{2.58}$$

where N is the number of data points the interferogram and M is the number of resolved comb modes. Since the sample's response is acquired, DCS sensitivity is normalized to the number of resolved comb modes and the minimum detectable feature of sample per spectral element is expressed by

$$\alpha_{min} = \left[L_{eff} \langle SNR \rangle_f \right]^{-1} \sqrt{\frac{T}{M}} \tag{2.59}$$

in units of $cm^{-1}Hz^{-1/2}$, where L_{eff} is effective interaction length of sample and T is the acquisition time of interferogram taken in DCS [43].

2.5.2 *Dual comb spectroscopy in mid-infrared region*

Molecular spectroscopy principally tends to emphasize wavelengths beyond 3 μm, where molecules reveal much stronger absorption cross sections. Since the first implementations, DCS has made notable progress in the near-infrared region where many low noise laser sources have already been developed for comb applications. Despite all its advantages, DCS is still competing with FTIR for many applications requiring broad spectral coverage into the mid-IR (3–5 μm) and far-IR (6–13 μm). As illustrated in Fig. 2.13, the development of frequency combs in the mid-infrared is undergoing a move into

these spectral regions, and there have been a number of interesting DCS demonstrations pioneered by Keilmann and coworkers [39,40].

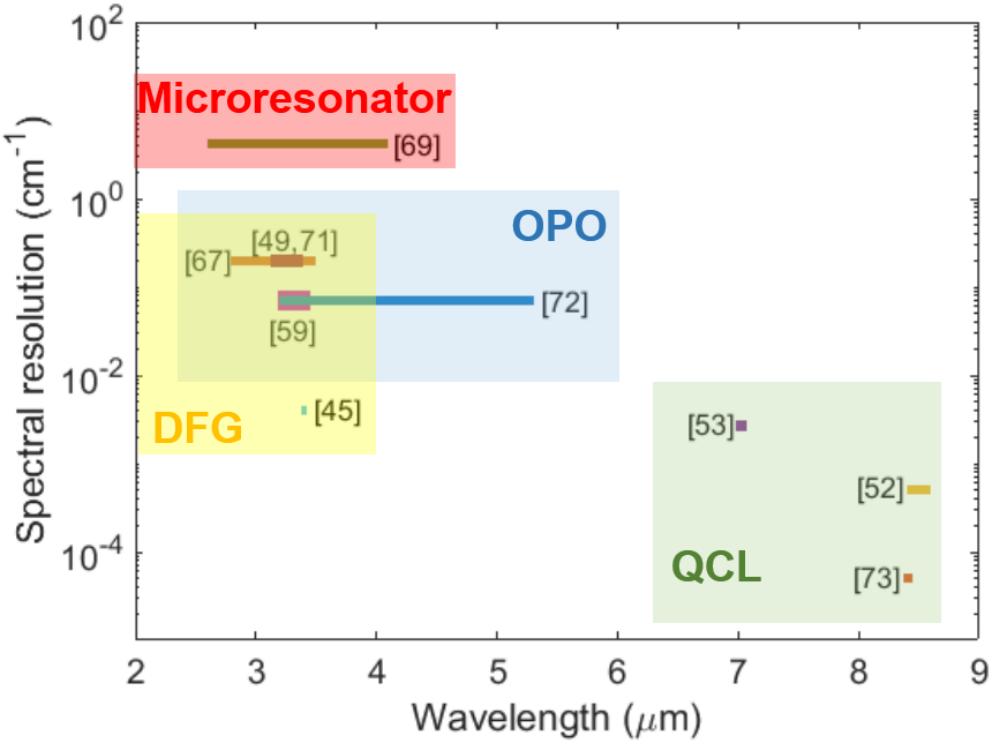

Figure 2.13: DCS demonstrations of microresonator, OPOs, DFG, and QCL with recent achievements including highest spectral resolutions among their results.

To date, most DCS systems have been reported in the near-infrared (near-IR) [42,61,62] because of the maturity of frequency-comb sources in this region [64-66]. The extension of DCS to the mid-IR has been achieved using difference-frequency generation (DFG) sources [59,67], quantum cascade lasers [52,53,68], micro-resonators [69], singly-resonant optical parametric oscillators (OPOs) [48,49,70,71] and doubly-resonant OPOs [72]. However, DCS in the mid-IR fingerprint region has been limited to an early demonstration using a μW-level DFG source, which achieved 2-cm^{-1} resolutions from 9–12 μm [39], and with a quantum-cascade laser comb, whose wide mode spacing required a multi-hour sweep of the comb-line positions in order to resolve molecular line-shapes over a 15-cm^{-1} range near 1420 cm^{-1} [53]. Indeed, quantum-cascade lasers are currently the only means of achieving moderately broadband high-resolution spectroscopy above 6 μm, with the technique of multi-heterodyne spectroscopy showing potential for coverage of tens of cm^{-1} [52] but with actual reported absorption spectroscopy only spanning < 1 cm^{-1} near 1190 cm^{-1} [73, 74].

Broadband multi-heterodyne spectroscopy also suffers from discontinuities in its spectral coverage, which arise from regions of the spectrum where the multi-heterodyne signal is weak, because FM modulation redistributes the power unevenly among the laser modes. Furthermore, properly resolving narrow line shapes requires scanning of the comb modes, which is time consuming and sacrifices the temporal resolution of the technique. These limitations can be circumvented by using new semiconductor nonlinear crystals to extend the wavelength coverage of near-IR femtosecond lasers to a region spanning from 6–12 μm [75]. This wavelength range is commonly known as the molecular 'fingerprint' region, where a wide range of organic compounds can be discriminated through the complex set of absorption features they exhibit due to molecular bending transitions.

2.6 References

1. T. Udem, J. Reichert, R. Holzwarth, and T. W. Hansch "Absolute optical frequency measurement of the cesium D-1 line with a mode-locked laser", Phys. Rev. Lett. 82 (18), 3568 (1999).

2. D. H. R. Telle, G. Steinmeyer, A. E. Dunlop, J. Stenger, D. H. Sutter, U. Keller, "Carrier–envelope offset phase control: a novel concept for absolute optical frequency measurement and ultrashort pulse generation", Appl. Phys. B 69, 327 (1999)

3. T. W. Hänsch, and N. Picqué. "Laser spectroscopy and frequency combs." *Journal of Physics: Conference Series*. Vol. 467. No. 1. (2013).

4. Jinendra K. Ranka, Robert S. Windeler, and Andrew J. Stentz, "Visible continuum generation in air–silica microstructure optical fibers with anomalous dispersion at 800 nm," Opt. Lett.25, 25-27 (2000)

5. T. A. Birks, W. J. Wadsworth, and P. St. J. Russell, "Supercontinuum generation in tapered fibers," Opt. Lett. 25, 1415-1417 (2000)

6. William J. Wadsworth, Arturo Ortigosa-Blanch, Jonathan C. Knight, Tim A. Birks, T.-P. Martin Man, and Phillip St. J. Russell, "Supercontinuum generation in photonic crystal fibers and optical fiber tapers: a novel light source," J. Opt. Soc. Am. B 19, 2148-2155 (2002)

7. S. G. Leon-Saval, T. A. Birks, W. J. Wadsworth, P. St.J. Russell, and M. W. Mason, "Supercontinuum generation in submicron fibre waveguides," Opt. Express 12, 2864-2869 (2004)

8. Mark A. Foster and Alexander L. Gaeta, "Ultra-low threshold supercontinuum generation in sub-wavelength waveguides," Opt. Express 12, 3137-3143 (2004)

9. Marco Bellini and Theodor W. Hänsch, "Phase-locked white-light continuum pulses: toward a universal optical frequency-comb synthesizer," Opt. Lett. 25, 1049-1051 (2000)

10. H. R. Telle, G. Steinmeyer, A. E. Dunlop, J.Stenger, D.H. Sutter, U. Keller., “Carrier–envelope offset phase control: a novel concept for absolute optical frequency measurement and ultrashort pulse generation”, Appl. Phys. B 69, 327 (1999)

11. D. J. Jones, S. A. Diddams, J. K. Ranka, A. Stentz, R. S. Windeler, J. L. Hall, S. T. Cundiff, "Carrier-Envelope Phase Control of Femtosecond Mode-Locked Lasers and Direct Optical Frequency Synthesis," Science 288, 635 (2000)

12. C. Grebing, S. Koke, B. Manschwetus, G. Steinmeyer, “Performance comparison of interferometer topologies for carrier–envelope phase detection”, Appl. Phys. B 95 (1), 81 (2009)

13. R. Jason Jones and Jean-Claude Diels, “Stabilization of Femtosecond Lasers for Optical Frequency Metrology and Direct Optical to Radio Frequency Synthesis,” Phys. Rev. Lett. 86, 3288 (2001)

14. S. B. Darack, G. T. Harvey, and D. R. Dykaar, "Timing-jitter stabilization of a colliding-pulse mode-locked laser by active control of the cavity length," Opt. Lett. 16, 1677-1679 (1991)

15. F. W. Helbing, G. Steinmeyer and U. Keller, "Carrier-envelope offset phase-locking with attosecond timing jitter," in *IEEE Journal of Selected Topics in Quantum Electronics*, vol. 9, no. 4, pp. 1030-1040 (2003)

16. M. Betz, F. Sotier, F. Tauser, S. Trumm, A. Laubereau, and A. Leitenstorfer, "All-optical phase locking of two femtosecond Ti:sapphire lasers: a passive coupling mechanism beyond the slowly varying amplitude approximation," Opt. Lett. 29, 629-631 (2004)

17. B. Borchers, S. Koke, A. Husakou, J. Herrmann, and G. Steinmeyer, "Carrier-envelope phase stabilization with sub-10 as residual timing jitter," Opt. Lett.36, 4146-4148 (2011)

18. A. Schliesser, N. Picqué, and T. W. Hänsch. "Mid-infrared frequency combs." *Nature Photonics* 6, 440-449 (2012)

19. Robert C. Eckardt, C. D. Nabors, William J. Kozlovsky, and Robert L. Byer, "Optical parametric oscillator frequency tuning and control," J. Opt. Soc. Am. B8, 646-667 (1991)

20. R.L. Byer, "Nonlinear optics and solid-state lasers", *Selected Topics in Quantum Electronics IEEE Journal of*, vol. 6, pp. 911-930 (2000)

21. R. Boyd, “Nonlinear Optis,” AcademicPress; 3 edition (2008)

22. M. Yamada, N. Nada, M. Saitoh, and K. Watanabe, “First-order quasi-phase matched $LiNbO_3$ waveguide periodically poled by applying an external field for efficient blue second-harmonic generation”, Appl. Phys. Lett. 62, 435 (1993)

23. K. Nakamura, J. Kurz, K. Parameswaran, and M. M. Fejer. "Periodic poling of magnesium-oxide-doped lithium niobate." *Journal of applied physics* 91, 4528-4534 (2002)

24. Manley, J. M., and H. E. Rowe. "Some general properties of nonlinear elements-Part I. General energy relations." *Proceedings of the IRE* 44.7, 904-913 (1956).

25. Teresa I. Ferreiro, Jinghua Sun, and Derryck T. Reid, "Frequency stability of a femtosecond optical parametric oscillator frequency comb," Opt. Express 19, 24159-24164 (2011)

26. J. H. Sun, B. J. S. Gale, and D. T. Reid, "Composite frequency comb spanning 0.4-2.4μm from a phase-controlled femtosecond Ti:Sapphire laser and synchronously pumped optical parametric oscillator," Opt. Lett. 32, 1414-1416 (2007)

27. Florian Adler, Kevin C. Cossel, Michael J. Thorpe, Ingmar Hartl, Martin E. Fermann, and Jun Ye, "Phase-stabilized, 1.5 W frequency comb at 2.8–4.8 μm," Opt. Lett. 34, 1330-1332 (2009)

28. Richard A. McCracken, Jinghua Sun, Christopher G. Leburn, and Derryck T. Reid, "Broadband phase coherence between an ultrafast laser and an OPO using lock-to-zero CEO stabilization," Opt. Express 20, 16269-16274 (2012)

29. K. Balskus, S. M. Leitch, Z. Zhang, R. A. McCracken, and D. T. Reid, "1-GHz harmonically pumped femtosecond optical parametric oscillator frequency comb," Opt. Express 23, 1283-1288 (2015)

30. Richard A. McCracken, Ilaria Gianani, Adam S. Wyatt, and Derryck T. Reid, "Multi-color carrier-envelope-phase stabilization for high-repetition-rate multi-pulse coherent synthesis," Opt. Lett.40, 1208-1211 (2015)

31. M. W. Haakestad, A. Marandi, N. Leindecker. and K. L. Vodopyanov, "Five-cycle pulses near $\lambda = 3$ μm produced in a subharmonic optical parametric oscillator via fine dispersion management". Laser & Photonics Reviews, 7: L93–L97. doi:10.1002/lpor.201300112 (2013)

32. Jinghua Sun and Derryck T. Reid, "Coherent ultrafast pulse synthesis between an optical parametric oscillator and a laser," Opt. Lett. 34, 854-856 (2009)

33. http://hyperphysics.phy-astr.gsu.edu/hbase/molecule/rotrig.html.

34. P. Atkins, and J. Paula. "*Elements of physical chemistry,"* Oxford University Press, USA (2013).

35. E. D. Becker, and T. C. Farrar. "Fourier transform spectroscopy." *Science* 178.4059, 361-368 (1972).

36. R. Bell. "*Introductory Fourier transform spectroscopy,"* Elsevier (2012).

37. B. C Smith, *Fundamentals of Fourier transform infrared spectroscopy*. CRC press (2011).

38. S. Schiller, "Spectrometry with frequency combs," Opt. Lett. 27, 766–768 (2002).

39. F. Keilmann, C. Gohle, and R. Holzwarth, "Time-domain mid-infrared frequency-comb spectrometer," Opt. Lett. 29, 1542–1544 (2004).

40. A. Schliesser, M. Brehm, F. Keilmann, and D. van der Weide, “Frequency-comb infrared spectrometer for rapid, remote chemical sensing,” Opt. Express 13, 9029–9038 (2005).

41. M. Brehm, A. Schliesser, and F. Keilmann, “Spectroscopic near-field microscopy using frequency combs in the mid-infrared,” Opt. Express 14, 11222–11233 (2006).

42. I. Coddington, W. C. Swann, and N. R. Newbury, “Coherent multiheterodyne spectroscopy using stabilized optical frequency combs,” Phys.Rev. Lett. 100, 013902 (2008).

43. B. Bernhardt, A. Ozawa, P. Jacquet, M. Jacquey, Y. Kobayashi, T. Udem, R. Holzwarth, G. Guelachvili, T. W. Hänsch, and N. Picqué, “Cavity-enhanced dual-comb spectroscopy,” Nat. Photonics 4, 55–57 (2010).

44. B. Bernhardt, E. Sorokin, P. Jacquet, R. Thon, T. Becker, I. T. Sorokina, N. Picqué, and T. W. Hänsch, “Mid-infrared dual-comb spectroscopy with 2.4 μm Cr2+:ZnSe femtosecond lasers,” Appl. Phys. B 100, 3–8 (2010).

45. E. Baumann, F. R. Giorgetta, W. C. Swann, A. M. Zolot, I. Coddington, and N. R. Newbury, “Spectroscopy of the methane ν3 band with an accurate midinfrared coherent dual-comb spectrometer,” Phys. Rev. A 84, 062513 (2011).

46. T. Ideguchi, A. Poisson, G. Guelachvili, T. W. Hänsch, and N. Picqué, “Adaptive dual-comb spectroscopy in the green region,” Opt. Lett. 37, 4847–4849 (2012).

47. T. Ideguchi, B. Bernhardt, G. Guelachvili, T. W. Hänsch, and N. Picqué, “Raman-induced Kerr-effect dual-comb spectroscopy,” Opt. Lett. 37, 4498–4500 (2012).

48. Z. Zhang, C. Gu, J. Sun, C. Wang, T. Gardiner, and D. T. Reid, “Asynchronous midinfrared ultrafast optical parametric oscillator for dual-comb spectroscopy,” Opt. Lett. 37, 187–189 (2012).

49. Z. Zhang, X. Fang, T. Gardiner, and D. T. Reid, “High-power asynchronous midinfrared optical parametric oscillator frequency combs,” Opt. Lett. 38, 2077–2079 (2013).

50. S. Potvin and J. Genest, “Dual-comb spectroscopy using frequencydoubled combs around 775 nm,” Opt. Express 21, 30707–30715 (2013).

51. T. Ideguchi, S. Holzner, B. Bernhardt, G. Guelachvili, N. Picqué, and T. W. Hänsch, “Coherent Raman spectro-imaging with laser frequency combs,” Nature 502, 355–358 (2013).

52. Y. Wang, M. G. Soskind, W. Wang, and G. Wysocki, “High-resolution multi-heterodyne spectroscopy based on Fabry-Perot quantum cascade lasers,” Appl. Phys. Lett. 104, 031114 (2014).

53. G. Villares, A. Hugi, S. Blaser, and J. Faist, “Dual-comb spectroscopy based on quantum-cascade-laser frequency combs,” Nat. Commun. 5, 5192 (2014).

54. S.-J. Lee, B. Widiyatmoko, M. Kourogi, and M. Ohtsu, “Ultrahigh scanning speed optical coherence tomography using optical frequency comb generators,” Jpn. J. Appl. Phys. 40, L878–L880 (2001).

55. A. M. Zolot, F. R. Giorgetta, E. Baumann, J. W. Nicholson, W. C. Swann, I. Coddington, and N. R. Newbury, “Direct-comb molecular spectroscopy with accurate, resolved comb teeth over 43 THz,” Opt. Lett. 37, 638–640 (2012).

56. S. Okubo, K. Iwakuni, H. Inaba, K. Hosaka, A. Onae, H. Sasada, and F.-L. Hong, “Ultra-broadband dual-comb spectroscopy across 1.0–1.9 μm,” Appl. Phys. Express 8, 082402 (2015).

57. H.-G. von Ribbeck, M. Brehm, D. W. van der Weide, S. Winnerl, O. Drachenko, M. Helm, and F. Keilmann, “Spectroscopic THz near-field microscope,” Opt. Express 16, 3430–3438 (2008).

58. S. Boudreau, S. Levasseur, C. Perilla, S. Roy, and J. Genest, “Chemical detection with hyperspectral lidar using dual frequency combs,” Opt. Express 21, 7411–7418 (2013).

59. F. Zhu, A. Bicer, R. Askar, J. Bounds, A. A. Kolomenskii, V. Kelessides, M. Amani, and H. A. Schuessler, “Mid-infrared dual frequency comb spectroscopy based on fiber lasers for the detection of methane in ambient air,” Laser Phys. Lett. 12, 095701 (2015).

60. P. R. Griffiths and J. A. Haseth, Fourier Transform Infrared Spectrometry, Wiley (2007).

61. Ian Coddington, Nathan Newbury, and William Swann, "Dual-comb spectroscopy," Optica 3, 414-426 (2016)

62. I. Coddington, W. C. Swann, and N. R. Newbury, "Coherent dual-comb spectroscopy at high signal-to-noise ratio," Phys. Rev. A 82, 043817 (2010).

63. I. Coddington, W. C. Swann, and N. R. Newbury, "Time-domain spectroscopy of molecular free-induction decay in the infrared," Opt. Lett. 35, 1395-1397 (2010).

64. L. C. Sinclair, I. Coddington, W. C. Swann, G. B. Rieker, A. Hati, K. Iwakuni, and N. R. Newbury, “Operation of an optically coherent frequency comb outside the metrology lab,” Opt. Express 22, 6996–7006 (2014).

65. J. Lee, K. Lee, Y.-S. Jang, H. Jang, S. Han, S.-H. Lee, K.-I. Kang, C.-W. Lim, Y.-J. Kim, and S.-W. Kim, “Testing of a femtosecond pulse laser in outer space,” Sci. Rep. 4, 5134 (2014).

66. L. C. Sinclair, J.-D. Deschênes, L. Sonderhouse, W. C. Swann, I. H. Khader, E. Baumann, N. R. Newbury, and I. Coddington, “Invited article: A compact optically coherent fiber frequency comb,” Rev. Sci. Instrum. 86, 081301 (2015).

67. F. C. Cruz, D. L. Maser, T. Johnson, G. Ycas, A. Klose, F. R. Giorgetta, I. Coddington, and S. A. Diddams, "Mid-infrared optical frequency combs based on difference frequency generation for molecular spectroscopy," Opt. Express 23, 26814-26824 (2015).

68. G. Villares, J. Wolf, D. Kazakov, M. J. Süess, A. Hugi, M. Beck, and J. Faist, “On-chip dual-comb based on quantum cascade laser frequency combs,” Appl. Phys. Lett. 107, 251104 (2015).

69. M. Yu, Y. Okawachi, A. G. Griffith, N. Picqué, M. Lipson and A. L. Gaeta, " Silicon-chip-based mid-infrared dual-comb spectroscopy," arXiv:1610.01121.

70. Y. Jin, S. M. Cristescu, F. J. M. Harren, and J. Mandon, "Two-crystal mid-infrared optical parametric oscillator for absorption and dispersion dual-comb spectroscopy," Opt. Lett. 39, 3270-3273 (2014).

71. Y. Jin, S. M. Cristescu, F. J. M. Harren and J. Mandon, "Femtosecond optical parametric oscillators toward real-time dual-comb spectroscopy," Appl. Phys. B 119, 65-74 (2015).

72. V. O. Smolski, H. Yang, J. Xu, K. L. Vodopyanov, " Massively parallel dual-comb molecular detection with subharmonic optical parametric oscillators," arXiv:1608.07318.

73. A. Hangauer, J. Westberg, E. Zhang, and G. Wysocki, "Wavelength modulated multiheterodyne spectroscopy using Fabry-Pérot quantum cascade lasers," Opt. Express 24, 25298 (2016).

74. L. A. Sterczewski, J. Westberg, and G. Wysocki, "Molecular dispersion spectroscopy based on Fabry–Perot quantum cascade lasers," Opt. Lett. 42, 243 (2017).

75. L. Maidment, P. G. Schunemann, and D. T. Reid, "Molecular fingerprint-region spectroscopy from 5 to 12 μm using an orientation-patterned gallium phosphide optical parametric oscillator," Opt. Lett. 41, 4261-4264 (2016).

Chapter 3 - Mid-IR Dual Comb Spectrometer with PPLN-based OPOs

Mid-IR optical frequency comb spectroscopy is a prominent potential tool for rapid measurements of broadband molecular spectra, principally because of the multitude of fundamental molecular vibrations in the mid-infrared region from 500-5000 cm^{-1} (2-20 µm), but its development has up to now been constrained by the quality of suitable mid-IR light sources and the stability requirements of the related optical frequency combs. Consequently, the performance of dual-comb spectroscopy in the mid-infrared wavelength region, and that of mid-infrared frequency combs, is still poorer than those in the near-infrared region where most demonstrations on direct frequency comb spectroscopy have been reported [1,2]. In this chapter a mid-infrared dual-comb spectrometer (DCS) is reported for fundamental gas absorption spectroscopy by using two independent picosecond optical parametric oscillators pumped by two identical Yb:fibre lasers. The demonstrated mid-IR spectrometer is able to deliver a broad range of wavelengths suitable for identifying many gases and molecules.

3.1 Fibre laser design and characterization

Fibre lasers are typically those that employ optical fibres as the gain medium, in contrast to those lasers e.g. with a semiconductor gain medium, like a semiconductor optical amplifier, and a fibre resonator, which have also been referred to as fibre lasers. In order to build a laser resonator with fibres, one either requires some kind of reflectors (mirrors) to form a linear resonator (Fig. 3.1a), or one designs a fibre ring cavity (Fig. 3.1b).

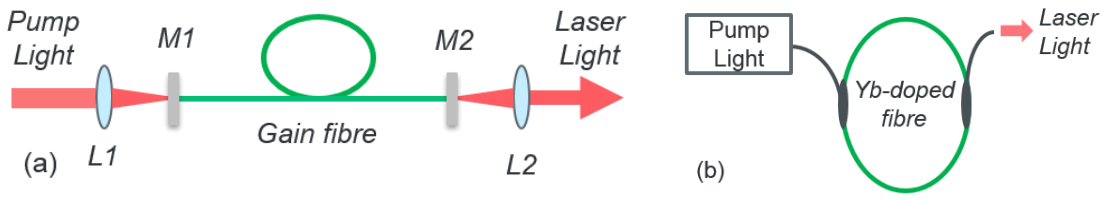

Figure 3.1: Generic designs of a simple fibre laser. Pump light is launched from the left-hand side through a dichroic mirror M1 into the core of the doped fibre and the generated laser light is extracted through M2 on the right-hand side from linear cavity (a). Alternatively, pump light is directly coupled into a fibre ring cavity with a fibre coupler and the generated light is extracted from a fibre output coupler (b).

The gain medium of a fibre laser is a fibre doped with rare earth ions such as erbium (Er^{3+}), neodymium (Nd^{3+}), ytterbium (Yb^{3+}), thulium (Tm^{3+}), or

praseodymium (Pr^{3+}), and pumped by one or several fibre-coupled laser diodes [3]. Unlike diode-pumped solid-state bulk lasers, the light propagates with small effective mode area, which means the light is guided through fibre, and therefore they often operate with much higher laser gain and resonator losses. In addition the intracavity conditions for modelocking and saturable absorption effects can differ significantly from solid-state lasers.

3.1.1 *Modelocked fibre lasers*

The advanced resonator designs are considered particularly for mode-locked fibre lasers, when generating picosecond or femtosecond pulses. Such ultrashort pulses are generated by fibre lasers either using active or passive modelocking. Here, the laser cavity includes either an active modulator or some kind of saturable absorber [4,5]. Such saturable absorption can be achieved using the effect of nonlinear polarization rotation, or a nonlinear fibre loop mirror [6,7]. The performance of picosecond and femtosecond mode-locked fibre lasers is substantially limited by the strong nonlinearities and uncontrolled birefringence of fibres, and sometimes also by the intracavity chromatic dispersion in many cases.

The general aspects of ultrashort pulses generated by active mode-locking involve active modulation of intracavity losses or of the round-trip phase change. These effects are controlled by using an acousto-optic or electro-optic modulator, a Mach-Zehnder integrated-optic modulator, or a semiconductor electro-absorption modulator inside the resonator (Fig. 3.2). Once the modulation is synchronized with the resonator round trips, this supports the generation of ultrashort pulses.

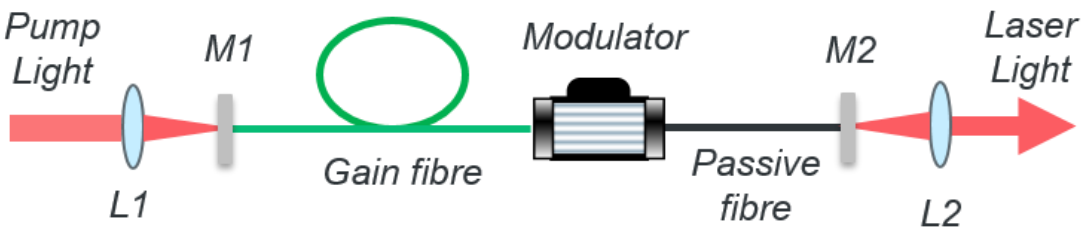

Figure 3.2: Schematic setup of an actively mode-locked fibre laser shown in a linear cavity. M, mirror; L, lens.

The pulse durations achieved by actively mode-locked fibre lasers are typically in the picosecond range. This limitation is determined by the strength of the modulation signal which arises from the fact that the pulse-shortening effect is limited by the performance of the modulator.

Passively mode-locked fibre lasers appeared in the early 1990s and a number of laser designs have been investigated since then. When an element whose transmittance rapidly changes depending on the optical power is introduced into the laser cavity, ultrashort pulse oscillation can be achieved spontaneously. Since the phase of each oscillation mode is automatically adjusted and synchronized by this element in this process, this phenomenon is called passive mode-locking (Fig. 3.3) [8]. The nonlinear optical Kerr effect in optical fibres, and/or a saturable absorber (SA) are commonly used as such intensity-dependent elements in the fibre laser cavity. This element and its parameters are chosen according to requirements of the laser properties. A fast saturable absorption achieved without semiconductor materials in the laser cavity is called nonlinear polarization evolution (NPE) due to the optical Kerr nonlinearities in optical fibres. This phenomenon is simply managed with an appropriate choice of a polarizing beam splitter and a few waveplates [9].

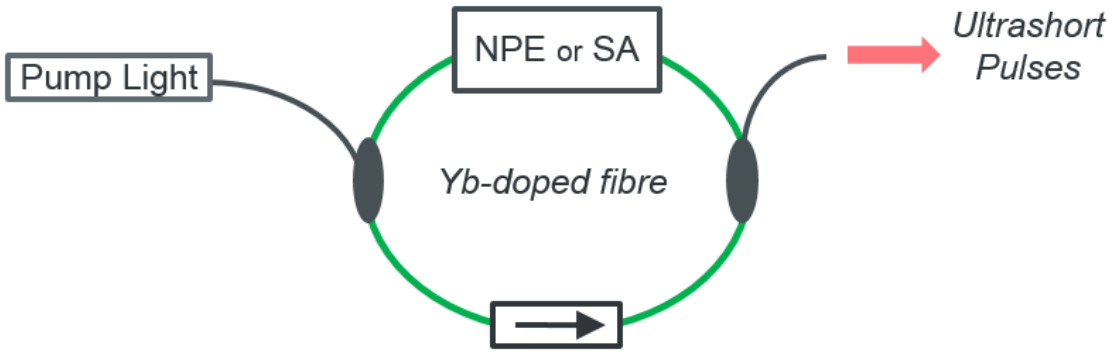

Figure 3.3: Typical setup of a passively mode-locked fibre laser. Mode-locking is achieved by either nonlinear polarization evalution (NPE) or saturable absorber (SA).

Various kinds of ultrashort pulse configurations, such as solitons (chirp-free $sech^2$-shaped solitary pulse), similaritons (parabolic-shaped pulse with linear chirping), and dissipative solitons (linearly chirped high-energy pulse with steep edges on the pulse spectra), are obtained by using these intensity-dependent devices in the fibre laser cavity, and by controlling the dispersion property and nonlinearity in the cavity adequately.

3.1.2 *All-normal dispersion Yb:fibre oscillator*

All-normal dispersion (ANDi) fibre lasers have found broad usage due to their simplicity, compactness and higher pulse energies [10]. There is strong motivation to evaluate their suitability for frequency comb generation. Their self-starting behaviour and intrinsic passive stability makes them attractive pump sources for OPOs [11]. In this section, two highly efficient, identical picosecond ANDi Yb fibre ring oscillators, which are capable of generating separately an octave-spanning super-continuum at 102 MHz are presented in detail.

The laser cavity configuration is presented in Fig. 3.4. A 980 nm fiber-pigtailed diode laser, was combined with a 10-cm-long fibre Bragg grating in order to shift the diode laser center wavelength to the efficient absorption wavelength which is 976 nm for Yb gain [12]. The fibre section consisted of a 28 cm length of Yb fibre (Liekki; SM 1200-4/125) with fiberized wavelength division multiplexing (WDM) (AFW Technologies; FWDM-9830-B-H-1-0-1). The collimators (AFW Technologies; C-SM-64-1-1-1-50-B-OC-CL-1) had a length of 167 cm single mode passive fibre (Nufern; SM HI1060), giving a total fibre length of ~ 195 cm. An output collimator was placed onto a translation stage with a piezoelectric actuator (Thorlabs; PZS001) so that repetition rate could be controlled precisely. The free-space part of the cavity was ~16 cm long, where one half-wave plate (Singapore Optics; WP-05M-ZH-1064) and two quarter-wave plates (Singapore Optics; WP-05M-ZQ-1064) are assembled to obtain mode locking via nonlinear polarization evolution (NPE) assisted by spectral filtering [10]. The interference filter (Edmund Optics) had a bandwidth of 10 nm and was slightly angled to transmit a centre wavelength of 1050 nm. The NPE rejection port through the polarization beam-splitting cube (Thorlabs; PBS103) was used as the laser output.

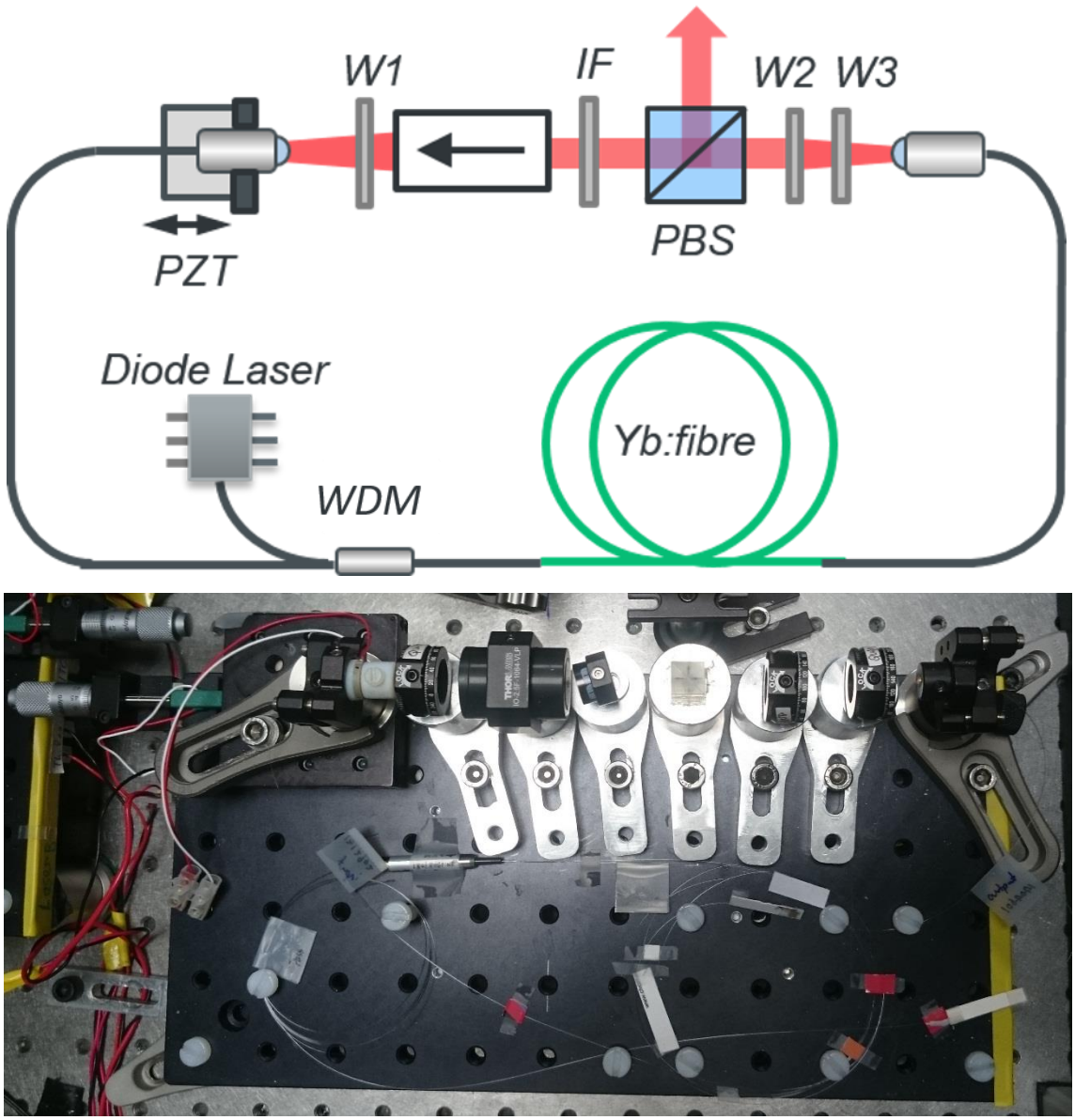

Figure 3.4: ANDi Yb:fiber master oscillator in generic sketch (top) and picture (bottom). Cavity is designed a form of circular with NPE section in which mode-locking is performed by changing waveplates. W1, quarter-wave plate; W2, half-wave plate; W3, quarter-wave plate; IF, interference filter; PBS, polarization beam splitter cube; PZT, piezo-transducer.

Both ANDi Yb fibre lasers delivered respectively mode-locked output powers of 156 mW and 152 mW at a repetition rate of approximately 102 MHz, corresponding to an optical-to-optical efficiency of ~53%. The optical spectra of the chirped pulses from both oscillators directly after the laser cavities are shown in Fig. 3.5. Both lasers were very stable in operation and self-starting.

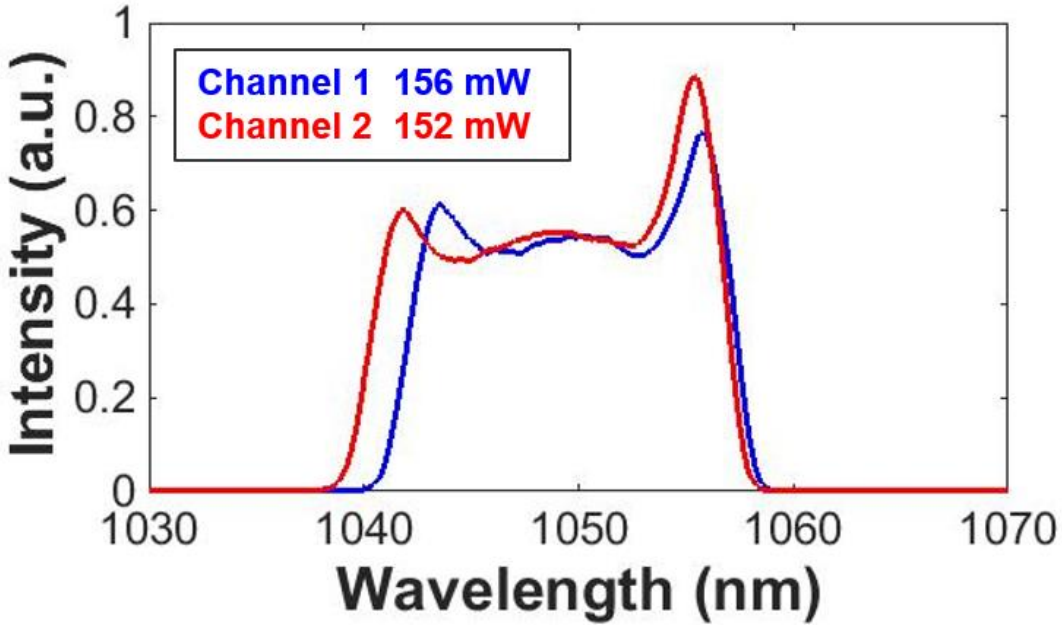

Figure 3.5: Optical spectra from the two master oscillators. Each oscillator delivers power more than 150 mw.

3.1.3 *Yb: fibre chirped-pulse amplifier*

Two amplification schemes exist for amplifying ultra-short optical pulses: chirped-pulse amplification (CPA) and direct amplification [3]. A CPA system consists of a pulse stretcher, power amplifier and a pulse compressor. The pulse stretcher elongates the pulse in the time domain, i.e., reduces the peak power of the pulse. This helps to alleviate or avoid the nonlinear effects in the amplifier gain media. CPA has the potential to amplify the optical pulses to very high peak power while maintaining the pulse quality, however the stretcher and compressor introduce significant loss, and add complexity to the system. On the contrary, for direct amplification, the ultra-short pulses are amplified straight from the oscillator, allowing a simpler, more efficient optical scheme to be implemented. During amplification, nonlinear effects, which are principally self-phase modulation (SPM) for an ultra-short pulse fibre amplifier, may accumulate. However, for moderate power amplification, the SPM-induced deterioration of pulse-quality and wave-breaking may be acceptable (and even beneficial) for many applications [13].

Fiber amplifiers can be pumped either in the forward direction, or in the backward direction, or bidirectionally. The direction of the pump wave does not affect the small-signal gain, the power efficiency of the saturated amplifier, and the noise characteristics [14]. In order to take into account parasitic propagation losses in long fibers, the signal becomes strong near near the pump input end in terms of holding the excitation density

down in that region by backward pumping, so that the pump light is efficiently absorbed by the ions. But since amplified spontaneous emission (ASE) in fibre amplifier propagates in the same direction as signal, it becomes stronger and effectuates a broadband noise [15]. Although backward pumping helps power conversion efficiency, forward pumping is better for low-noise operation. Bidirectional pumping can be also considered to achieve a low noise figure and a high power efficiency at the same time.

The schematic of the fibre amplifier which was designed and constructed for this work is shown in Fig. 3.6. Each seed signal from the mode-locked Yb fiber laser require no additional stretcher because the pulses from the ANDi lasers were sufficiently chirped already to remove the need for any additional stretcher here. The signal from each oscillator was directly coupled into the core of a single-mode fibre (with a core diameter of 10 µm and NA of 0.075) with the help of an aspheric lens, after passing through a pair of lenses to reduce its beam size, an isolator and a half-wave plate.

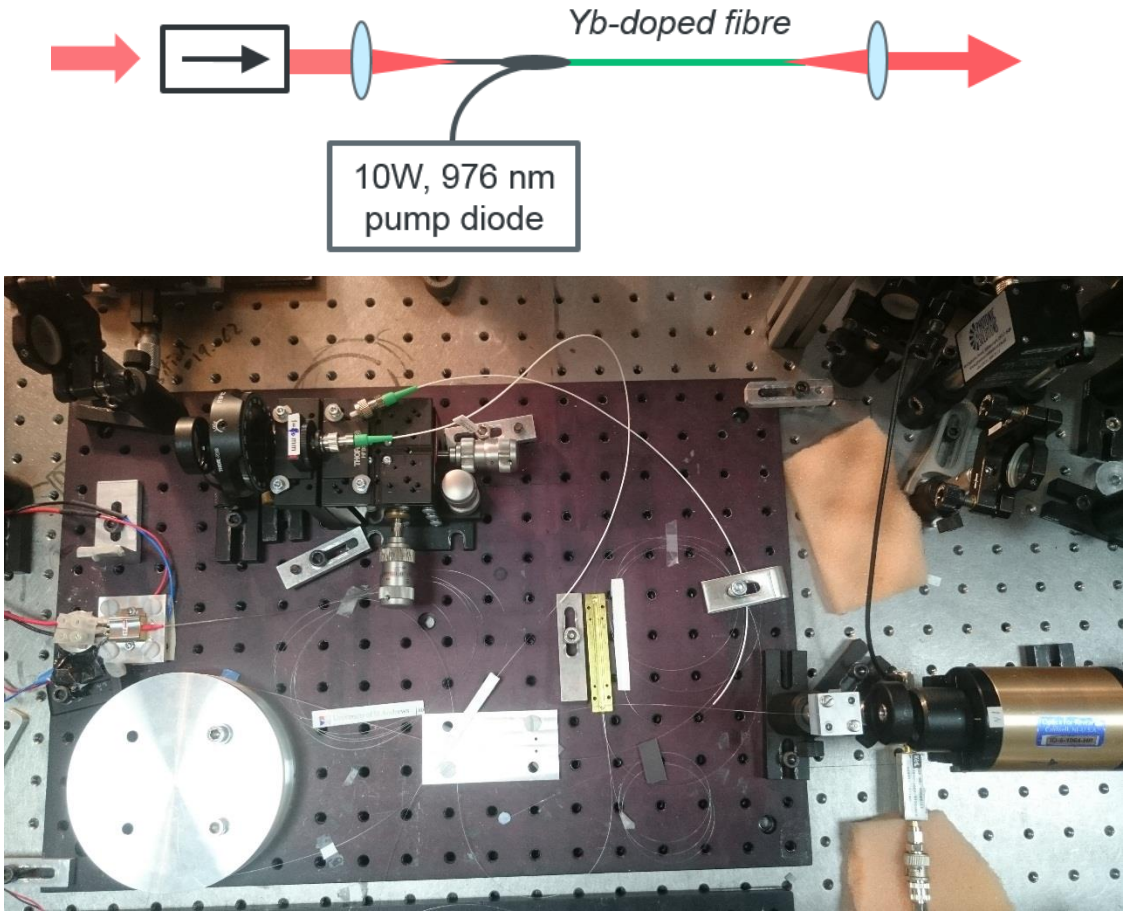

Figure 3.6: Yb fibre chirped pulse amplifier seeded by an ANDi Yb:fibre oscillator (described in the previous section).

The amplifier was pumped by a 9-W, 976-nm fibre-coupled diode laser (with a fibre core diameter of 105 um and NA of 0.22). A fibre pump/signal combiner combined the single-

mode signal and the multi-mode pump into a Yb-doped double-cladding fibre (DCF). The signal was guided and amplified in the single-mode Yb-doped core, while the pump propagated inside the inner cladding (including the core) and was absorbed by the Yb ions doped in the core. Both the seed coupling and output ends of the fibre were angle-cleaved to avoid lasing of the amplifier. The Yb-doped DCF in each system had a core diameter of 10 µm and NA of 0.075, a cladding diameter of 125 µm and NA of 0.22. These fibres were individually 1.93 m and 1.91 m long, with an absorption coefficient of ~7.7 dB m^{-1} at 976 nm.

The average output power from each of the mode-locked Yb fiber oscillators was approximately 155 mW, and the transmission of the isolator was ~ 86%. With a coupling efficiency of more than 70%, we can estimate that ~ 105 mW signal was coupled into the core of the fibre. The pump loss through the pump/signal combiner was ~ 0.5 dB, and ~90% pump power was absorbed by the fibre amplifier. Therefore, with a 7.2 W pump power from the pump diode, approximately 5.8 W was absorbed by the Yb-doped fibre, and 2.9 W output power was obtained from the amplifier. The amplifier output power versus the absorbed pump power is shown in Fig. 3.7. The slope efficiency was 59.4%.

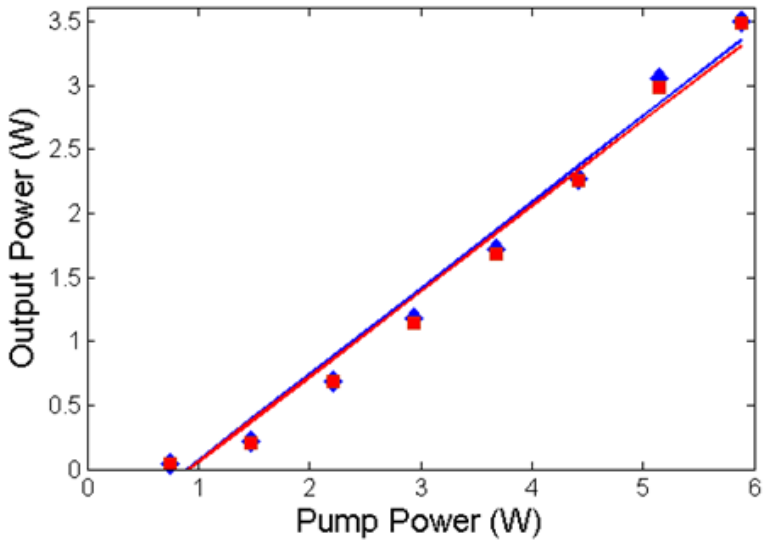

Figure 3.7: Power conversion in the fibre amplifier. The thresholds of two identical systems for amplification were investigated and found to have a power of less than 500 mW per channel.

The spectrum of the amplifier output is shown in Fig. 3.8. The output spectra of the fibre amplifier became broader with the increase of the output power due to self-phase modulation in the fibre amplifier. The central wavelength of the fibre amplifier output was red-shifted because the seed central wavelength of ~1049 nm significantly deviates from the amplifier gain peak. At the approximate output power of 1.5 W from the

amplifier, the FWHM of the spectrum was 25 nm and the central wavelength was 1054 nm. Pulse durations at this power level were measured with an intensity autocorrelator [16,17] and calculated to be 3.9 ps as chirped.

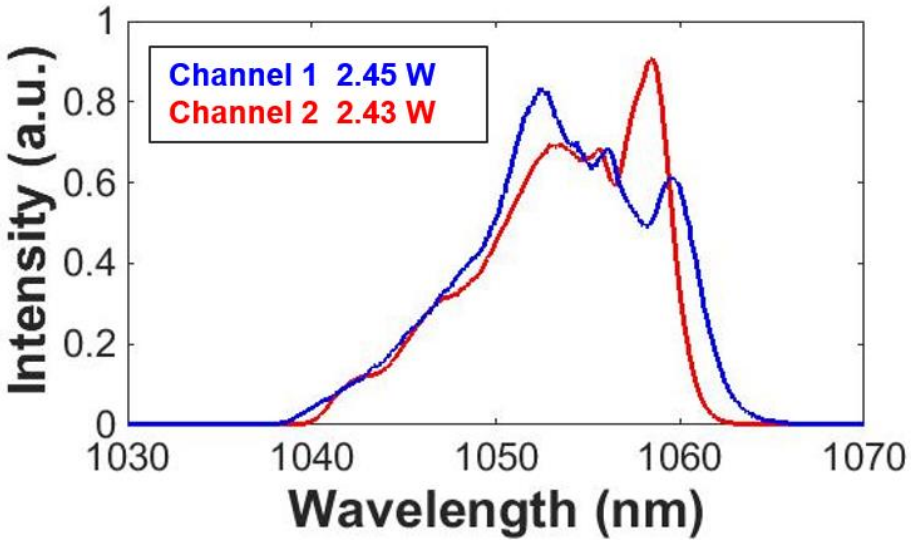

Figure 3.8: Optical spectrum of both amplifier outputs. The average power of each channel is approximately 2.45 W.

3.2 Optical parametric oscillator design and characterization

The optical parametric oscillators (OPO) are here essential parts of a dual-comb spectrometer. First generation OPOs were designed with MgO:PPLN crystal to supply broad mid-infrared spectra where gas absorption spectroscopy will be performed. Their performance analysis is necessary to understand its figure of merit and vulnerabilities entirely.

3.2.1 *Periodically poled lithium niobate*

Periodically poled lithium niobate (PPLN) is a nonlinear crystal for parametric wavelength conversion processes, specially frequency doubling, difference frequency generation, sum frequency generation, and optical parametric oscillation [18-21]. The orientation of the lithium niobate crystal is periodically poled to manage quasi-phase-matching. The inverted portions of the crystal manipulates generated photons that are π out of phase with the generated photon that would have been existed at that point in the crystal if it had not been poled as explained in Section 2.2.1. Thus, the recently generated photons basically interfere constructively with previously generated photons in specifically choosen periodicity with which to flip the orientation of the crystal, and as a

result, the number of generated photons is produced with a high conversion efficiency of input to generated photons by the light propagating through the PPLN [22].

The concept of PPLN fabrication is the process by which the crystal structure of Lithium Niobate is inverted (Fig. 3.9). Lithium niobate is a ferroelectric crystal, where each unit cell has a small electric dipole moment and the electric dipole is orientated by the positions of the niobium and lithium ions in that unit cell. By applying an intense electric field into a unit cell the crystal structure is inverted due to the orientation of the electric dipole. To fabricate PPLN, a periodic electrode structure is deposited on the lithium niobate wafer, and a voltage (~22kV/mm) is applied to invert the crystal underneath the electrodes [23]. The design of the electrodes is key to engineering periodicity in different lengths of PPLN crystals.

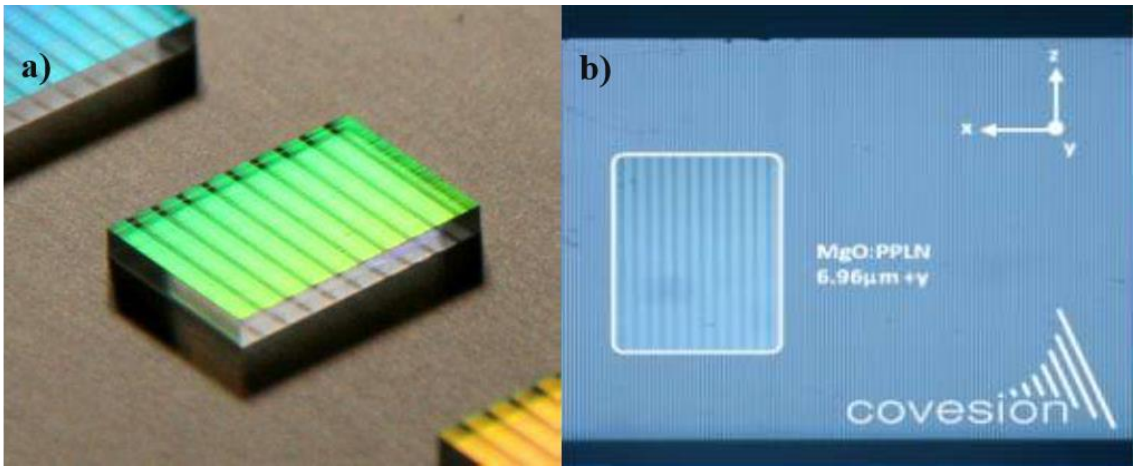

Figure 3.9: MgO doped PPLN crystal with consistent domain structure along thickness [24].

PPLN is a well studied nonlinear crystal in optical parametric oscillators [24-30]. A schematic of such an OPO is shown in Fig. 3.10. The converted wavelengths are determined by energy conservation and phase matching. The sum of the energy of a signal photon and an idler photon must equal the energy of a pump photon, as determined by energy conservation. By using PPLN with a different poling period or changing the PPLN temperature, the combination of wavelengths that is quasi-phase matched, and hence referred to as the operation wavelength, may be tuned over a wide range. It is commonly pumped with a 1-µm laser to produce signal and idler beams at wavelengths between 1.3 and 5µm. PPLN based OPOs can deliver output powers of several watts and can be pumped with pulsed or CW pump lasers.

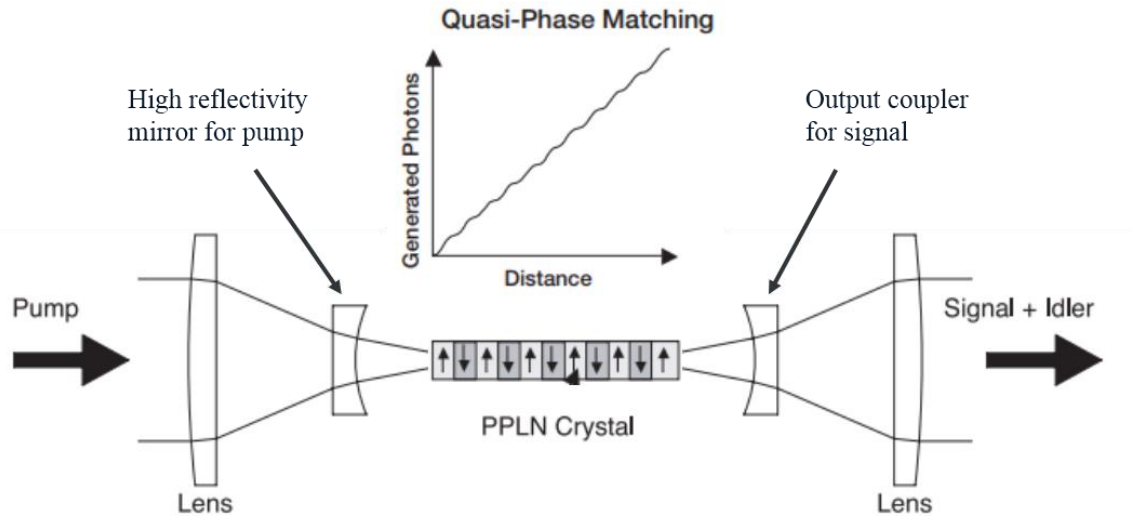

Figure 3.10: Optical parametric oscillation with a PPLN crystal. Cavity mirrors support oscillation for nonlinear conversion into signal and idler with relatively low pump power.

3.2.2 *Singly resonant MgO:PPLN based OPOs*

The OPO design followed an approach similar to that described by Zhang *et al.* [31]. Each OPO incorporated a 20-mm-long and 1 mm thick 5 mol.% MgO:PPLN crystal, located in an aluminium heat sink maintained at 30 °C. The MgO doping of the PPLN crystal decreases the photorefractive effect that can damage the crystal and cause the output beam to be distorted [32]. The crystal consisted of 9 periodically poled gratings and its periods were between 27.91 μm and 31.59 μm. Each grating was 0.5 mm wide with individual periods. Each poled grating was separated by 0.2 mm wide regions of unpoled material. The temperature control of the crystal also minimized the photorefractive effect and avoided fluctuations of the refractive index of the crystal. The choice of such a long crystal is unusual for a system supporting femtosecond pulse bandwidths, however it provides a number of important benefits. Firstly, the long crystal provides a group-delay between the pump and signal pulses which is well matched to the durations of the chirped pump pulses. This leads to high parametric conversion efficiency, as the intracavity signal pulse walks through the broad pump pulse on each transit of the crystal. Next, the high intracavity dispersion resulting from the long MgO:PPLN crystal means the OPO tunes very slowly with cavity length, conferring excellent passive power and wavelength stability. Finally, as illustrated in Fig. 3.11, the phase-matching characteristic of this crystal means that the entire pump bandwidth (13 nm / 3.5 THz) is phase-matched to a much narrower signal bandwidth (4 nm / 0.5 THz) at a grating period of 30.49 μm. Consequently, this scheme enables almost complete parametric transfer of the pump bandwidth to the idler pulses, providing the necessary spectral coverage for methane spectroscopy.

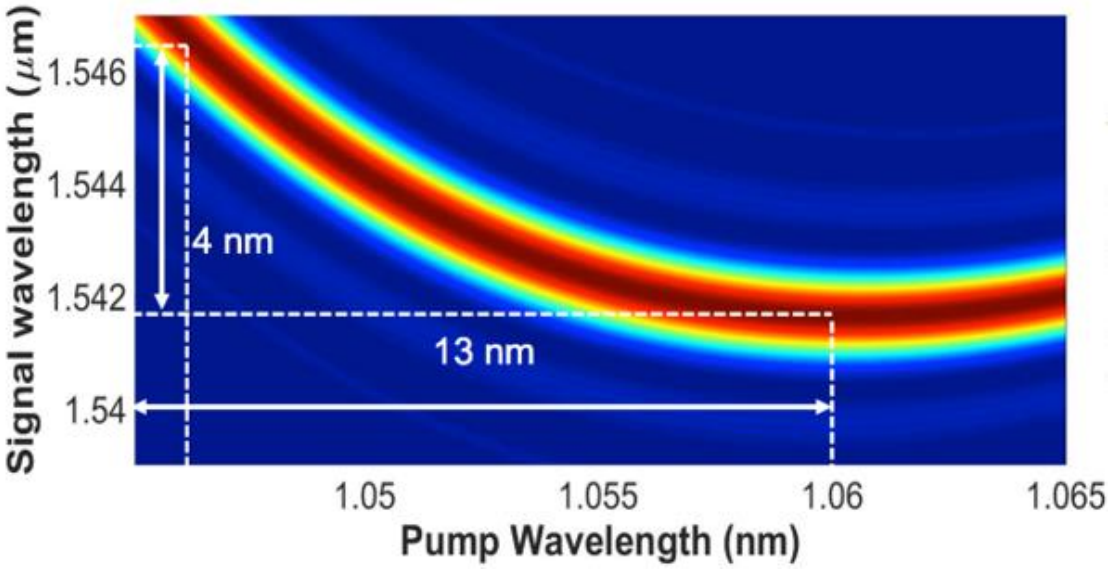

Figure 3.11: Phasematching efficiency map of the 20-mm MgO:PPLN crystal (Λ= 30.49 μm), showing how a broad pump bandwidth is phase-matched to a substantially narrower signal bandwidth. In the color-map, red corresponds to maximum efficiency and blue to zero efficiency.

Figure 3.12 shows the developed Yb-fiber laser pumping the singly resonant optical parametric oscillator system in a standing-wave cavity design (linear cavity). The pump source was described in Section 3.2 and 3.3. Chirped pulses (3.9 ps) with powers of approximately 1 W were sent through OPO. A lens (L1) with a focal length of 75 mm focused the pump pulses onto the nonlinear crystal (MgO:PPLN; Covesion). The OPO cavity consisted of two concave mirrors with a radius of -150 mm (M1, M2), three highly reflective plane mirrors coated on YAG substrates for high transmission at the pump and idler wavelengths (T> 90% at 1020–1110 and 2300–3700 nm) and high reflectivity at the signal wavelength (R > 99.8% at 1400–1800 nm), and an output coupler (T~15% at 1.35-1.6 μm). One of the plane mirrors was mounted on a piezo which had a 4.6 μm stroke. The OPO cavity length could be tuned by translating the highly reflective mirror with the piezo to control the cavity delay. The OPO was singly resonant for the signal, which was extracted through a 15% output coupler (OC) which was chosen to be able to obtain maximum idler power. The idler pulses were transmitted through a mirror (M2) and collimated with a CaF_2 lens (L2) following which an antireflection-coated Ge window was used to filter depleted pump pulses and leaked signal pulses whilst transmitting the idler pulses prior to monitor and spectroscopy.

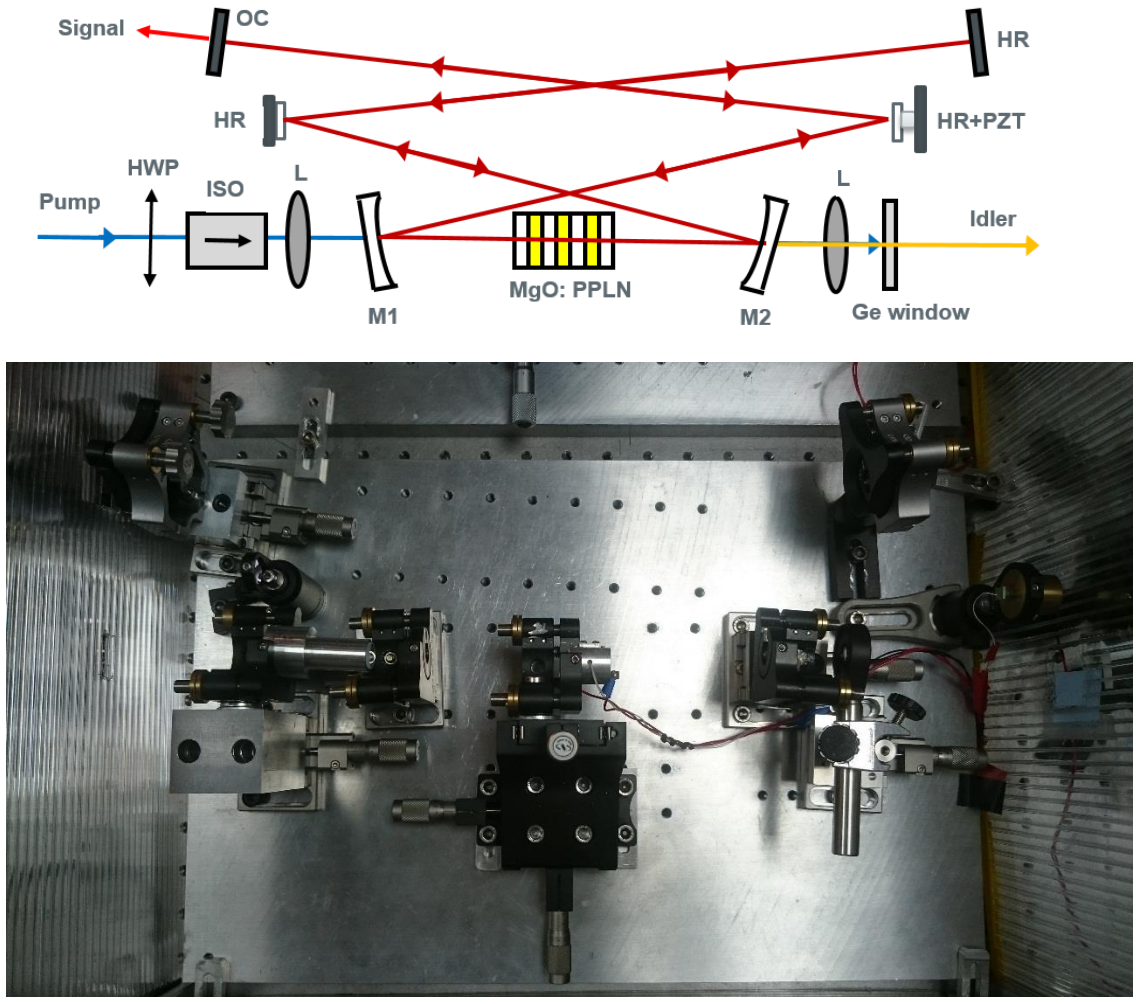

Figure 3.12: Singly resonant PPLN based OPO pumped by ANDi Yb:fibre laser in generic design (top) and picture (bottom).

The spectral properties of the OPO were characterized by a Fourier transform optical spectrum analyzer (Thorlabs OSA205), which offered a maximum spectral resolution of 0.25 cm^{-1} (7.5 GHz). Idler spectra are shown at a resolution of 2 cm^{-1} in Figure 3.13, for six out of seven of the poling periods of the PPLN crystal; the shortest grating period which produced insufficient power. The maximum spectral width of the idler was approximately 200 nm (185 cm^{-1}), centred at 3.3 µm. The low threshold and slow carrier-envelope phase shift with chirped pulses were yielded by using the long crystal length and the intra-cavity dispersion management. The long crystal also supports very large positive GVD in the signal wavelength region that induces significant pulse-broadening effects. With a grating period of 30.49 µm in the OPO crystal and a pump power of 2.45 W, the idler power reached over 150 mW, corresponding a pump-to-idler conversion efficiency of ~6.5%. At longer wavelengths, the threshold became higher due to the lower reflectivity of the cavity mirrors for the longer signal wavelengths and the higher absorption in the PPLN crystal.

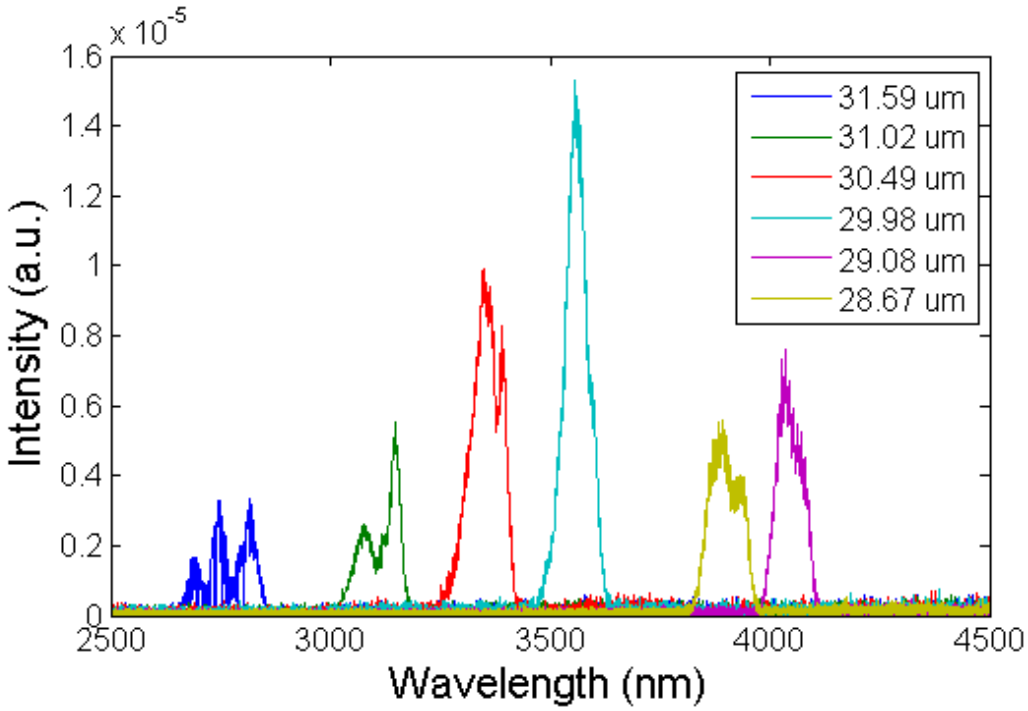

Figure 3.13: Idler spectra of each OPO in PPLN grating periods between 28.67 and 31.59 µm. There is strong water absorption at around 2.8 µm.

With a 15% OC, the threshold for oscillation was less than the pump power of 150 mW, and Fig. 3.14 (left) shows the measured signal / idler powers. Fig. 3.14 (right) shows the signal spectrum of the OPO whose central wavelength is 1543.3 nm generated by using a grating period of 30.49 µm and FWHM was measured to be 3 nm. The pump bandwidth is parametrically transferred into narrower spectrum compared to the pump bandwidth due to the relatively long MgO:PPLN grating. Furthermore, the idler spectra is expected to be broad in that case, because the pump spectrum is the convolution of the signal and idler spectra, and almost the full width of the pump spectrum was depleted in the OPO [31].

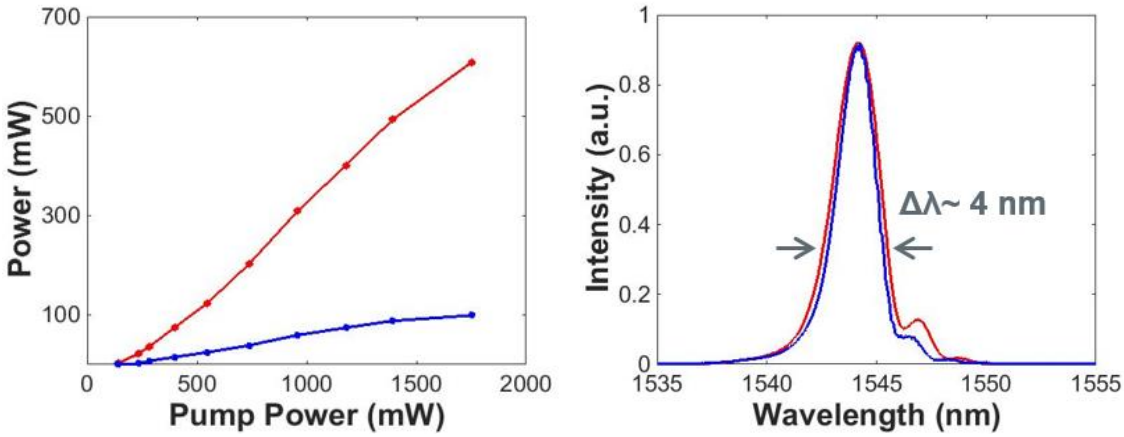

Figure 3.14: Output powers from the signal (blue) and idler (red) channels of one OPO, implying slope efficiencies of 39.5 % and 6.7 % for the signal and idler channels respectively (Left). Signal spectra from both OPOs (right).

3.3 Laser pulse repetition frequency stabilization

The pulse repetition rate (or pulse repetition frequency) f_{rep} of a pulse sequence is described as the number of emitted pulses per second, or the inverse temporal pulse spacing. A regular train of pulses that are mutually coherent results in a frequency comb in the optical spectrum, where the spacing of the lines is determined by the pulse repetition rate:

$$f_{rep} = \frac{c}{L} \tag{3.1}$$

where c is speed of light and L is the roundtrip cavity length of the oscillator.

In this section, how f_{REP} can be electronically stabilized to create a pair of combs whose comb-mode spacings are precisely controlled and thus suitable for dual-comb spectroscopy will be described. This was accomplished by employement of a direct digital synthesizer.

3.3.1 *Modelocked laser cavity length control*

Control of the laser repetition frequency is one of the most important aspects of the laser system in terms of its applications. This is managed by tuning the cavity length of the oscillator precisely. One of most common methods used in a modelocked fibre laser is to control the fibre length inside the oscillator by using a fibre stretcher or fiber-coupled optical modulator [33], but most fibre stretchers or optical modulators are limited by a short scanning range and slow response. Another disadvantage with these methods is the distorted spectrum that can accompany them and this becomes more important in spectroscopy applications when applying pressure onto the fibre. The other most common method is a movable mirror or stage in the free-space part of the laser cavity [34]. Although this method is convenient for long-range adjustment, fast response in terms of the piezo and easy implementation with a piezo mounted on a mirror or collimator, it comes with some disadvantages of a higher exposure to environmental influences, e. g. dust and mechanical perturbations typically.

Mechanical constraints with a movable stage inside an oscillator design basically become significant when the clamping force onto the piezo is approached or exceeded due to its weight or the spring force of the stage or mirror. This issue was overcome by using a very

light 3D printed collimator mount for attaching the input collimator to the PZT (Noliac, NAC2123) whose blocking force was 3560 N and whose resonant frequency was 483 kHz with a maximum scanning range of 3.3 µm (Fig. 3.15). This PZT was able to be driven with up to 200 V for optimal movement over its scanning range.

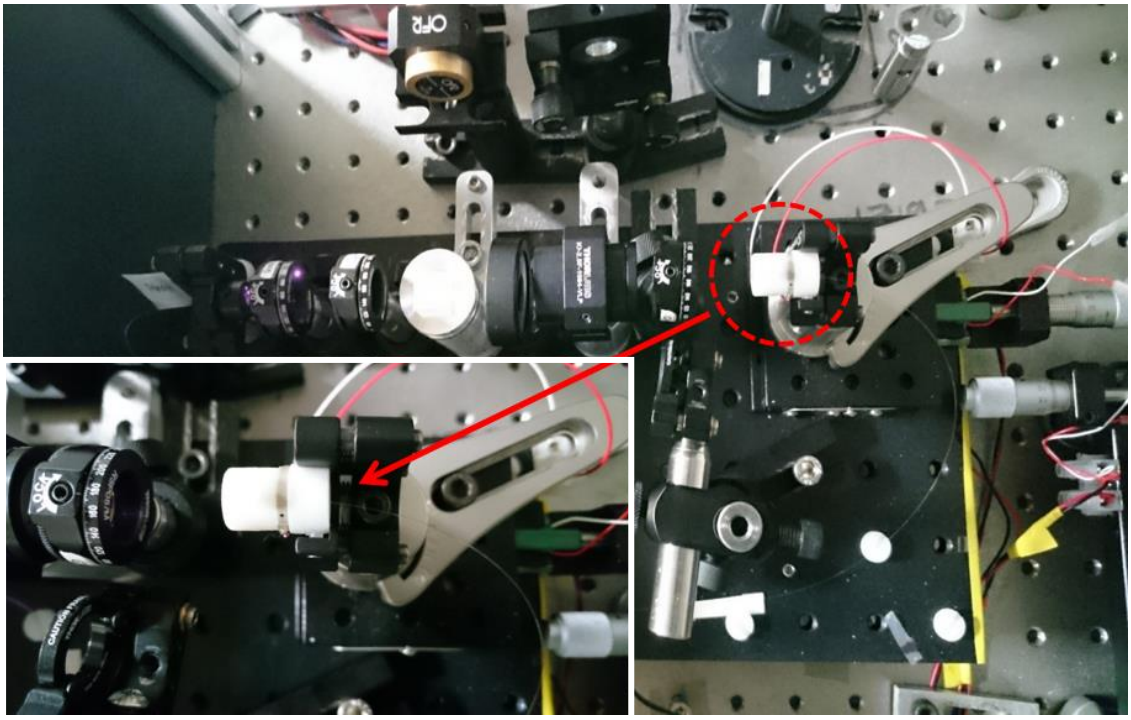

Figure 3.15: Ring piezo inserted on 3D printed collimator mount.

3.3.2 *Laser repetition frequency stabilization of two modelocked lasers using direct digital synthesis*

A digitally-controlled method to generate multiple frequencies from a reference frequency source has been developed, called direct digital synthesis (DDS) [35]. The basic architecture is shown in Figure 3.16. In this generic model, a programmable-read-only-memory (PROM) driven by a stable clock accumulates one or more integral number of cycles of a sinewave (or other arbitrary waveform, for that matter). As the address counter steps through each memory location, a digital-to-analog converter (DAC) driven by the corresponding digital amplitude of the signal at each location, in turn, generates the analog output signal.

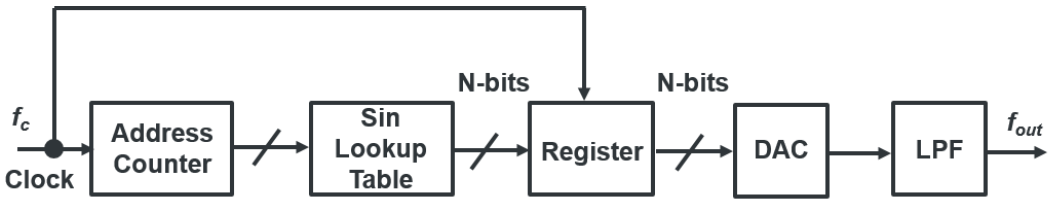

Figure 3.16: Fundamental principle of direct digital synthesis system. LPF, low-pass filter.

DDS generates a sine wave at a set frequency. The frequency is composed of two variables, the reference-clock frequency and the binary number programmed into the frequency register (M, tuning word). The main input to the phase accumulator is determined by the binary number in the frequency register. When sine look-up table is required, the phase accumulator computes a phase (angle) address for the look-up table, which outputs the digital value of amplitude corresponding to the sine of that phase angle to the DAC. In turn the DAC converts that digital number to a corresponding value of analog voltage or current. With each clock cycle, the phase increment which is determined by the binary number is added to the phase accumulator to generate a fixed-frequency sine wave. The phase accumulator steps quickly through the sine look-up table for the larger phase increment and thus generate a high frequency sine wave while the phase accumulator takes many more steps, accordingly generating a slower waveform for the small phase increment. The final output frequency of DDS system can be tuned only by varying the reference clock frequency or by reprogramming the PROM. The spectral purity of the final analog output signal is determined primarily by the DAC and the phase noise basically depends on the reference clock.

Repetition-rate control was implemented by a system based on direct digital synthesis (DDS) which, unlike methods based on phase-locked loops, adds no extra phase noise over and above that which is present in the original reference frequency [36]. The first implementation was demonstrated by Bartels et al. [37] for asynchronous optical sampling in pump-probe spectroscopy. Two identical DDS boards (Analog Devices, AD9912) were operated with a 48-bit tuning word, permitting a practically arbitrary choice of the output frequency (tuning step size ~4 μHz), and with a maximum clock frequency of 1 GHz (Fig. 3.17) [38].

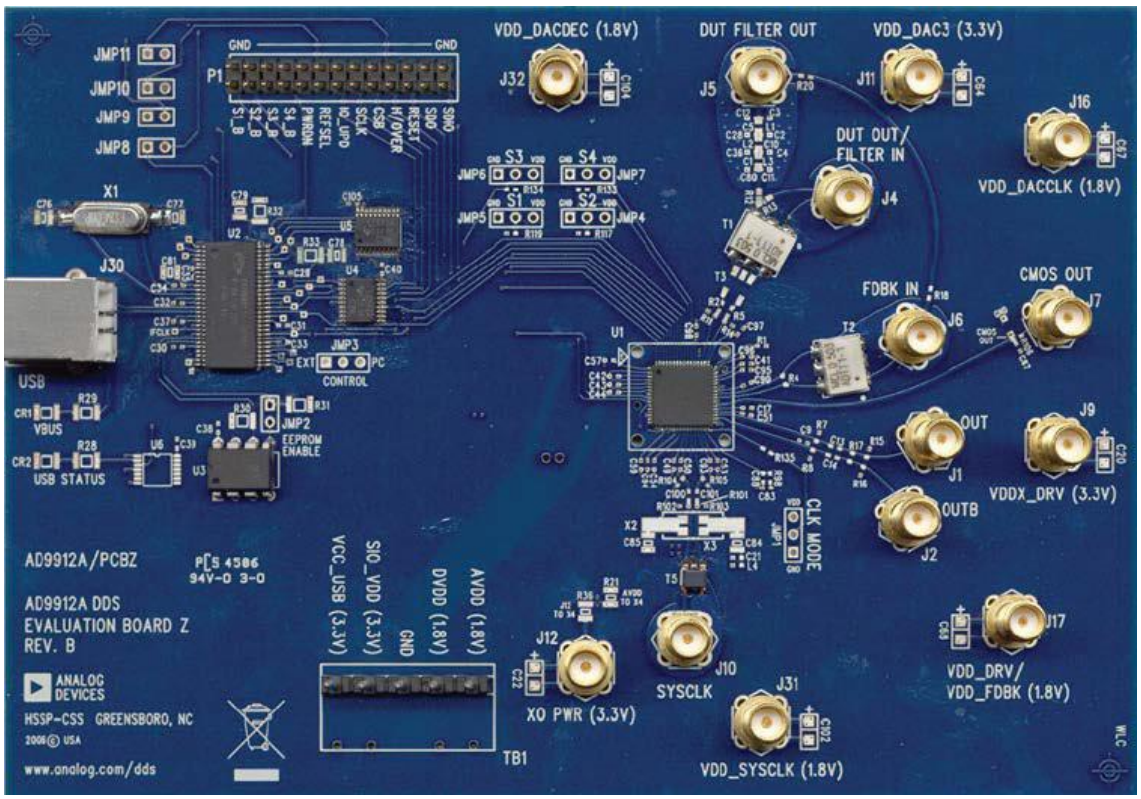

Figure 3.17: Direct digital synthesizer evolution board (Rev. B). Connections of DDS board are arranged as followed in [39].

A precision radio-frequency synthesizer provided a 1-GHz reference frequency for the system, which is illustrated in Fig. 3.18. This master synthesizer had two functions. First, it provided a direct reference for the repetition frequency (f_{REP}) of one of the Yb:fibre lasers, referred to hereafter as the *master laser*. The tenth harmonic of the master laser was sampled using a fast silicon photodiode and a 1-GHz bandpass filter (1 GHz ± 50 MHz). These detected signals were used to phase-coherently generate an error signal corresponding deviations of the repetition rate-offset Δf from the set value of Δf_{set}. This error signal generated by two DDS boards are described in Figure 3.15. This unit combined two direct digital synthesizers and selected the 10th harmonics of the repetition rates of the master $10 \times f$ and slave lasers $10 \times (f + \Delta f)$ with bandpass filters BP1 and BP2 (1 GHz centre frequency, 50 MHz bandwidth) and added those signals to the outputs of two DDS evolution board using double balanced mixers M1 and M2. The amplified error signal was low-pass filtered with a loop filter and further amplified by using a high voltage amplifier (HVA) to control the slave repetition frequency via the output collimator mounted on a high-bandwidth piezoelectric transducer as explained in the previous section.

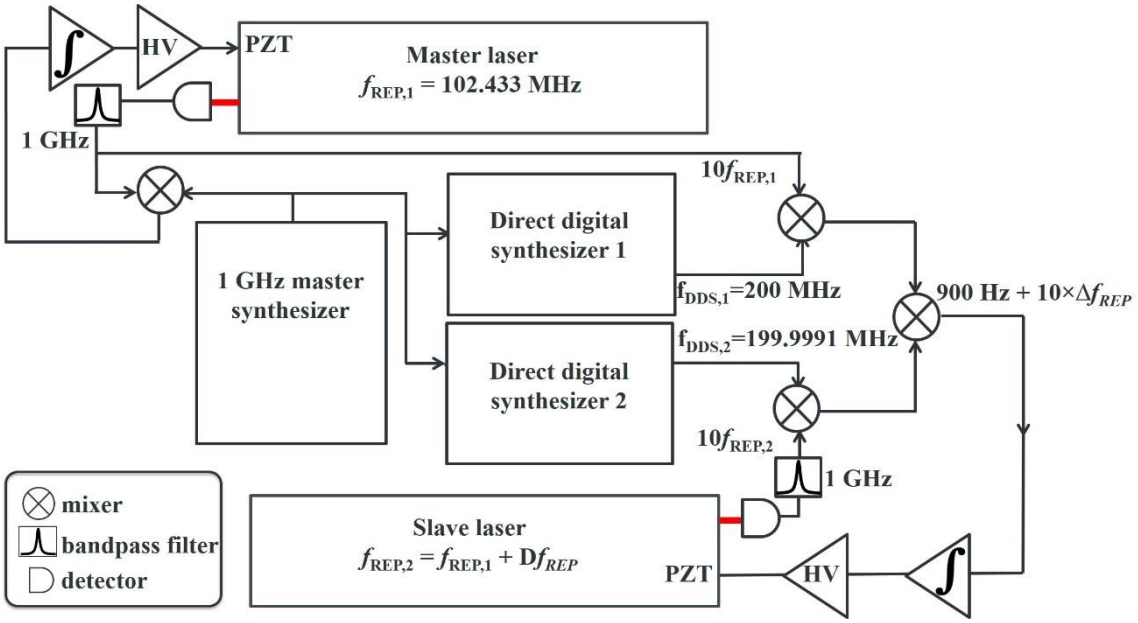

Figure 3.18: Repetition-frequency locking scheme. HV, high voltage amplifier; PZT, piezo-electric transducer.

The second function of the master synthesizer was as the clock for two DDS modules, whose purpose was to provide the second fibre laser (the *slave laser*) with a reference frequency, enabling its repetition rate to be locked at a fixed offset from that of the master laser. Taking as an example, the arrangement needed to lock the repetition-frequency difference (Δf_{REP}) to 90 Hz, each DDS was programmed with a different tuning word, resulting in two ~200-MHz outputs with a frequency separation of 900 Hz. These outputs were separately mixed with the tenth harmonics of the master and slave repetition frequencies, and the difference of the resulting frequencies (900 Hz + $10\Delta f_{REP}$) used as the error signal sent to to a proportional-integral (PI) amplifier (New Focus, LB1005) for driving the intracavity PZT in the slave laser.

The PI amplifier shown in Fig. 3.19 was calibrated before the phase-lock loop (PLL) was activated for the repetition frequency stabilization. Firstly, the output voltage (6) was monitored with no input (1) by turning the output offset control (9) to set the minimum voltage to 0 V. Similarly, the output voltage was also arranged for its maximum setting to set to 10 V. These voltage rail settings provided sufficient drive to capture and lock the repetition frequency, but also to avoid the possible damage of the PZT if it was driven with negative voltage. Then the error signal was connected to (1) and the input offset (2) was adjusted to zero offset. The acquire switch (5) was kept in low-frequency gain limit to limit DC gain and exclude integral gain domination at lower frequencies. While monitoring the bandwidth of the output of PI amplifier (6), the locking stability was improved by increasing the proportional gain (4) and the corner frequency (8) until reducing oscillation on the output (6). The output of PI amplifier was passed to the HVA and the formatted PLL signal was

monitored in the error monitor output (7). Once the error signal was set to 0 V by adjusting the output offset (9), the acquire switch was set to Lock On for longer locking stabilization.

Figure 3.19: Control panel of PI amplifier (New Focus LB1005). 1, input port; 2, input offset control; 3, PI corner frequency control; 4, proportional gain control; 5, gain regime control; 6, output port; 7, error port 8, low frequency gain control; 8, output offset control.

The DDS technique enables excellent long-term stability. In Fig. 3.20 I present time-series data of the repetition-frequency difference measured from the two lasers locked as described in the scheme above. Over a total observation time of 100 seconds the average frequency was counted in windows of 100 ms and implied an RMS variance of only 2 mHz.

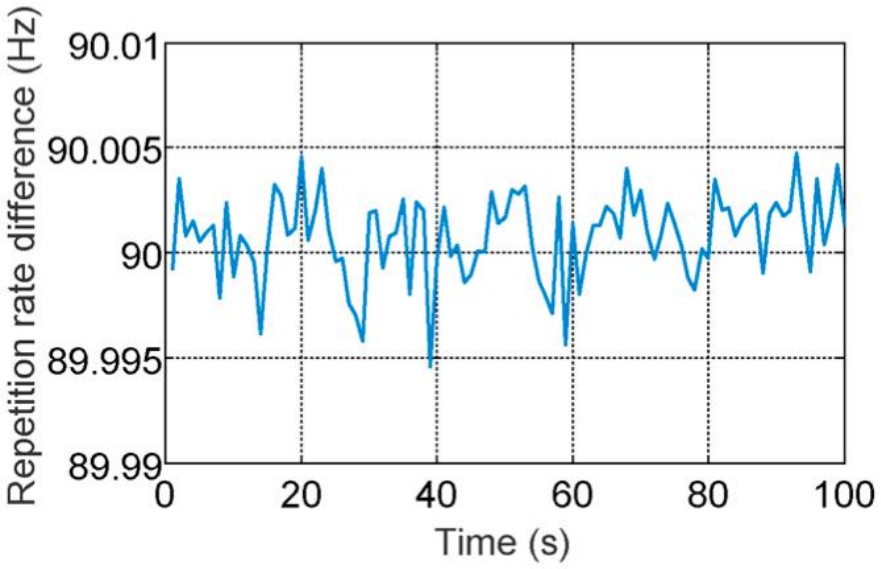

Figure 3.20: Variation of the locked repetition rate difference (Δf_{REP} = 90 Hz) over a period of 100 seconds with 100 ms gate time, showing a RMS variance of only 2 mHz.

3.4 Nonlinear interferometer: carrier-phase-envelope stabilization

Yb:fibre oscillator mode-locking in the normal dispersion regime has remarkable capabilities to maintain stability for long periods and generate chirped picosecond pulses

with passive mode-locking, which can be dechirped to sub-150 fs outside the laser. Such advantages make ANDi Yb:fibre lasers promising for high power optical frequency combs in precision spectroscopy applications by exploiting coherent supercontinuum generation [40].

In their role as pump sources for the mid-infrared dual-comb spectroscopy with OPOs, the Yb:fibre lasers are used to provide a phase reference, which by means of nonlinear interferometry allows the detection of idler carrier-envelope offset frequency in the optical parametric oscillators. Specifically, an external sum-frequency mixing (SFM) setup was used to mix the pump and idler pulses to produce light to heterodyne with the pump supercontinuum. As reported in [41], the heterodyne signal between pump supercontinuum and the pump-idler SFM light yields the idler CEO frequency.

3.4.1 *Pulse compression*

The naturally chirped pulses produced by the ANDi lasers must be compressed to their transform-limited durations to generate a broad supercontinuum. There are a number of techniques known for temporally compressing optical chirped pulses [42-48]. The most common method is the grating based pulse compression in the picosecond or femtosecond regime. When chirped pulses are sent through the compressor (such as a pair of diffraction gratings or transmission gratings etc.), the spectral phase of chirped pulses is flattened in terms of its chromatic dispersion. The shortest pulse duration is then limited by the optical bandwidth of the pulses, defined as the bandwidth-limited pulse duration.

The grating can be classified by its design properties such as reflection or transmission [49]. Reflection gratings diffract light back into the plane of incidence. However, the transmission gratings diffract the light into the opposite half-space. Commercially the transmission gratings have better performance for pulse compression in comparison to reflection gratings. Here, grating properties will be explained for transmission gratings and a pair of transmission gratings is described as were used for pulse compression in the experimental setup.

The general grating equation that governs dispersion and diffraction terms is given by

$$m\lambda = d(\sin\theta_i + \sin\theta_D) \tag{3.2}$$

where m is the diffraction order, λ is the incident wavelength, d is the grating period, θ_i is the diffraction angle of the incident light in the m^{th} diffraction order, and θ_D is the diffraction angle of dispersed light in the m^{th} diffraction order. The experimental setup is shown in Fig. 3.21.

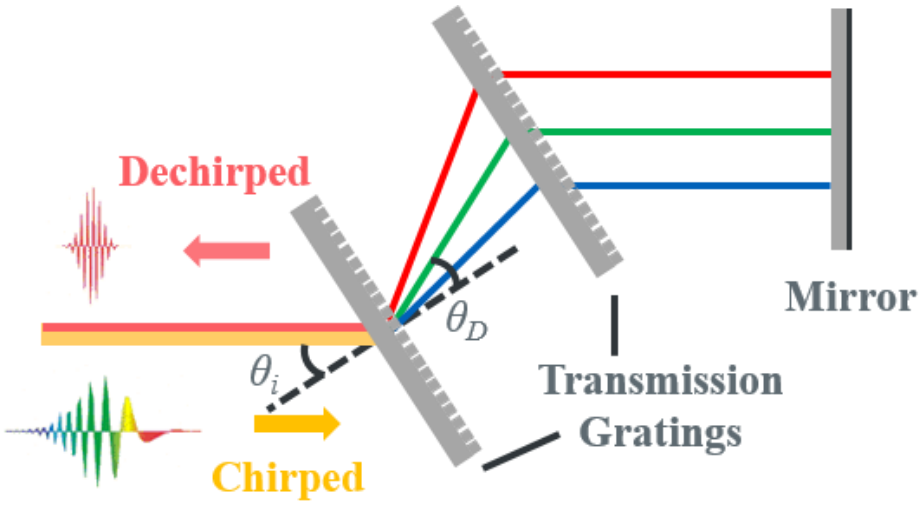

Figure 3.21: Pulse compression setup with a transmission grating pair.

The angular dispersion of the first transmission grating is given by

$$\frac{d\theta_D}{d\lambda} = \frac{\sin(\theta_i) - \sin(\theta_D)}{\lambda.\cos(\theta_D)} \tag{3.3}$$

The angular dispersion yields negative group delay dispersion (GDD) and the angular dispersion equation is modified due to GDD relation as:

$$\frac{d^2\varphi}{d\omega^2} \approx -\frac{\lambda_i^3}{2\pi c^2 d^2}\frac{L_{sep}}{cos^2(\beta')} \tag{3.4}$$

where L_{sep} is the distance between transmission gratings and β' is the difference of diffraction angle and incident angle. In transmission gratings, β' becomes less critical for pulse compression.

The pulse compression setup followed the transmission grating based pulse compression as explained here. Firstly, the amplified chirped beam was divided into two arms with a beam splitter which reflected 25% of incident beam and transmited the rest of total power to the optical parametric oscillator directly. The reserved 25% of the incident power corresponded to 344 mW and propagated through the compressor (Figure 3.22). Before compression, the pulses from the Yb:fibre lasers were typically around 3.9 ps in duration. To compress the chirped pulses from each laser a pair of transmission gratings (Lightsmyth, T-1000-1040) was employed. Each transmission grating had 1000 lines/mm with exceptionally high transmission efficiency of more than 93%. Group velocity dispersion (GVD) was calculated as -7038 fs^2/mm from using the line density of grating pair. By adjusting the distance between the gratings, the pulse was compressed to its minimum value. Diffraction limited pulses were observed by setting the grating pair separation distance to 32 mm corresponding to 0.24 ps^2 GVD at a CPA power of less than 1.5 W.

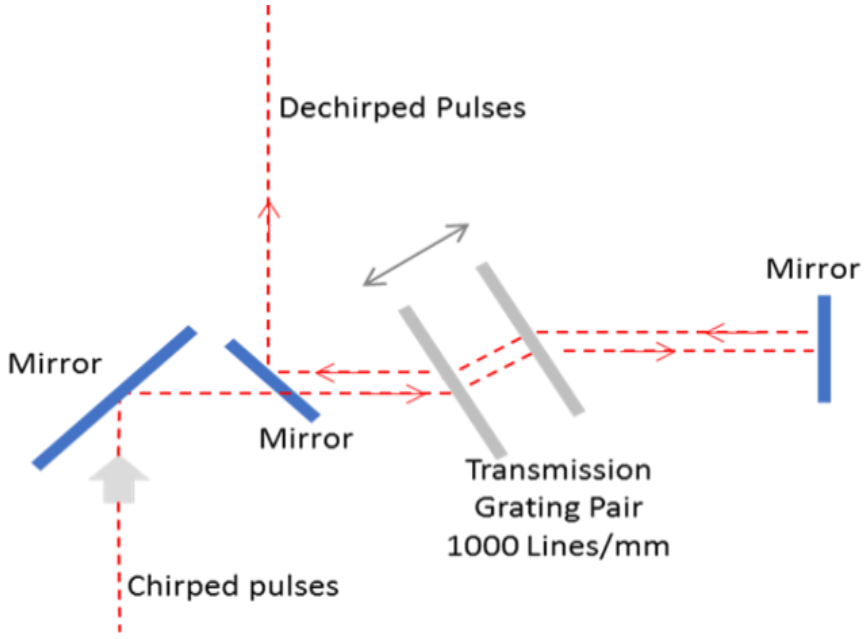

Figure 3.22: Compressor setup involving double-pass transmission through a grating pair.

The pulse durations leaving the compressor output were measured with an interferometric autocorrelation (IAC) technique based on two-photon absorption (TPA) using a GaAsP photodiode [50]. Firstly, the pulse spectrum was measured with the optical spectrum analyser and its inverse FFT was taken to find the transform-limited shape of the pulses, following which their IAC was numerically calculated and compared with the experimentally measured IAC. The interferometric autocorrelation of the compressed pulses is depicted in Fig. 3.23, and has a FWHM of 172 fs. The shaped of the IAC

indicates that the output pulses are essentially and completely dechirped and so had been compressed to close to their transform limit. The average power after the compressor setup was 263 mW giving a pulse peak power of 13.7 kW and a pulse energy of 2.5 nJ.

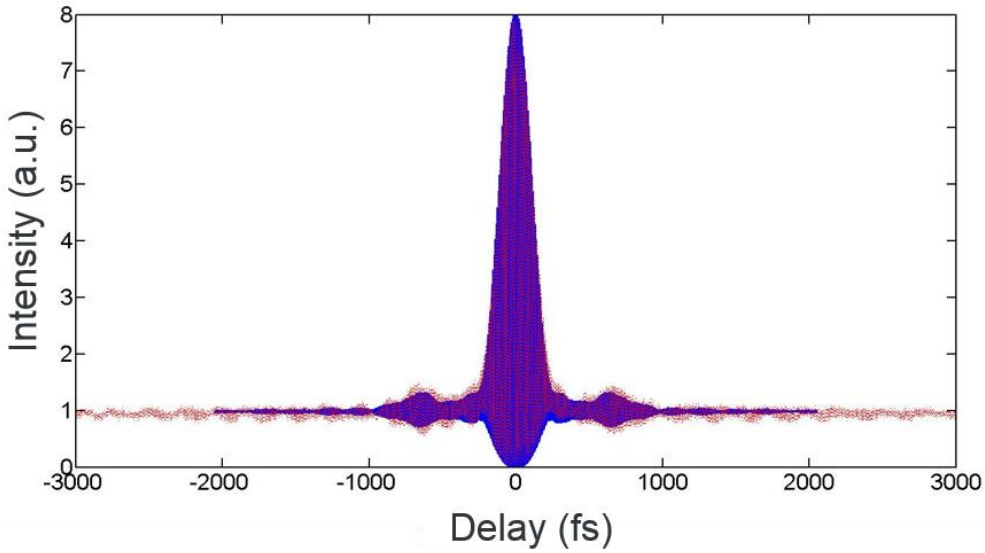

Figure 3.23: Autocorrelation trace of compressed pulse obtained by two-photon-absorption autocorrelator. Dechirped pulses (blue) after compressor were observed at a pulse duration of 172 fs as agreed with its bandwidth-limit (red).

3.4.2 *Pump supercontinuum generation*

Supercontinuum generation is necessary to broaden the input spectrum to a wide optical spectrum around the input light. Although the temporal coherence is not necessarily preserved, the spatial coherence basically remains high. A typical supercontinuum generation spans an octave in frequency (a factor of two in some frequency components of the continuum optical spectrum). To achieve this phenomenon, optical pulses propagate in a strongly nonlinear device (such as using a tapered fibre, photonic crystal fibre or waveguide) [51-53]. Since the development of commercially available photonic crystal fibres (PCF), supercontinuum generation has been fundamental to many accomplishments in optical frequency technology in many applications.

The physical process of supercontinuum generation in PCF predominantly relies on self-phase modulation (SPM) and four-wave mixing (FWM). Once the pump light starts to propagate through a highly nonlinear fibre, the phase of the input light is introduced to an intensity dependent shift in terms of SPM. Then FWM becomes dominant after the initial SPM based broadening through the PCF. The supercontinuum generation using initial pulses, $A(z,t)$ is evolved with the generalized nonlinear Schrodinger equation

(GNLE) in terms of chromatic dispersion, the Kerr nonlinearity with self-steepening, and Raman scattering [54] given by

$$\frac{\partial A}{\partial z}+\frac{\alpha}{2}A-\sum_{k\geq 2}\frac{i^{k+1}}{k!}\beta_k\frac{\partial^k A}{\partial T^k} = i\gamma\left(1+i\tau_{shock}\frac{d}{dT}\right)\left(A(z,t)\int_{-\infty}^{+\infty}R(T')\times|A(z,T-T')|^2dT' + i\Gamma_R(z,T)\right) \quad (3.5)$$

Eq. 3.5 shows linear propagation effects including linear loss, α and dispersion coefficients of propagation constant, β_k in its left-hand side. In the right-hand side of Eq. 3.5 is contained nonlinear effects based on the general nonlinear coefficient, $\gamma = w_0 n_2(w_0)/cA_{eff}(w_0)$ where $n_2(w_0)$ is the nonlinear refractive index and $A_{eff}(w_0)$ is the effective mode area of the propagation medium. Dispersion of nonlinearity associated with self-steepening and optical shock formation is defined inside the first parenthesis. Last contribution on nonlinear dynamics is linked to Raman scattering including the spontaneous Raman noise, Γ_R. The process of supercontinuum is activated when a certain threshold power is reached. For sufficient spectral broadening, such parameters should be arranged carefully.

The compressor served as a source of high-peak-power fs pulses for the generation of an octave-spanning supercontinuum, which was purposed to implement *f*- 2*f* self-referencing for carrier-envelope offset stabilization [55]. Despite a coherent octave-spanning supercontinua at Ti:Sapphire wavelength of 800 nm, the longer lengths of PCF and/or laser sources with higher average powers are required in terms of the longer pulses produced by ANDi Yb lasers. Therefore the first-order solitons are not strong to undergo generation in the PCF of multiple Raman solitons, which can reduce the coherence across the supercontinuum spectrum [54].

In order to investigate estimated length of the PCF, the pump supercontinuum was simulated using Eq. 3.5, the PCF parameters (numerical aperture, the fibre GDD etc) and the pump parameters (pulse duration, input power etc) (Fig 3.24). The pump parameters

were used for the dechirped pulses which were compressed to 172 fs and the input power of 260 mW. For the PCF, the parameters of NKT Photonics; SC-3.7-975 was followed and simulated up to 200 cm with 1-cm step. Femtosecond pulse launched into PCF activated soliton fissions and then excess energy was transferred to dispersive waves through shorter wavelengths while fundamental solitons yielded raman scattering to shift through longer wavelengths. With current input parameters, both effects symmetrically initiated the spectral broadening within first 9 cm. Then red shift became strong in longer wavelengths rapidly. In propagation distance between 50 cm and 100 cm spectral components of the pump supercontinuum occured resonably on both shorter and longer wavelengths under certain circumstances. After first 100 cm, spectral broadening for shorter wavelengths seems quite stable. To consider simulation result with input parameters, the length of PCF between 80 cm and 100 cm is enough to generate conjugate of $p + i$ (approximately 800 nm) with sufficient power.

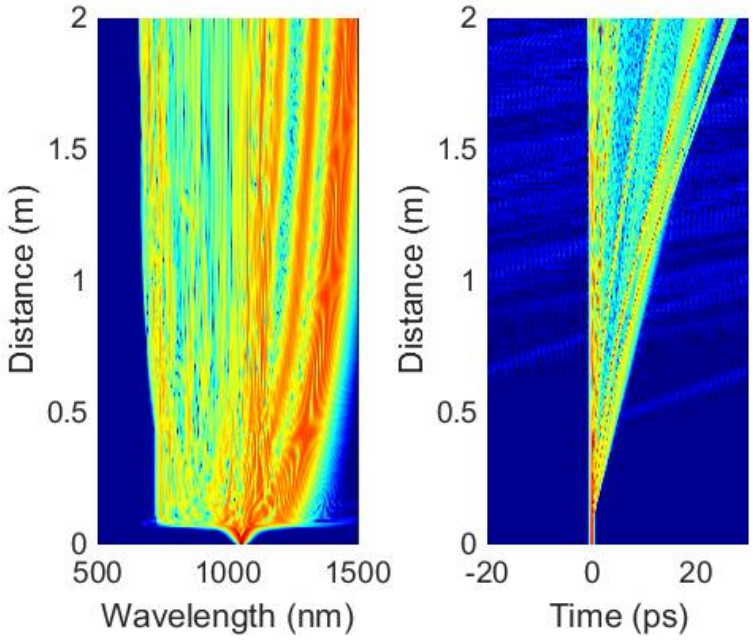

Figure 3.24: The pump supercontinuum generation is simulated to evaluate spectrum (left) and temporal (right) characteristic after propagating 2m.

The suitability of the Yb:fibre laser is assessed for super-continuum generation by using a commercial PCF (NKT Photonics; SC-3.7-975) specifically designed for pumping by a 1050 nm ultrafast laser. The PCF core had a diameter of 3.7 µm a numerical aperture (NA) of 0.25 and a nonlinear coefficient of ~18 $(W.km)^{-1}$. Two identical 102-cm-length of the PCF at the zero-dispersion-wavelength (ZDW) of 975 ± 15 nm were used in the both channels. The pulses after the compressors were attenuated in order to obtain the necessary wavelength for heterodyning with the sum frequency mixing light and then

coupled into the PCF with an efficiency of 63%, based on the input and output average powers of ~261 mW and 165 mW, respectively. The super-continuum spectra from both channels are shown in Fig. 3.25. Strong Raman-soliton pulses are apparent on the long-wavelength side (λ~1225 nm). Dispersive waves on the short-wavelength side of the supercontinuum (λ < 900 nm) were generated with significant spectral intensities down to wavelengths just below 800 nm.

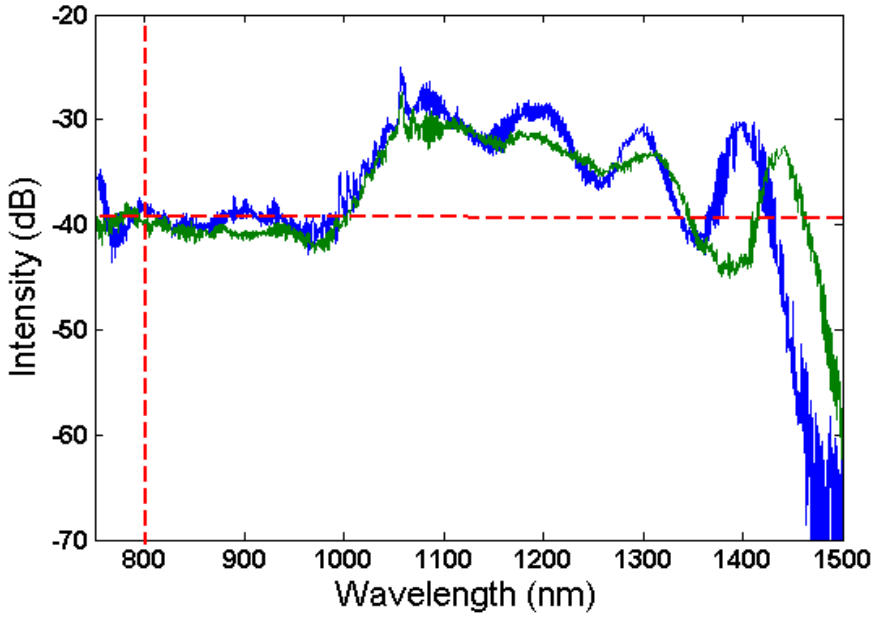

Figure 3.25: Supercontinuum spectra of pump 1 (blue) and pump 2 (green). Dashed lines intersect at 801 nm corresponds to pump + idler in order to detect carrier offset frequency. Vertical dashed lines center on the required wavelength for f_{CEO} detection and typical power of the required wavelength (cross-section of vertical and horizontal dashed lines) is less than 1 mW.

Each PCF output was connected to a separate 3-axis microblock and then each pSC beam was collimated by a 6-mm aspheric lens on microblock. The pSC beam spot sizes were collimated before sending them through the beat detection part.

3.4.3 *Sum frequency mixing*

Sum frequency generation is a nonlinear process based on $\chi^{(2)}$ nonlinearity that is also similar to parametric oscillation described in Section 2.2.1. This physical phenomenon also requires different phasematching for sum and difference frequency generation [57]. Basically two input photons at different frequencies of ω_1 and ω_2 propagate without change at their respective group velocities in the nonlinear crystal. Then one photon at a frequency of ω_3 is generated in a case of momentum cconservation:

$$\omega_3 \approx \omega_1 + \omega_2 \tag{3.6}$$

The efficient nonlinear conversion is valid when both input photons have the same flux and polarization. Second-harmonic generation is treated as a special case of sum frequency generation as well.

For obtaining the carrier-offset frequency of the idler pulses, the frequency mixing of pump and idler is configured to generate the required wavelength to beat the conjugate one generated from the pump supercontinuum. The spatially overlapped idler and unconverted pump beams exiting the OPO second curved mirror were focused by a concave silver mirror into a 2-mm-long PPLN crystal with a grating period of 22 μm which phasematched pump + idler (*p* + *i*) SFM generation (Fig. 3.26). The beam was then collimated by another concave silver mirror. A dichroic mirror was used to separate the idler from the SFM light at ~801 nm.

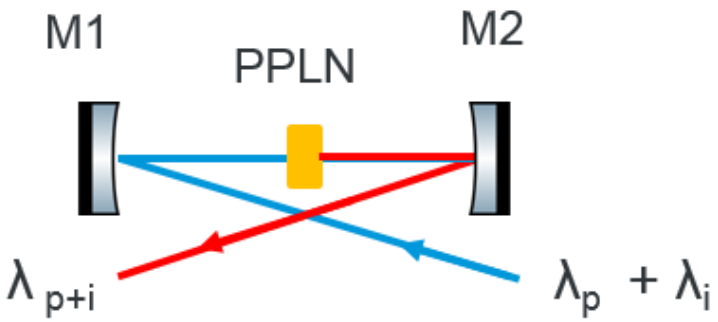

Figure 3.26: Schematic of sum-frequency generation with 2 mm PPLN crystal for pump + idler generation. M1, M2; curve mirror.

The output of the PPLN crystal also contains a few different spectral components generated by interactions between pump, idler and signal as seen Fig. 3.27. An interference filter with a 10-nm FWHM bandwidth was used to suppress all outputs except for the pump + idler light. The generated pump + idler light in each channel was measured to have an average power of 0.9 mW and a spectral bandwidth of 8 nm after interference filter.

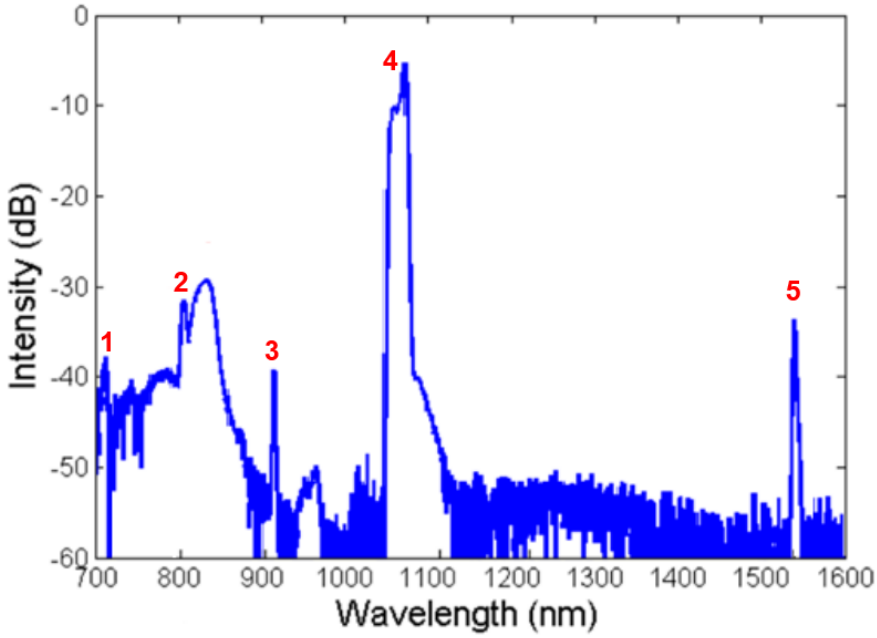

Figure 3.27: Spectrum after frequency mixing with PPLN crystal. The main peak, the remaining depleted pump, contains a big portion of power. (1) 2nd harmonics of signal; (2) pump + idler SFM, λ_{p+i}; (3) $2p + i$ different frequency generation λ_{2s+i}; (4) pump λ_p, (5) signal λ_s

3.5 Carrier envelope offset frequency control

A pulse of the modelocked laser can be alternatively defined as a time-dependent electric field formed of a slowly varying envelope and a faster underlying carrier wave. Although many areas of optics ignore the carrier-envelope phase, it must be considered for frequency domain applications such as spectroscopic measurements or absolute frequency measurements.

To control the CEO frequency of an oscillator it is first necessary to detect it by a nonlinear interferometric measurement [55]. By definition the carrier-envelope offset phase arises from a difference between the intracavity group and phase velocities. Therefore, modulation of the intracavity dispersion allows control of this CEO phase. The principle behind self-referencing from nonlinear interferometry was explained in Chapter 2. Here, control of the CEO frequency for each OPO will be examined and their limitations and performances will be examined together.

3.5.1 *CEO detection*

The carrier-envelope offset frequency detection is required for the idler offset frequency which is necessary for the mid-infrared spectroscopy described later. The $p + i$ light generated by the sum frequency mixing and its conjugate from supercontinuum

generation is superimposed on a photodetector measuring the optical intensity. Then a beat signal occurs with the difference of these optical frequencies.

Before observing the beat signal, some conditions must be satisfied to record the optical frequency difference on a photodetector. First there must be perfect overlapping of the spatial distributions of the input light fields. Second, polarization states of the input lights must not be orthogonal. Their polarization states should be parallel even for higher difference generation. The third condition is to use a suitable photodetector whose frequency and spectral bandwidths cover the optical frequency difference. The last condition is temporally overlapping of both input pulses, meaning that the time delay between the input pulses must be zero.

All conditions required to detect a beat note were investigated before looking for it. For spatially overlapping between the filtered pSC and $p+i$ by SFG, the beam profiler was used to properly match their spot sizes on both photodetector. Both overlapped beams were observed in almost same beam shape and sizes shown in Fig. 3.28.

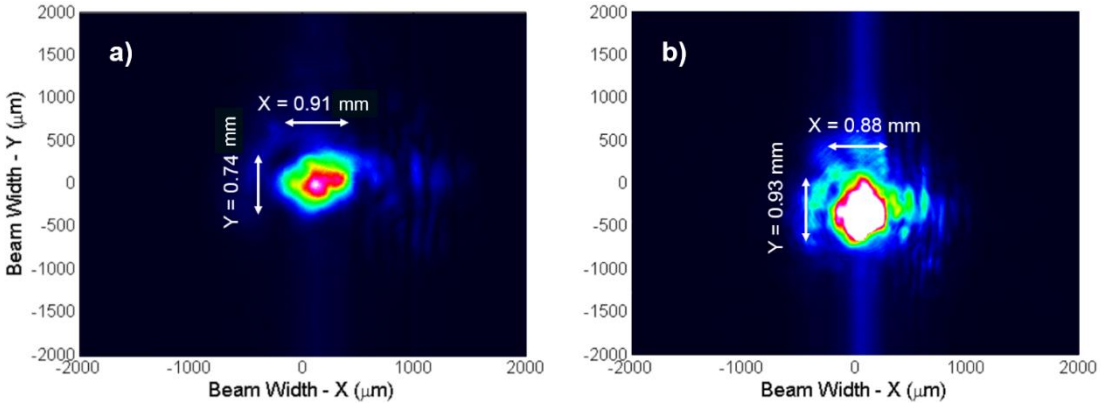

Figure 3.28: The beam profiles of the combined beams between pump supercontinuum and pump+idler SFM light for OPO comb 1 (a) and OPO comb 2 (b).

The optical heterodyne detection setup was assembled as shown in Fig. 3.29. The $p + i$ SFM light was combined with the pump supercontinuum (*pSC*) in the beamsplitter before detection by an avalanche photodiode (APD, Hamamatsu C12702-03) which had peak sensitivity at visible wavelengths and a high-band cut-off frequency of 100 MHz. Once both input beams were overlapped spatially, temporal overlapping was concerned before detection. The temporal mismatch between input pulses arose due to different lengths between the nonlinear interferometer's arms. These differences for comb 1 and comb 2

were measured 713 mm and 761 mm respectively. For each comb interferometer, the time delay setup seen Fig. 3.26 was implemented to compensate temporally pulse pair from the interferometer. The overlapped beam was focussed onto an APD detector with a 50-mm-long lens after the polarizer and interference filter. Each APD detector was aligned by observing the highest fundamental repetition frequency on a RF spectrum analyzer. By adjusting the time delay between the $p + i$ and pSC arms, a beat signal was detected containing the idler CEO frequency directly.

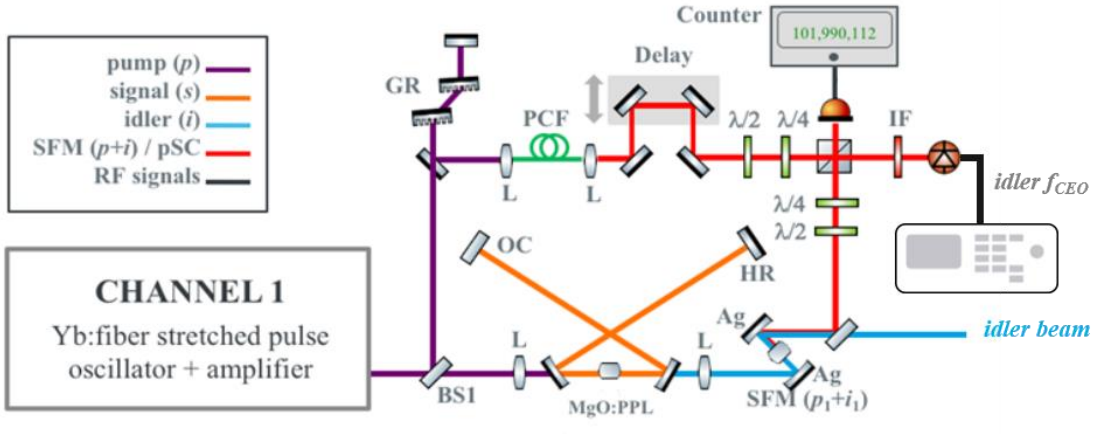

Figure 3.29: The nonlinear interferometer is used to detect idler f_{CEO} for stabilization. GR, grating; L, lens; PCF, photonic crystal fibre; IF, interference filter; HR, high reflected mirror; OC, output coupler; BS, beam splitter.

From the output from each APD the RF signals was measured at f_{rep} and $f_{rep} \pm f_{CEO}$ (Fig. 3.30). The absolute power of the CEO signal was typically less than -30 dBm and so required amplification; a minimum of -20 dBm signal strength was necessary for locking. So, each beat signal was firstly filtered with 50-MHz low-pass filter (Mini-circuits) to separate only the CEO signal and prevent damaging amplifier with strong f_{rep} signal. A low-noise amplifier (Mini-circuit ZFL-500LN+) was used to amplify each beat signal with 25-dB gain. Thus the signal-to-noise (SNR) level for each signal was approximately increased up to -10 dB.

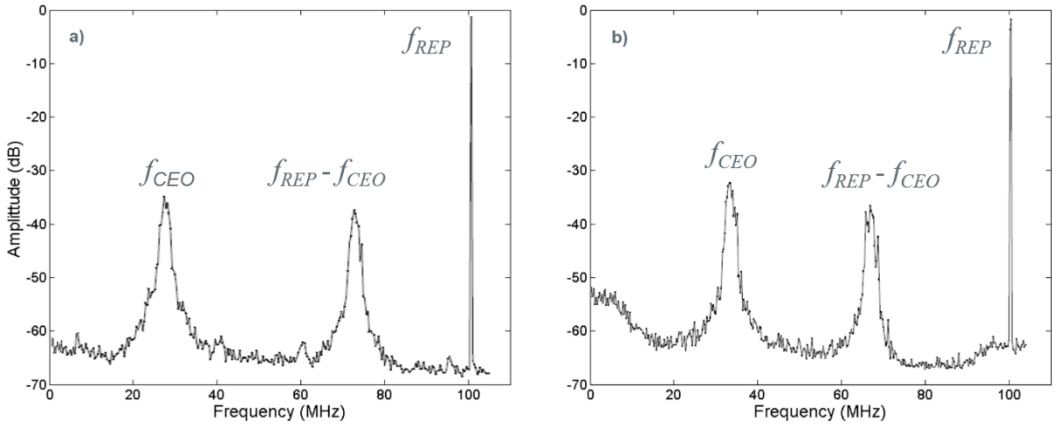

Figure 3.30: The raw RF signal of f_{CEO}, f_{REP} - f_{CEO} and f_{REP} for OPO 1 (a) and OPO 2 (b). The relative intensity of each idler f_{CEO} is observed in almost same level and measured 32 dB.

3.5.2 *CEO stabilization*

Once the f_{CEO} of the laser oscillator had been detected, the detected beat frequency was converted into an error signal in order to stabilize the comb modes by a number of electronics stages. Comparison with an RF reference signal gave an error signal which was used to modulate the position of a cavity mirror through the use of a piezoelectric transducer (PZT). The end mirror was slightly tilted compared to the end mirror angular aperture and therefore kept to the microradian range in order to prevent intracavity power fluctuations.

The detection concepts of each CEO signal have been already discussed in the previous section. The phase-lock-loop electronics for stabilizing both OPOs are substantial and are described here. The general outline of the electronic feedback loop is shown in Figure 3.31.

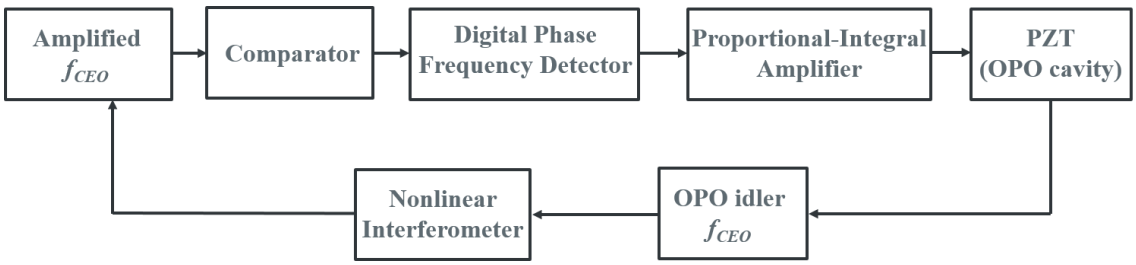

Figure 3.31: The generic sketch of the phase-locked loop for f_{CEO} stabilization.

The amplified RF signal was sent through a comparator (Pulse Research Lab, PRL-350TTL) to generate a low-noise TTL signal. The comparator supplied output voltage of either 0 or 2.7 V. The TTL CEO signal was connected to a digital phase-frequency

detector with a formatted reference signal to generate an error signal for CEO frequency locking.

A digital phase-frequency detector (PFD) was used to compare two TTL input signals and provide the phase/frequency difference between them as shown in Fig. 3.32 [58]. The first input is the modified CEO frequency signal, while the second input is the reference signal from a RF signal generator (Hewlett Packard ESG-D3000A RF Synthesizer) to which the CEO frequency is to be stabilized.

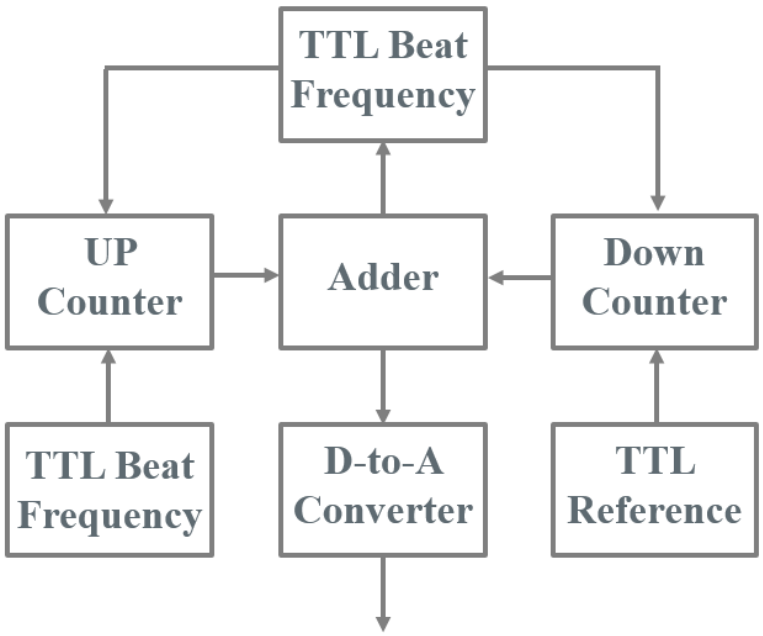

Figure 3.32: Block diagram of the digital phase-frequency detection used to convert an analog signal for proportional-integral (PI) amplifier. Adapted from [58]

The block diagram of the PFD is based on [58]. The TTL beat frequency is divided down in 4-bit synchronous up counter, while the TTL reference frequency is divided down in 4-bit synchronous down counter. Then both inputs are added together by a 4-bit adder. If the TTL beat frequency becomes slightly faster (slower) than the reference frequency the up counter counts faster (slower) than the down counter. Eventually, the output of adder is slowly incrementing (decrementing). When the beat frequency and the reference frequency are same with different phases, output of the adder is constant and responds to the phase difference between these frequencies. As a final step, the D-to-A module converts the phase difference to an analog signal for the PI amplifier.

The analogue signal from the PFD was passed to a proportional-integral (PI) amplifier to form a phase-locked-loop. To employ a PZT stack in the OPO cavity the stack was normally driven directly by the PI amplifier. Correct adjustment of the PI amplifier followed the same arrangement as explained in Section 3.3.2.

The cavity length tuning behaviour of the OPO was described in Chapter 2. The same derivation is executed for the CEO phase of the OPO. By the definition of the absolute phase of an OPO pulse, the CEO phase is given by

$$\emptyset_{ceo} = \emptyset(\omega) - \omega\frac{d\emptyset(\omega)}{d\omega} \tag{3.7}$$

The variation in CEO phase with frequency is therefore given by

$$\frac{d\emptyset_{ceo}}{d\omega} = -\omega\frac{d^2\emptyset}{d\omega^2} \tag{3.8}$$

which can be correlated with group delay dispersion by cavity tuning expressed [59]

$$\frac{\partial\tau}{\partial\omega} = \frac{d^2\emptyset}{d\omega^2} = -\frac{1}{c}\frac{dL}{d\omega} \tag{3.9}$$

where τ is the cavity round trip time or group delay differentiated to find group delay dispersion. By using Eq. 3.9, CEO is linked by

$$\frac{d\emptyset_{ceo}}{d\omega} = \frac{\omega}{c}\frac{dL}{d\omega} = k\frac{dL}{d\omega} \tag{3.10}$$

This equation can be rearranged to provide

$$\frac{d\emptyset_{ceo}}{d\omega} = \frac{\frac{\omega}{c}}{\frac{d\omega}{dL}} \tag{3.11}$$

which in turn can be modified to show that

$$\frac{d\emptyset_{ceo}}{dL} = \frac{2\pi}{\lambda} \tag{3.12}$$

According to Eq. 3.11, the cavity tuning allows the carrier-envelope offset phase to be controlled by the cavity length tuning slightly without affecting the centre frequency of the resonant pulse. This equation also shows that a cavity round-trip change of λ will provide a CEO frequency change of f_{REP}.

The pump f_{CEO} equals the sum of the CEO frequencies of the signal and idler [Eq. 2.33]; therefore, the idler f_{CEO} can be tuned by changing the pump f_{CEO} of the same channel by changing the drive current of the appropriate laser diode in the mode-locked Yb:fibre oscillator. Instead, the idler f_{CEO} can be tuned by changing the OPO cavity length. A 50 MHz shift was achieved by moving the folding mirror by 400 nm with a PZT (Thorlabs, AE0203D04F) and the idler f_{CEO} of each channel was therefore independently controlled by using these either of two mechanisms.

3.5.3 *Performance analysis of CEO stabilization*

The OPO and laser output have intensity fluctuations as a function of time that are known as the relative intensity noise (RIN) [60]. These fluctuations occur beacuse of a number of reasons including thermal instability, mechanical vibrations, beam pointing, or/and electrical noise.

Such noise can be investigated by the noise power per unit frequency interval relative to the mean signal. The total power of the system output is expressed by the Parseval theorem which states that the energy of a signal described in time domain is equal to its energy in frequency domain:

$$E_{Total} = \int_{-\infty}^{\infty} |h(t)|^2 dt = \int_{-\infty}^{\infty} |H(f)|^2 df \tag{3.13}$$

The power in a frequency interval is modified for the combined power of positive and negative frequencies for $0 \leq f \leq \infty$, written as

$$P_h(f) = |H(f)|^2 + |H(-f)|^2 \tag{3.14}$$

The power spectral density (PSD) is simplified to use the discrete Fourier transform in order to aquire a finite number of points instead. This approach quantifies *N* points to obtain

$$H_k \equiv \sum_{j=0}^{N-1} h_j e^{i2\pi \frac{jn}{N}} \tag{3.15}$$

The PSD is integrated from 0 to Nyquist frequency (f_N) and normalised with the mean squared amplitude. It corresponds to half the mean squared amplitude and applied to each frequency to obtain the cumulative noise, given by

$$\Delta h_{CUM} = \left(2\int_0^{f_N} P_h(f)df\right)^{1/2} \tag{3.16}$$

Where $P_h(f)$ is the normalised PSD. During the performance analysis of f_{CEO} stabilization, the noise of the stabilized and free-running systems are evaluated in terms of their relative intensity noise (RIN) using the PSD which is calculated as as the Fourier transform of the autocorrelation function of the normalized power fluctuations.

The RIN measurements were conducted for each laser and each OPO for the stabilized and free-running system. Before the measurements, both lasers and OPOs were enclosed in perspex cases. The idler outputs from each OPO source were detected on individual mid-infrared detectors and amplified to fill the dynamic range of the data acquisition card before the data were recorded using a 12-bit data acquisition card. The recorded data including a fluctuation around zero were processed using the PSD calculated relative to the mean signal as described above. The PSD was plotted on a dB scale, a standard method of displaying RIN measurements in units of dBc^2/Hz, where c is the carrier voltage [61]. The cumulative standard deviation was calculated as a percentage relative to the carrier.

The RIN for both OPOs was measured using the idler outputs for stabilized and free-running operations and shown in Fig. 3.33. The RIN results of both OPOs was observed to be very similar in terms of the frequency components that contributed to the overall cumulative standard deviation. For both free-funning OPOs, their noise characters were found to be almost the same and each relative intensity noise was dominated by frequencies around 1 kHz. When the idler f_{CEO} of each OPO was locked, each RIN was slightly enhanced to higher than 1 kHz (~2 kHz). However, the servo bumps of PZT that were used to modulate the cavity dispersion were observed at frequencies of ±4 kHz. Due to the servo bumps, the frequency noise of feedback loop was built up in terms of feedback changing from negative to positive or vice versa [62]. Higher frequencies beyond that were expected to arise from acoustic vibrations and thermal drifts across the optical bench and air flows inside the covered OPO cavity.

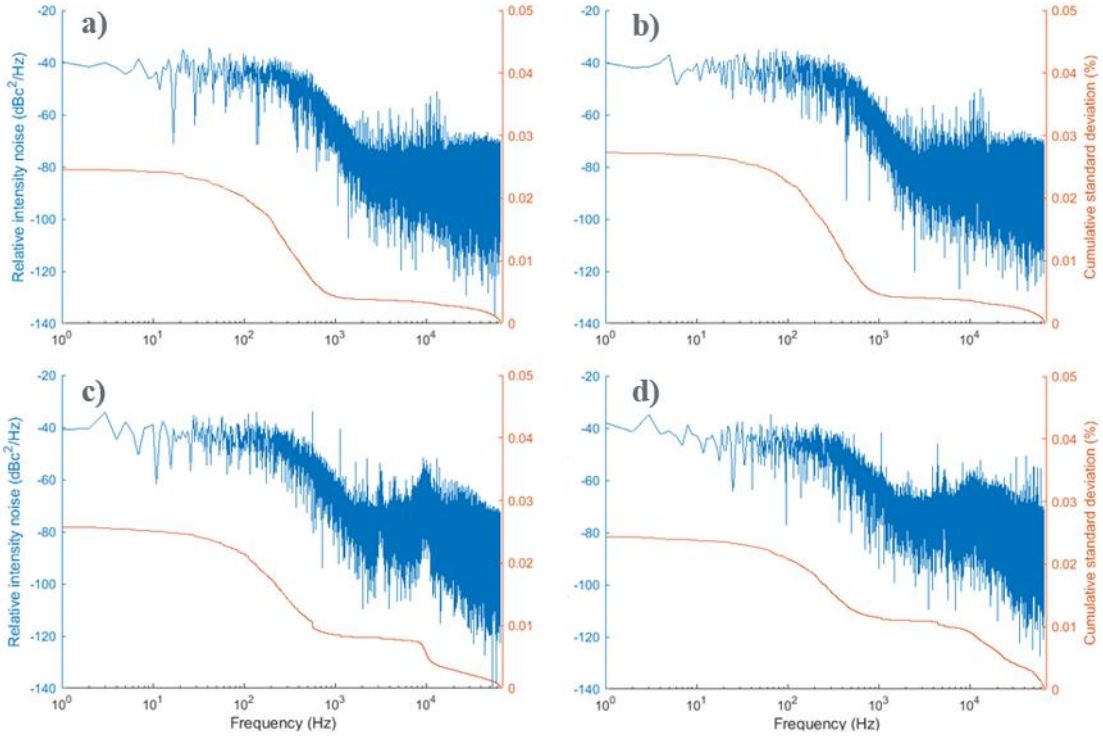

Figure 3.33: The RIN results of free-running OPO 1 (a) and OPO 2 (b). Their free-running noise performances were compared to the f_{CEO} stabilized OPO 1(c) and OPO 2 (d).

Both OPOs were designed with long PPLN crystals providing significant contribution to the net-positive GDD and their idler offset frequencies were stabilized using cavity tuning in terms of Eq. 3.20. Although the OPO with the high group delay dispersion is influenced less by intracavity instabilities, the modulation depth for the phase-locked loop is also limited for this reason. This explains why stabilizing the f_{CEO} of the OPO did not achieve any substantial noise supression. In summary, the noise analysis here shows that the OPO

operated with high cavity dispersion is passively stable and therefore suitable for spectroscopic measurement.

3.6 Conclusion

In this chapter, the development of two independent synchronously-pumped OPOs producing broadband mid-IR pulses with identical spectral properties from two 20-mm-long MgO:PPLN crystals has been described. The design aspects of the OPO comb were introduced and examined in preparation for the initial dual-comb spectroscopy experiments. The high intracavity dispersion of this OPO was designed to make it insensitive to cavity-length variations that means that it is possible to acquire high quality data under standard laboratory conditions without the need for either active repetition-rate stabilization or the carrier offset locking, demonstrating performance equivalent to that obtained using a fully stabilized system.

3.7 References

1. F. Keilmann, C. Gohle, and R. Holzwarth, "Time-domain mid-infrared frequency-comb spectrometer," Opt. Lett. 29, 1542-1544 (2004).
2. A. Schliesser, N. Picqué, and T. W. Hänsch, “Mid-infrared frequency combs”, Nature Photonics, *6*(7), 440-449 (2012).
3. M. J. F. Digonnet, *Rare-Earth-Doped Fiber Lasers and Amplifiers*, 2nd edition., CRC Press, Boca Raton, FL (2001).
4. M.E. Fermann, A. Galvanauskas, G. Sucha, D. Harter, “Fiber-lasers for ultrafast optics”, Appl. Phys. B 65, 259 (1997).
5. L. E. Nelson, D. J. Jones, K. Tamura, H. A. Haus, E. P. Ippen, “Ultrashort-pulse fiber ring lasers”, Appl. Phys. B 65, 277 (1997).
6. N. J. Doran and David Wood, "Nonlinear-optical loop mirror," Opt. Lett. 13, 56-58 (1988)
7. M. E. Fermann, M. L. Stock, M. J. Andrejco, and Y. Silberberg, "Passive mode locking by using nonlinear polarization evolution in a polarization-maintaining erbium-doped fiber," Opt. Lett. 18, 894-896 (1993).
8. Agrawal, Govind P. *Nonlinear fiber optics*. Academic press, (2007).
9. H. A. Haus, “Theory of mode locking with a fast saturable absorber”, J. Appl. Phys. 46 (7), 3049 (1975)
10. Andy Chong, Joel Buckley, Will Renninger, and Frank Wise, "All-normal-dispersion femtosecond fiber laser," Opt. Express 14, 10095-10100 (2006)

11. A. Chong, W. H. Renninger, and F. W. Wise, "Environmentally stable all-normal-dispersion femtosecond fiber laser," Opt. Lett. 33, 1071-1073 (2008)

12. H. M. Pask et al, "Ytterbium-doped silica fiber lasers: versatile sources for the 1-1.2/spl mu/m region." *IEEE Journal of Selected Topics in Quantum Electronics* 1.1 (1995).

13. M. E. Fermann, A. Galvanauskas, and G. Sucha, *Ultrafast lasers: Technology and applications*. Vol. 80. CRC Press, (2002).

14. R. Paschotta, J. Nilsson, A. C. Tropper and D. C. Hanna, "Ytterbium-doped fiber amplifiers," in *IEEE Journal of Quantum Electronics*, vol. 33, no. 7, pp. 1049-1056 (1997).

15. C. M. Caves, "Quantum limits on noise in linear amplifiers." *Physical Review D* 26.8, 1817 (1982).

16. B. M. van Oerle and G. J. Ernst, "Autocorrelation measurements of bursts of picosecond pulses", Appl. Opt. 35 (25), 5177 (1996).

17. L. P. Barry *et al.*, "Autocorrelation of ultrashort pulses at 1.5 μm based on nonlinear response of silicon photodiodes", Electron. Lett. 32 (20), 1922 (1996).

18. E. J. Lim, M. M. Fejer and R. L. Byer, "Second-harmonic generation of green light in periodically poled planar lithium niobate waveguide," in *Electronics Letters*, vol. 25, no. 3, pp. 174-175, 2 (1989).

19. M. Yamada, N. Nada, M. Saitoh, and K. Watanabe, "First-order quasi-phase matched $LiNbO_3$ waveguide periodically poled by applying an external field for efficient blue second-harmonic generation", Appl. Phys. Lett. 62, 435 (1993).

20. Robert G. Batchko, Vladimir Y. Shur, Martin M. Fejer, and Robert L. Byer, "Backswitch poling in lithium niobate for high-fidelity domain patterning and efficient blue light generation", Appl. Phys. Lett. 75, 1673 (1999).

21. L. E. Myers and W. R. Bosenberg, "Periodically poled lithium niobate and quasi-phase-matched optical parametric oscillators," in *IEEE Journal of Quantum Electronics*, vol. 33, no. 10, pp. 1663-1672, (1997).

22. K. Nakamura, J. Kurz, K. Parameswaran, and M. M. Fejer, "Periodic poling of magnesium-oxide-doped lithium niobate," *Journal of applied physics*, *91*(7), 4528-4534, (2002).

23. G. Miller, "Periodically poled lithium niobate: modeling, fabrication, and nonlinear-optical performance", Ph. D. thesis at the University of Stanford (1998).

24. Covesion guide to PPLN, www.covesion.com.

25. L. E. Myers, W. R. Bosenberg, G. D. Miller, R. C. Eckardt, M. M. Fejer, and R. L. Byer, "Quasi-phase-matched 1.064-μm-pumped optical parametric oscillator in bulk periodically poled $LiNbO_3$," Opt. Lett. 20, 52-54 (1995)

26. Walter R. Bosenberg, Lawrence E. Myers, Robert L. Byer, Alexander Drobshoff, and Jason I. Alexander, "Continuous-wave singly resonant optical parametric oscillator based on periodically poled $LiNbO_3$," Opt. Lett. 21, 713-715 (1996)

27. A. Galvanauskas, M. A. Arbore, M. M. Fejer, M. E. Fermann, and D. Harter, "Fiber-laser-based femtosecond parametric generator in bulk periodically poled $LiNbO_3$," Opt. Lett. 22, 105-107 (1997)

28. P. E. Britton, D. Taverner, K. Puech, D. J. Richardson, P. G. R. Smith, G. W. Ross, and D. C. Hanna, "Optical parametric oscillation in periodically poled lithium niobate driven by a diode-pumped Q-switched erbium fiber laser," Opt. Lett.23, 582-584 (1998)

29. Steven T. Yang and Stephan P. Velsko, "Frequency-agile kilohertz repetition-rate optical parametric oscillator based on periodically poled lithium niobate," Opt. Lett. 24, 133-135 (1999)

30. P. Loza-Alvarez, C. T. A. Brown, D. T. Reid, W. Sibbett, and M. Missey, "High-repetition-rate ultrashort-pulse optical parametric oscillator continuously tunable from 2.8 to 6.8 μm," Opt. Lett. 24, 1523-1525 (1999).

31. Zhaowei Zhang, Jinghua Sun, Tom Gardiner, and Derryck T. Reid, "Broadband conversion in an Yb:KYW-pumped ultrafast optical parametric oscillator with a long nonlinear crystal," Opt. Express 19, 17127-17132 (2011).

32. D. A. Bryan, R. Gerson, and H. E. Tomaschke, “Increased optical damage resistance in lithium niobate”, *Applied Physics Letters, 44*(9), 847-849 (1984).

33. Fabien Kéfélian, Haifeng Jiang, Pierre Lemonde, and Giorgio Santarelli, "Ultralow-frequency-noise stabilization of a laser by locking to an optical fiber-delay line," Opt. Lett. 34, 914-916 (2009).

34. Florian Adler, Konstantinos Moutzouris, Alfred Leitenstorfer, Harald Schnatz, Burghard Lipphardt, Gesine Grosche, and Florian Tauser, "Phase-locked two-branch erbium-doped fiber laser system for long-term precision measurements of optical frequencies," Opt. Express 12, 5872-5880 (2004).

35. Kroupa, Věnceslav F., ed. *Direct digital frequency synthesizers*. IEEE (1999).

36. E. Murphy, C. Slattery, “Direct digital synthesis (DDS) controls waveforms in test, measurement, and communications”, Analog Dialogue 39-08 (2005).

37. R. Gebs, G. Klatt, C. Janke, T. Dekorsy, and A. Bartels, "High-speed asynchronous optical sampling with sub-50fs time resolution," Opt. Express 18, 5974-5983 (2010).

38. M. Bousonville, and J. Rausch. "Reference Signal Generation with Direct Digital Synthesis for FAIR”, *11th International Conference on Heavy Ion Accelerator Technology, Venedig* (2009).

39. "Evaluating the AD9912 1 GSPS Direct Digital Synthesizer with 14-Bit DAC." http://www.analog.com/media/en/technical-documentation/user-guides/EVAL-AD9912A_PCBZ_UG-475.pdf.

40. P. K. Mukhopadhyay, K. Ozgoren, I. L. Budunoglu and F. O. Ilday, "All-Fiber Low-Noise High-Power Femtosecond Yb-Fiber Amplifier System Seeded by an All-Normal Dispersion Fiber Oscillator," in *IEEE Journal of Selected Topics in Quantum Electronics*, vol. 15, no. 1, pp. 145-152 (2009).

41. Z. Zhang, X. Fang, T. Gardiner, and D. T. Reid, "High-power asynchronous midinfrared optical parametric oscillator frequency combs," Opt. Lett.38, 2077-2079 (2013).

42. E. B. Treacy, "Optical pulse compression with diffraction gratings", IEEE J. Quantum Electron. 5 (9), 454 (1969).

43. S. V. Chernikov, D. J. Richardson, D. N. Payne, and E. M. Dianov, "Soliton pulse compression in dispersion-decreasing fiber," Opt. Lett. 18, 476-478 (1993).

44. Andrius Baltuška, Zhiyi Wei, Maxim S. Pshenichnikov, and Douwe A. Wiersma, "Optical pulse compression to 5 fs at a 1-MHz repetition rate," Opt. Lett. 22, 102-104 (1997).

45. Jens Biegert and Jean-Claude Diels, "Compression of pulses of a few optical cycles through harmonic generation," J. Opt. Soc. Am. B 18, 1218-1226 (2001).

46. Birgit Schenkel, Rüdiger Paschotta, and Ursula Keller, "Pulse compression with supercontinuum generation in microstructure fibers," J. Opt. Soc. Am. B 22, 687-693 (2005).

47. A. Couairon, M. Franco, A. Mysyrowicz, J. Biegert, and U. Keller, "Pulse self-compression to the single-cycle limit by filamentation in a gas with a pressure gradient," Opt. Lett.30, 2657-2659 (2005).

48. A. Ricci, A. Jullien, N. Forget, V. Crozatier, P. Tournois, and R. Lopez-Martens, "Grism compressor for carrier-envelope phase-stable millijoule-energy chirped pulse amplifier lasers featuring bulk material stretcher," Opt. Lett.37, 1196-1198 (2012).

49. E. Hecht, *Optics*, Pearsons, 4th edition (2001).

50. J.M. Dudley, D.T. Reid, W. Sibbett, L.P. Barry, B. Thomsen, and J.D. Harvey, "Commercial Semiconductor Devices for Two Photon Absorption Autocorrelation of Ultrashort Light Pulses," Appl. Opt. 37, 8142-8144 (1998).

51. Jinendra K. Ranka, Robert S. Windeler, and Andrew J. Stentz, "Visible continuum generation in air–silica microstructure optical fibers with anomalous dispersion at 800 nm," Opt. Lett. 25, 25-27 (2000).

52. T. A. Birks, W. J. Wadsworth, and P. St. J. Russell, "Supercontinuum generation in tapered fibers," Opt. Lett. 25, 1415-1417 (2000).

53. O. Fedotova, A. Husakou, and J. Herrmann, "Supercontinuum generation in planar rib waveguides enabled by anomalous dispersion," Opt. Express 14, 1512-1517 (2006)

54. John M. Dudley, Goëry Genty, and Stéphane Coen. "Supercontinuum generation in photonic crystal fiber." *Reviews of modern physics* 78.4: 1135 (2006).

55. Teresa I. Ferreiro, Jinghua Sun, and Derryck T. Reid, "Locking the carrier-envelope-offset frequency of an optical parametric oscillator without *f*–2*f* self-referencing," Opt. Lett. 35, 1668-1670 (2010).

56. J. M. Dudley, G. Genty, and S. Coen, Supercontinuum generation in photonic crystal fiber. *Reviews of modern physics*, *78*(4), 1135 (2006).

57. R. W. Boyd, *Nonlinear optics*. Academic press, 2003.

58. M. Prevedelli, T. Freegarde, and T. W. Hänsch, "Phase locking of grating-tuned diode lasers," Appl. Phys. B **60**, S241–248 (1995).

59. D. C. Edelstein, E. S. Wachman, and C. L. Tang, "Broadly tunable high repetition rate femtosecond optical parametric oscillator," Appl. Phys. Lett. **54**, 1728–30 (1989).

60. E. Rubiola, K. Volyanskiy and L. Larger, "Measurement of the laser relative intensity noise," *2009 IEEE International Frequency Control Symposium Joint with the 22nd European Frequency and Time forum*, Besancon (2009).

61. W. H. Press, S. A. Teukolsky, W. T. Vetterling, and B. P. Flannery, *Numerical Recipies: The Art of Scientific Computing*, Third edition (Cambridge University Press, 2007).

62. A. Abramovici, J. Chapsky, *Feedback Control Systems: A Fast-Track Guide for Scientists and Engineers*; Springer: Berlin, Germany (2010).

Chapter 4 – Mid-Infrared Dual Comb Spectroscopy with Methane

Prior work at Heriot-Watt by Zhang et al. [1] demonstrated the first dual-comb spectroscopy using an OPO, and this system operated in a mode where two femtosecond lasers pumped a single OPO. While this approach offers advantages in terms of stability [2,3], it places a limit on the repetition-frequency difference between the two combs because spectrally different idler pulses are produced when the pump repetition rates differ significantly [1]. Using a single OPO cavity also makes it complex to independently measure and control the carrier-envelope offset frequency (f_{CEO}) for each OPO [4], limiting the ability to utilize this signal for stabilization or calibration.

The research presented in this chapter introduces a dual-comb spectrometer in which, by simultaneously recording the DCS interferogram, repetition-rate and carrier-envelope offset frequencies, mid-infrared dual-comb spectroscopy in the region of the 3.3-μm methane absorption band is achieved by using two independent picosecond optical parametric oscillators. A unique and novel aspect of this work is that an absolute wavelength scale is provided which is entirely derived from radio-frequency references, achieving an absolute wavelength accuracy of 0.27 nm at 3150 nm.

4.1 Methane: A substantial contributor to greenhouse gases

Methane is the smallest hydrocarbon, an uncolored and non-smelling gas. It has a symmetrical nonpolar structure, where the carbon atom is surrounded by four hydrogen atoms in a perfectly tetrahedral arrangement. It is also a hot topic because it is one of the most potent greenhouse gases in Earth's atmosphere. In terms of the 100-year global warming potential of methane, it traps 28 times more heat per unit of mass than carbon dioxide, and 32 times that when one accounts for aerosol interactions [5]. Global methane levels, had risen to 1800 parts per billion (ppb) by 2011, an increase by a factor of 2.5 since pre-industrial times, from 722 ppb, the highest value in at least 800,000 years [6].

Methane can come from many sources, both natural and industrial. But the largest source of industrial emissions is the oil and gas industry (Fig. 4.1). The equilibrium between sources and sinks of methane is still under active investigation. The most prominent sink in the methane cycle is linked to the hydroxyl radical produced photochemically in the atmosphere. Production of this radical is not deeply understood and has a large influence

on atmospheric concentrations. According to observations that have shown between the year 2000 and 2006, atmospheric concentration of methane increases, and for this reason, it is aimed to monitor in depth [7].

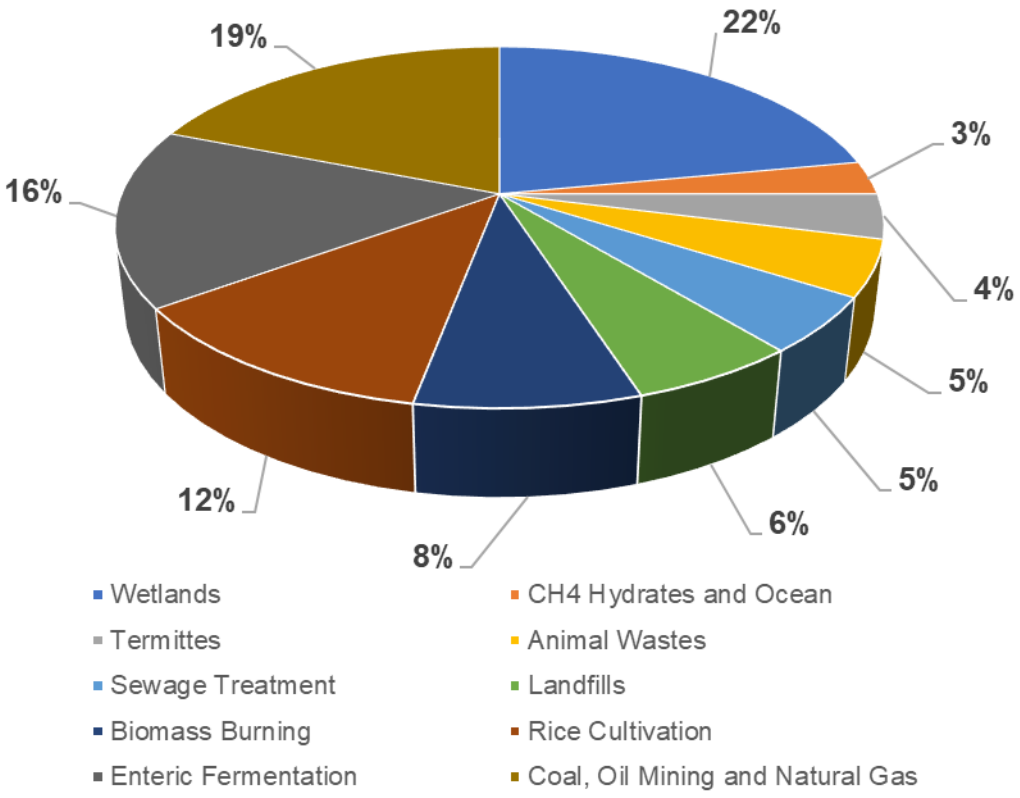

Figure 4.1: Global sources of methane showing current estimates for individual sources [8].

The IR spectrum of methane is quite distinguishable from spectra of larger hydrocarbons due to its simpler structure. In the IR spectrum of methane there are two strong absorption bands at 3020 cm^{-1}(3.3 µm) and 1300 cm^{-1} (7.7 µm) due to C-H stretching and bending modes, respectively (Fig. 4.2) [9]. Methane also absorbs more longer wavelength radiation in terms of higher infrared absorption cross section [10].

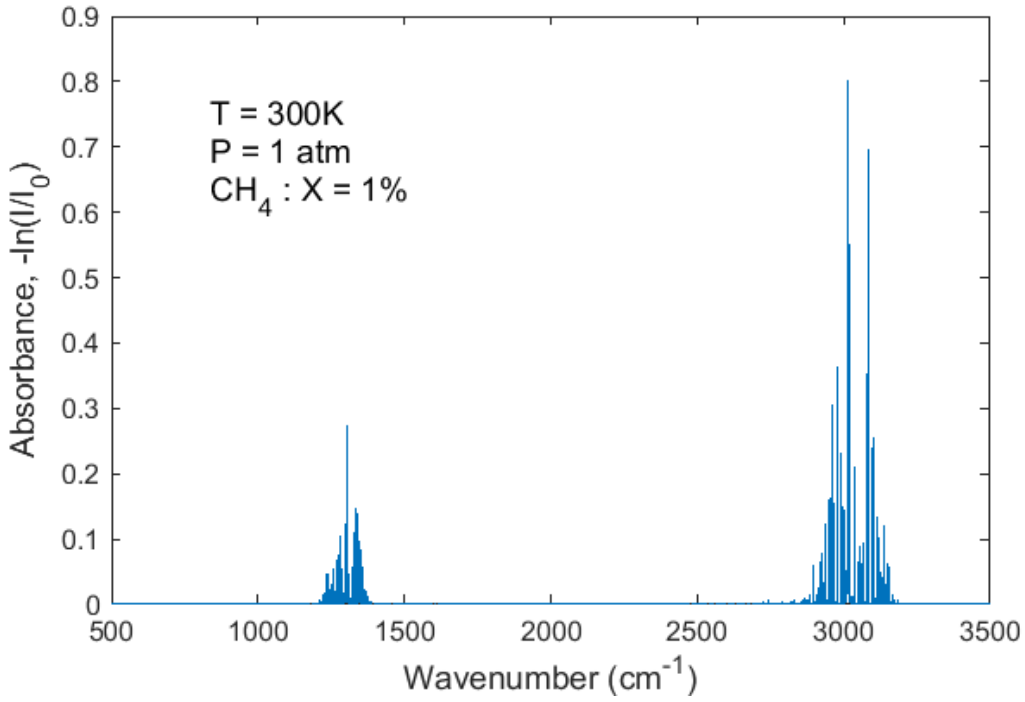

Figure 4.2: Infrared spectrum of methane. The principal peaks are defined as vibrational states of methane and others around the main peaks are the rotational states of the molecule [10].

Methane was chosen as a sample gas for evaluating the performance of the dual-comb spectroscopy system developed in this thesis because its spectroscopy is well documented and it exhibits absorption bands in a spectral region well-matched to PPLN OPO idler wavelengths. Furthermore, a comparison of experimental results with methane HITRAN data can support a detailed statement about the performance of the dual comb spectrometer.

4.2 Homodyne (symmetric) DCS with actively stabilized asynchronous OPOs

The pump lasers, locking electronics and OPOs were integrated into a complete dual-comb spectroscopy system for ro-vibrational gas spectroscopy. In the experiment, the DCS signal is detected with a mid-infrared detector and digitized by the data acquisition card. For ideally stable frequency combs, the sampled waveform can be Fourier-transformed to determine the optical spectrum easily. In reality, major challenges appear from the residual instabilities of the frequency combs, even when these benefit from state-of-the-art stabilization. The first spectroscopy experiment was carried out with actively stabilized asynchronous OPOs.

4.2.1 *Choice of* Δf_{REP}

Spectroscopy across the methane P, Q and R branches near 3000cm^{-1} requires a sufficient idler bandwidth, typically 200 - 400 cm^{-1}. Increasing the current to the pump fibre amplifier allows wider pump bandwidths to be generated through self-phase modulation, which in turn achieves broader idler bandwidths by exploiting parametric transfer of bandwidth from the pump to the idler [11]. Increasing the idler bandwidth implies reducing the maximum operating value of Δf_{REP} to comply with the dual-comb aliasing criterion (see Chapter 2). Figure 4.3 illustrates this trade-off. Ideally, operating at as high a value of Δf_{REP} is preferred because the faster acquisition time helps to obtain the dual-comb specta with relatively lower phase drifts.

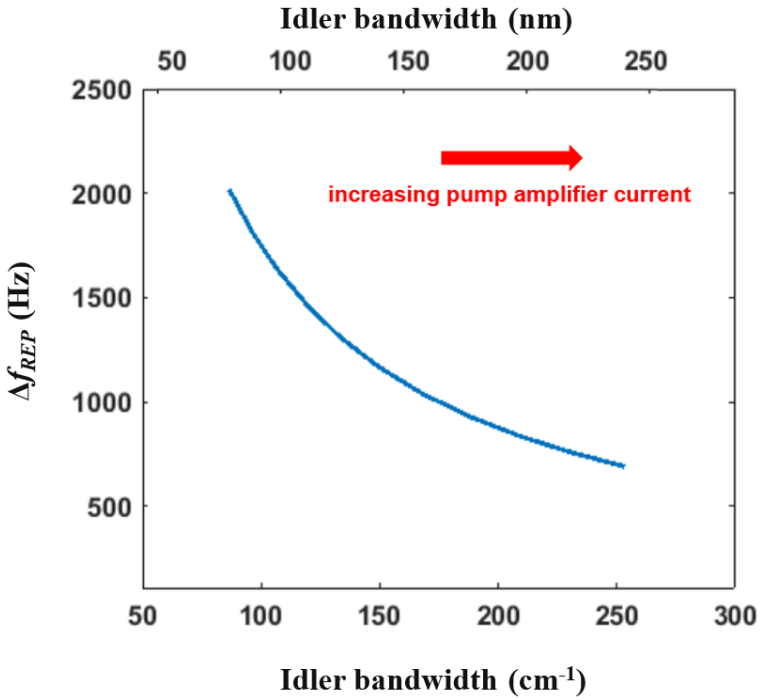

Figure 4.3: Maximum repetition frequency difference between two combs to avoid aliasing. Pump bandwidth is increased with increasing pump amplifier-current and correlates nearly directly to an equivalent idler bandwidth through the parametric transfer effect.

The maximum Δf_{REP} was compromised in terms of the pump spectral bandwidth by varying pump amplifier power. This power was optimized in order to send enough power for the nonlinear interferometry. In order to stabilize both OPOs, approximately 0.9 W was required from each pump laser at least. Therefore, each OPO generated an idler spectral bandwidth of 181 nm corresponding up to maximum repetition frequency of 1071 Hz which resulted in dual-comb interferograms exhibiting no aliasing.

4.2.2 *Spectrometer integration with f_{REP} and f_{CEO} stabilization unit*

In Chapter 3 actively stabilized asynchronous OPOs were described and examined in detail. An illustration of a dual-comb spectrometer with asynchronous OPOs, the integration of the pump lasers, nonlinear interferometry and OPOs into a complete dual-comb spectroscopy system is shown in Fig. 4.4. Firstly, the idler f_{CEO} for each channel was obtained from separate nonlinear interferometers which heterodyned the pump supercontinuum (pSC) with sum-frequency mixing (SFM) light between the pump and idler (p + i). These were implemented using a beamsplitter (BS1) to direct 30% of the pump light for each OPO to a grating compressor and into a photonic crystal fiber (PCF) to produce supercontinuum light at 800 nm. The spatially overlapped idler and undepleted pump beams exiting the OPO were focused by a concave silver mirror into a 2 mm long PPLN crystal with a grating period of 22 μm to generate SFM light with an average power of 1 mW. A dichroic mirror was used to separate the idler from the SFM light at 800 nm. The SFM light was combined with the pump supercontinuum and the heterodyne mixing signal detected by an avalanche photodiode (APD). A 10-nm bandwidth interference filter (IF) was used before the APD to improve the signal:noise level of the heterodyne frequency. By adjusting the time delay between the SFM and supercontinuum pulses, two signals were obtained containing the idler CEO frequencies of both channels independently.

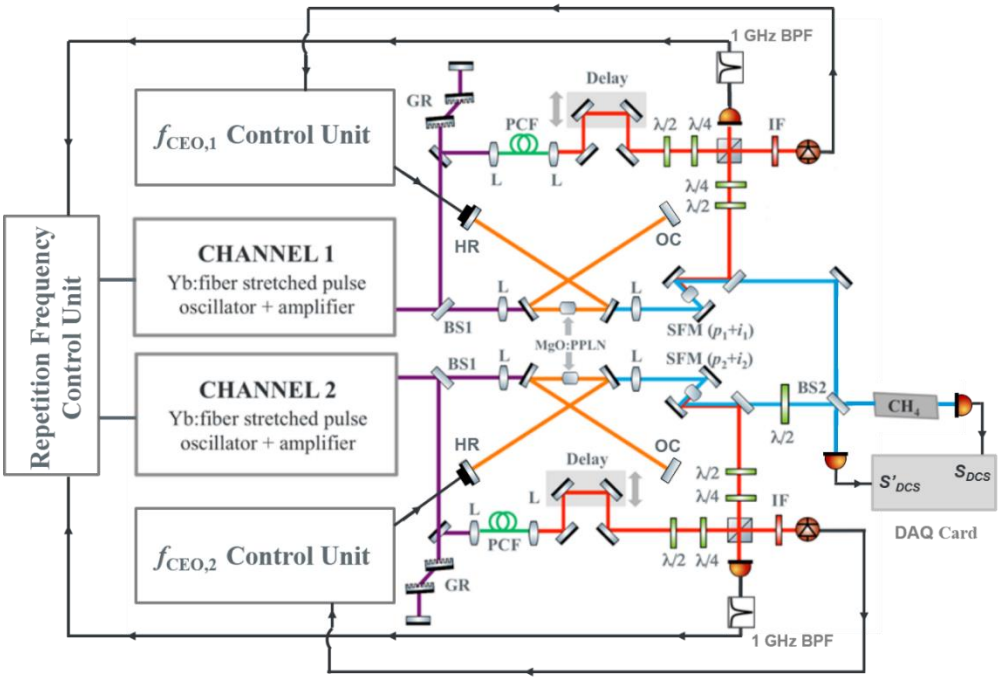

Figure 4.4: Layout of the mid-IR dual-comb spectrometer with repetition frequency and phase offset control units. HR, high reflectivity mirror; BS, beamsplitter; MgO:PPLN, periodically poled lithium niobate; SFM, sum-frequency mixing; PCF, photonic crystal fiber; L, lens; OC, output coupler; λ/2, half-wave plate; λ/4, quarter-wave plate; GR, transmission grating pairs; DAQ, data acquisition card.

The idler outputs of the OPOs were combined at a 50:50 CaF_2 beamsplitter before passing through a methane gas cell. This is a homodyne dual-comb scheme, in which pulses from both channels sample the gas absorption lines before detection. The gas cell was 20-cm long and contained a 1 atm mixture of N_2 with <1% of CH_4. The idler pulses were detected by a cryogenically cooled MCZT (HgCdZnTe) photovoltaic detector with a bandwidth of 100 MHz. The resulting signal was low-pass filtered to < 50 MHz to satisfy the Nyquist sampling condition to avoid aliasing before being digitized at 14 bits and 100 MSa/s. The typical idler power needed for dual-comb spectroscopy was <10 mW per channel, which resulted in a signal:noise ratio of 17 dB.

4.2.3 *Spectroscopic results from DCS*

In the first experiment the repetition rate of each fiber oscillator was approximately 102 MHz, while the repetition-frequency difference between the two channels was free-running at 216 Hz. The sequence of time-domain interferograms is shown in Fig. 4.4a, illustrating a repetition period of 4.6 ms ($1/\Delta f_{REP}$), and an example of one interferogram extracted from this dataset is shown in Fig. 4.4b. Fourier transforming a single interferogram within an 80-μs time window provided the dual-comb spectrum (Fig.4.4c), which was rendered in the optical domain by applying a scaling factor of $f_{REP}/\Delta f_{REP} = 4.74 \times 10^5$. Comparison with a Hitran simulation, [12] (Fig. 4.4d) using appropriate gas concentrations (0.8% methane at 1 atm in this measurement) indicated that the dual-comb spectrum had a resolution of 6 GHz (0.2 cm^{-1}). As can be seen in Fig. 4.4c, this resolution is sufficient to resolve detailed features in the P and R branches of the ro-vibrational spectrum, as well as the dense structure associated with the Q branch which shows around 90% absorption near 3.31 μm.

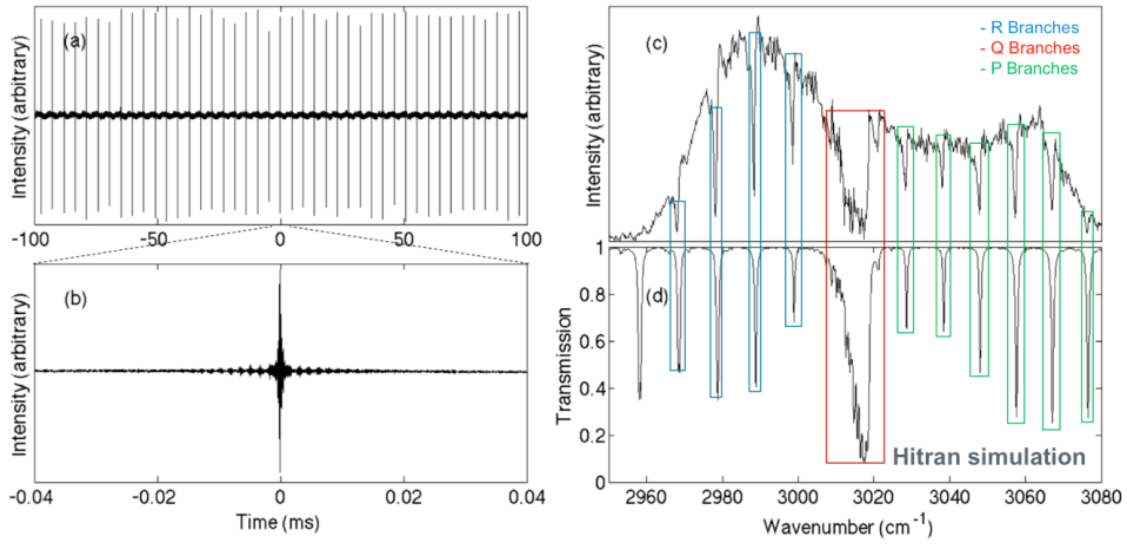

Figure 4.5: (a) Time-domain interferograms obtained from free-running OPOs with Δf_{REP} =216 Hz and (b) example of a single interferogram in an 80-μs time window corresponding to 0.2 cm^{-1} resolution. (c) Fourier-transform spectrum expressed in optical domain and (d) comparison with a Hitran simulation [12] for 0.8% CH_4 in N_2 at 1 atm.

Dual-comb spectroscopy was next implemented using the DDS repetition-rate stabilization and carrier-envelope offset stabilization explained in the previous chapter. The repetition rates of the fiber lasers were again approximately 102 MHz, but their difference was set to exactly Δf_{REP} = 300 Hz which was choosen as explained in Section 4.2. In this experiment the gas concentration was 0.5% methane in N_2 at 1 atm. We again observed resolutions of 0.2 cm^{-1}, indicating no resolution difference between the free-running spectroscopy and that obtained under full stabilization (Fig. 4.5).

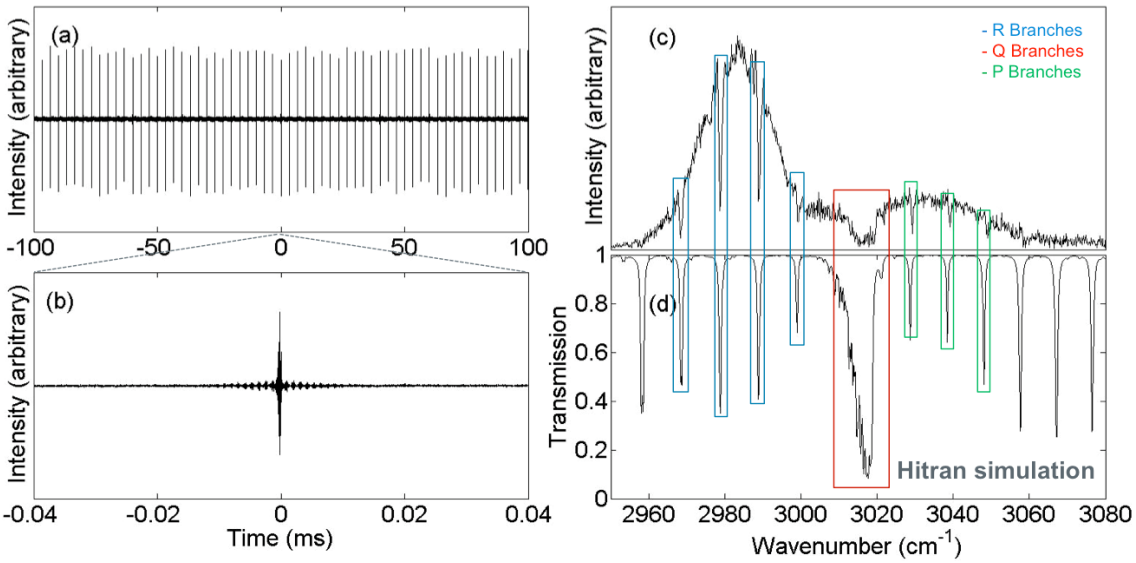

Figure 4.6: (a) Time-domain interferograms obtained with the repetition rates of the OPOs locked using the DDS system, resulting in Δf_{REP} =300 Hz and (b) example of a single interferogram in an 80-μs time window corresponding to 0.2 cm^{-1} resolution. (c) Fourier-transform spectrum expressed in optical domain and (d) comparison with a Hitran simulation for 0.5% CH_4 in N_2 at 1 atm.

4.2.4 *Analysis and discussions*

The DCS with fully stabilized OPOs suffered from frequency noise in the phase stabilization loop when the offset frequencies of both OPO combs were stabilized. This timing jitter distorted the acquired interferograms as a result of modulation fed back through the system. Therefore, consecutive interferograms lost their coherence and DCS was only available with fully stabilized OPOs when feedback modulations were limited to the modulation depth that is related to intracavity dispersion tuning. This issue was foreseen as a circumstance of systematic noise from the phase-locked loop when the noise of stabilized OPOs was discussed in Chapter 3.

In the case of the free running system, the passive stability of the f_{CEO} signal was measured from both idler channels by heterodyning the pump-idler sum-frequency light with the pump super-continuum, as described in Chapter 3. The f_{CEO} was digitized at a sampling rate of 10 ns for 200 ms and these data were used to construct the Allan deviation plots shown in Fig. 4.7a and the Fourier spectra of the datasets shown in Fig. 4.7b and Fig. 4.7c. The data show that over the typical acquisition time of a dual-comb spectrum (80 μs) the variance in f_{CEO} is ~200 kHz, while over 200-ms it is below 800 kHz. Over short timescales the variance in f_{CEO} is therefore comparable with the linewidth of the comb teeth, which even under well controlled conditions has been shown to be ~100 kHz [13] and is limited by the stability of the reference synthesizer used for f_{REP} stabilization. Although one channel shows poorer f_{CEO} stability than the other, we can conclude that over the time needed to acquire a dual-comb spectrum the f_{CEO} stability is comparable with the comb linewidth, so is unlikely to be the predominant factor limiting the spectral resolution. However its impact can still be significant.

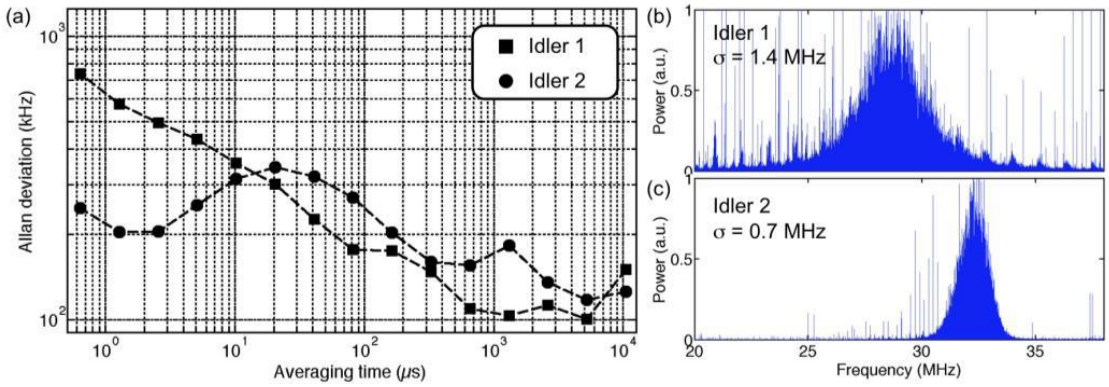

Figure 4.7: (a) Allan deviations and (b) Fourier spectra calculated from a 200-ms acquisition of the idler f_{CEO} signals.

4.3 Heterodyne (Asymmetric) DCS using absolute wavelength calibration with free-running asynchronous OPOs

In all implementations of mid-IR DCS there has to our knowledge been no absolute wavelength calibration reported which did not rely on a pre-existing optical reference such as a Fourier-transform spectrometer [2,3,14], an auxiliary reference laser [15-17] or spectral registration with a known gas spectrum [1,18]. In this section, by simultaneously recording the DCS interferogram, repetition-rate and carrier-envelope offset frequencies, we now demonstrate absolute optical wavelength calibration in a measurement of the mid-infrared dual-comb spectroscopy of methane gas using two free-running independent oscillators.

Dual comb spectroscopy as described in Section 4.2.1 was repeated without stabilization, but now with synchronous recording of the carrier-envelope frequencies of both OPOs (Fig. 4.8). The laser repetition frequencies f_{REP1} and f_{REP2} were sampled from the other output of the beamsplitter cube in the nonlinear interferometers. In order to obtain high resolution, the tenth harmonics of the repetition frequencies were detected following a 50-MHz-bandwidth RF filter centered at 1 GHz. Mixing these signals provided a third signal at the tenth harmonic of the repetition-frequency difference ($10\Delta f_{REP}$), necessary for accurate calibration. The absolute repetition frequency of Channel 1 was acquired with a precision frequency counter.

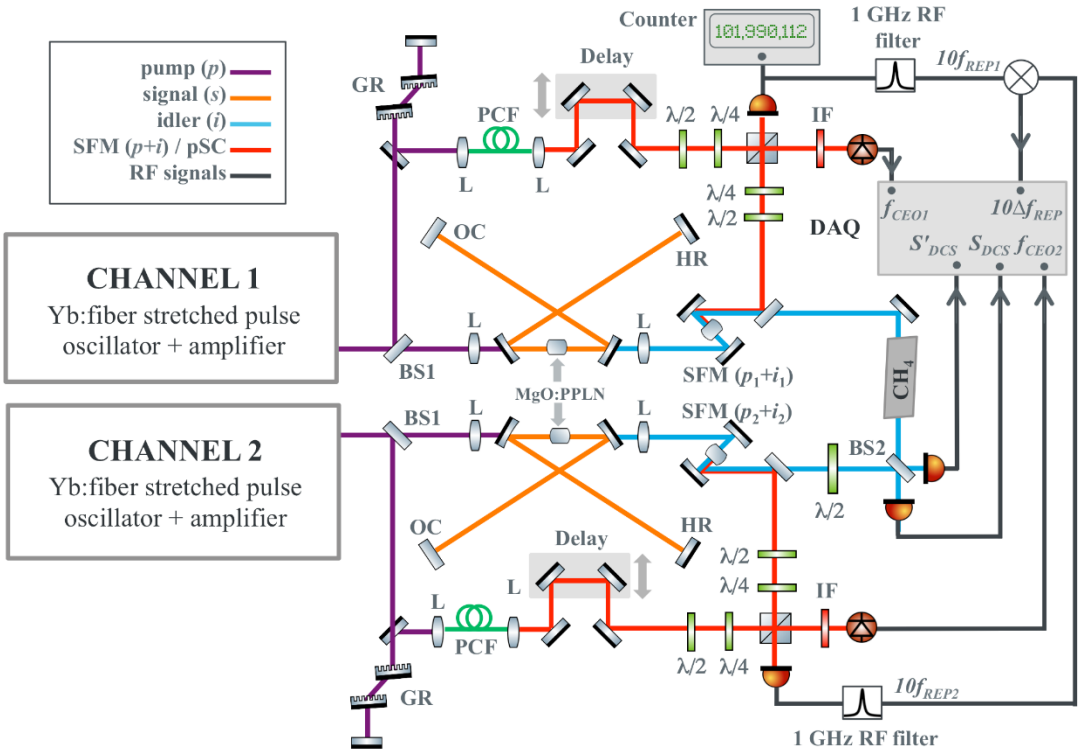

Figure 4.8: Layout of the mid-IR dual-comb spectrometer. HR, high reflectivity mirror; BS, beamsplitter; MgO:PPLN, periodically poled lithium niobate; SFM, sum-frequency mixing; PCF, photonic crystal fiber; L, lens; OC, output coupler; λ/2, half-wave plate; λ/4, quarter-wave plate; GR, transmission grating pairs; DAQ, data acquisition card.

The DCS configuration was a heterodyne scheme, in which idler pulses from one OPO passed through the gas cell before being combined with those from the other OPO at a 50:50 CaF_2 beamsplitter. The gas cell was 20 cm long and contained a 1 atm mixture of N2 with <1% of CH_4. A half-wave plate in one idler channel was used to adjust the power balance between the channels before detection. The idler pulses were detected by two identical cryogenically cooled HgCdZnTe detectors with a bandwidth of 100 MHz. Using two detectors allowed us to record the DCS interferogram signal (S_{DCS}) and its antiphase replica (S'_{DCS}). By differencing these signals, we significantly reduced common-mode noise present on the two channels. The typical idler power needed was <10 mW per channel. After Nyquist filtering to < 50 MHz, the DCS interferogram signals were sampled at 12-bit resolution at a rate of 200 MSa/s, together with the signals $10\Delta f_{REP}$ (= $10\Delta f_{REP1}$ - $10\Delta f_{REP2}$), f_{CEO1} and f_{CEO2}.

4.3.1 *Signal handling and wavelength calibration*

An overview of the signal handling and wavelength calibration process is presented in Fig. 4.9. Twenty-three consecutively acquired dual-comb interferograms were individually windowed, along with the co-acquired f_{REP}, f_{CEO} and Δf_{REP} calibration

signals, from which a unique look-up table was constructed for each spectrum. As observed in [19], residual instability in Δf_{REP} at the level of a few hundred mHz leads to nm-scale fluctuations in the centre wavelength of each spectrum, which if left uncorrected prevents spectral averaging. A full-spectrum cross-correlation approach was used to co-align the spectra with approximately 0.1-nm precision before averaging was implemented to yield the final spectrum.

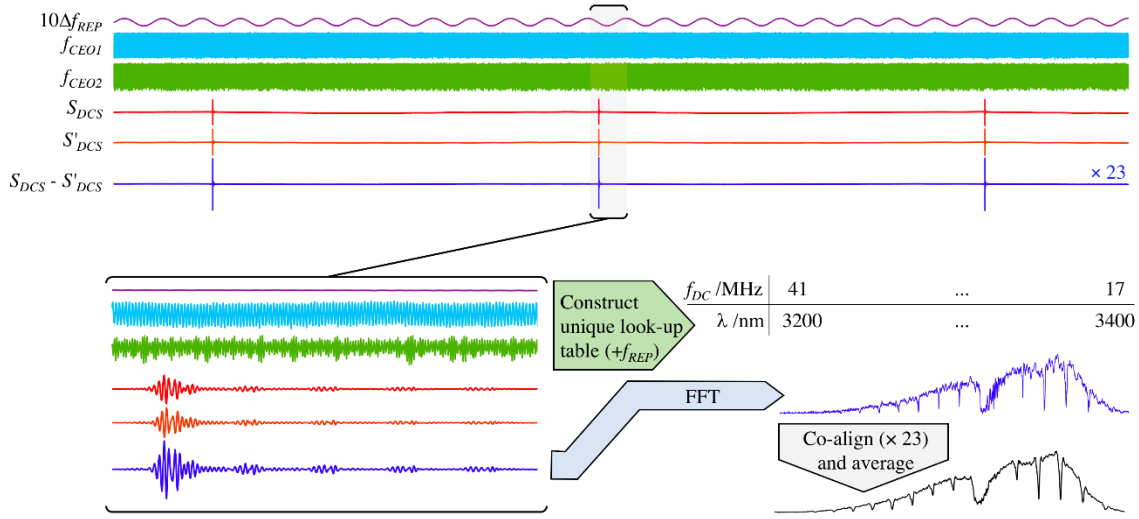

Figure 4.9: Signal handling and wavelength calibration process.

The digitized signals were processed in Matlab and a low-noise DCS interferogram obtained by differencing S_{DCS} and S'_{DCS}, after first balancing their powers. Power balancing was implemented numerically by using the Hilbert transform to extract the envelope of each interferogram. The interferograms were normalized using their respective envelopes before subtracting one from the other. By rejecting common-mode noise, this procedure improved the signal:noise ratio of the data by approximately a factor of three and enhanced the vertical symmetry of the resulting interferogram. The resulting interferogram was Fourier transformed and calibrated on an absolute wavelength scale in the following way.

Noting that the beat frequencies from the nonlinear interferometers may either be f_{CEO} or f_{REP} - f_{CEO}, the true offset frequencies for each comb were first determined. The wavelength range of interest was defined and then used to obtain the corresponding range of mode numbers for Comb 1:

$$n_1 = \frac{c}{f_{REP1}}\left(\frac{1}{\lambda_{MAX}} \cdots \frac{1}{\lambda_{MIN}}\right) \tag{4.1}$$

A wavelength range from 3.2 μm (λ_{MIN}) to 3.4 μm (λ_{MAX}) was selected, corresponding to mode numbers from 864437 – 918464. Except for very small values of Δf_{REP}, interference occurs between comb teeth of different mode numbers. In practice, we chose Δf_{REP} to be sufficiently high to provide a wide range of radio frequencies while still being low enough to avoid aliasing as explained in Chapter 2.

The mode-number difference was calculated as:

$$\Delta n = \left[\frac{c}{\lambda_{MAX} f_{REP2}}\right] - \left[\frac{c}{\lambda_{MAX} f_{REP1}}\right] \tag{4.2}$$

with the bracket notation representing rounding down to the nearest integer. Thus, for mode n_1 in Comb 1, the nearest mode in Comb 2 is $n_2 = n_1 + \Delta n$. Modes n_1 in Comb 1 and n_2 in Comb 2 interfere to produce a unique frequency in the DCS interferogram:

$$f_{DC} = f_1 - f_2 \tag{4.3}$$

where $f_1 = n_1 f_{REP1} + f_{CEO1}$ and $f_2 = n_2 f_{REP2} + f_{CEO2}$. Only the correct assignment for each channel of f_{CEO} to either the measured signal or f_{REP} - f_{CEO} (amounting to testing four different options) yields a value for f_{DC} which matches the experimental data. Once the correct assignments have been identified these persist for the entire set of interferograms.

The instantaneous frequencies of the $10\Delta f_{REP}$, f_{CEO1} and f_{CEO2} signals were obtained directly in the time domain using a zero-crossings algorithm to produce an average for each frequency within the time windows corresponding to the individual interferograms (~100 μs). After Fourier transforming, these frequencies were used along with f_{REP1} to create a look-up table which uniquely mapped f_{DC} to the wavelength of Comb 1, $\lambda = c/f_1$. Using this look-up table, each spectrum was individually calibrated in wavelength and stored for subsequent co-alignment to the other spectra prior to averaging the entire dataset.

The wavelength shifts were attributed to changes in Δf_{REP} which are unresolvable at the resolution of our current calibration system. The mapping between changes in wavelength λ and Δf_{REP} can be calculated in the following way.

In dual-comb spectroscopy a reduction factor of $\Delta f_{REP} / f_{REP}$ relates an interval in optical frequency δf_{OPT} to an interval in the radio frequency δf_{DC}. This allows an interval in radio frequency to be expressed as an interval in wavelength:

$$\delta f_{DC} = \frac{\Delta f_{REP}}{f_{REP}} \frac{c\delta\lambda}{\lambda^2} \tag{4.4}$$

The comb-mode equations show that an error in the repetition-frequency difference of $\delta(\Delta f_{REP})$ leads to an error in the interferogram carrier frequency of

$$\delta f_{DC} = n\delta(\Delta f_{REP}) \tag{4.5}$$

Thus for a mode number of n = 906,300 corresponding to the Q branch (λ = 3.31 µm) we find that a wavelength error of $\delta\lambda$ = 2.40 nm implies an error in the RF frequency of δf_{DC} = 0.359 Hz when Δf_{REP} = 500 Hz.

Consider N similar spectra, each of which is centered at a different position in the sampling grid. We calculate the relative shift, $\Delta\nu$, between any pair of spectra, $I_i(\nu)$ and $I_j(\nu)$ ($i, j \leq N$), by finding the location of the maximum of their cross-correlation [20]:

$$\delta\nu = \underset{\nu}{argmax}\left[I_i(\nu) * I_j(-\nu)\right] \tag{4.6}$$

Figure 4.10 illustrates a set of mutually shifted spectra (red, green and blue). Cross-correlation between any pair of spectra yields the magnitude and direction of their relative shift, allowing a table of mutual shifts to be formed, in the example this amounts to 3 × 3 values, including self-comparisons. The example in Fig. 4.10 shows three spectra separated from each other by shifts of between two and ten elements. The shift of each spectrum relative to the median can be computed by summing its mutual shifts and normalizing the resulting values by the number of spectra.

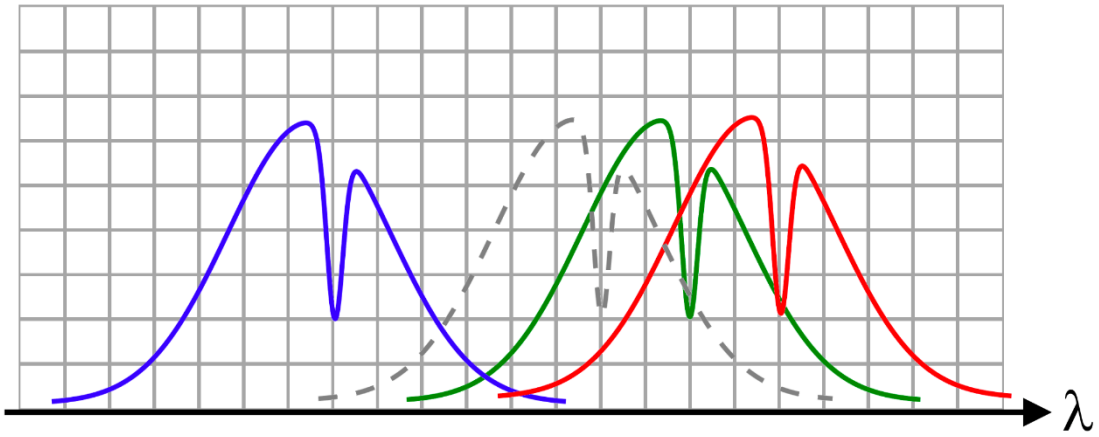

$n = 3$	RED	GREEN	BLUE
RED	0	-2	-10
GREEN	2	0	-8
BLUE	10	8	0
Σ / n	4	2	-6

Figure 4.10: For a set of mutually shifted spectra (red, green and blue) a table of relative shifts can be formed from mutual cross-correlations, whose columns can be summed and normalized to yield the relative shifts of each spectrum from the median position (gray dashed). Individual spectra are then co-aligned with the spectrum closest to the median (green) and averaged. Finally, the average spectrum is shifted by the required amount (2) to align it with the median position.

4.3.2 *Dual-comb spectroscopy of methane with absolute wavelength calibration*

The average of 23 calibrated spectra from consecutively acquired DC interferograms is shown in Fig. 4.11 (top, black line) superposed on a representative spectrum acquired from a single interferogram (top, gray). The inset shows visually the improvement in the signal-to-noise ratio provided by averaging multiple spectra. Incoherent averaging of 23 spectra should provide a factor of 4.80 ($\sqrt{23}$) improvement, and in the example presented here the root-mean-square noise in the region between the absorption lines decreases by 4.66, close to the expected value.

Figure 4.11 (lower panel) shows the result of implementing a best fit using the HITRAN 2012 database to the measured transmittance data [12]. The best fit was obtained for a resolution of 0.5 cm^{-1}, a methane concentration of 0.68% and a wavenumber (wavelength) shift of 0.25 cm^{-1} (0.27 nm). This shift reveals the accuracy limit of the calibration method as implemented, but which could be improved in many ways. Averaging more

spectra would reduce the noise and improve the absolute accuracy further, however data acquisition constraints placed a limit on the number of interferograms which could be acquired in our current implementation. The standard deviation observed in the set of individually calibrated spectra would be reduced by recording a higher harmonic of Δf_{REP}. In this demonstration, we acquired $10\Delta f_{REP}$, however this could be extended significantly further by heterodyning higher harmonics of the repetition frequency using high-speed detectors, or by directly recording a high harmonic of Δf_{REP} by mixing the pump combs on a high-speed two-photon absorption photodiode.

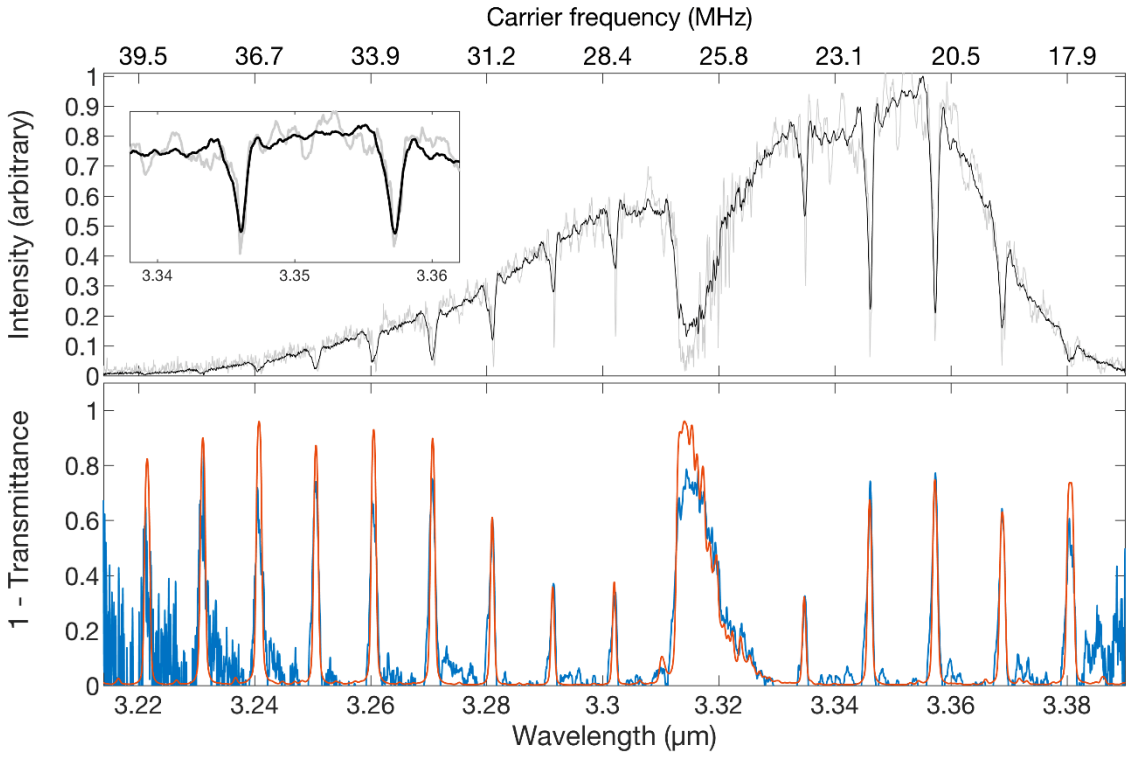

Figure 4.11: Top: Average of 23 calibrated spectra after re-centering on the median wavelength (black) and comparison with a single representative spectrum (gray). The inset illustrates the 4.66× improvement in RMS noise between two adjacent absorption features, close to the expected factor of 4.80 ($\sqrt{23}$). Bottom: Comparison of the measured transmittance (blue) with a HITRAN 2012 best fit for 0.68% methane in nitrogen for a 20-cm path length and a resolution of 0.5 cm^{-1} (red). An offset of 0.25 cm^{-1} (0.27 nm) was applied to the data to obtain the best fit, corresponding to the residual inaccuracy of the calibration.

The HITRAN comparison shows that the experimental transmittance spectrum clearly resolves the P and R branches of the ro-vibrational spectrum, as well as some of the structure associated with the Q branch (near 3.32 μm). Saturation effects in this region are responsible for the deviation between the experimental and HITRAN data in this region.

4.3.3 *Analysis and discussions*

As the results in the previous section demonstrate, the f_{CEO}-based wavelength calibration technique for mid-IR DCS provides the high signal:noise ratio, broad bandwidth and sub-cm^{-1} resolution necessary to resolve gas-phase ro-vibrational absorption lines. Using the tenth harmonic of the repetition frequency difference allows Δf_{REP} to be determined with better accuracy, however short-term excursions of Δf_{REP} introduce wavelength shifts in the calibrated spectra of up to a few nm. The total recording time for the dual-comb data was 50 ms, corresponding to a Nyquist-limited resolution of 20 Hz, but providing Δf_{REP} to a nominal 2 Hz resolution. This is the origin of the uncertainty which is responsible for the deviations in the wavelength calibrations of the different spectra which can be seen in Fig. 4.9, in which the spectra of 23 consecutively acquired interferograms are shown as an intensity map.

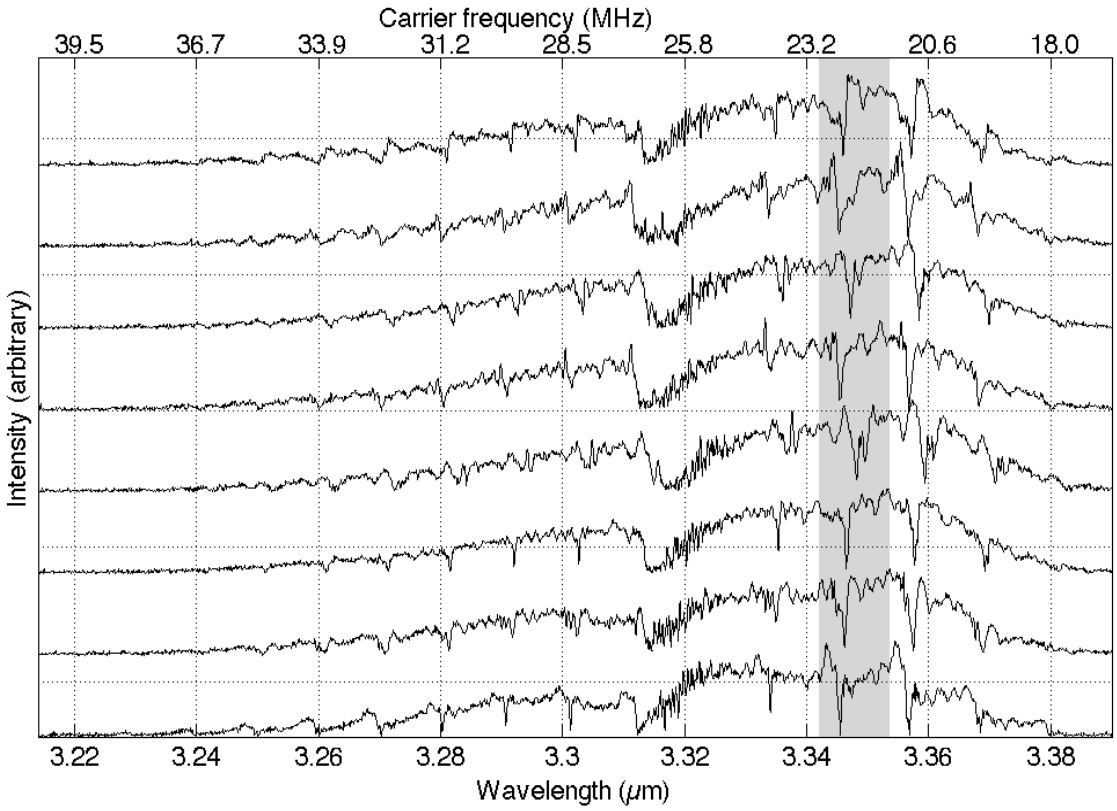

Figure 4.12: Spectra of eight consecutively acquired interferograms, shown after calibration onto a common wavelength scale. The equivalent radio-frequency scale is also shown for comparison.

Dealing with this problem by using co-alignment to an independently measured narrow spectral feature was proposed in the original demonstration of mid-IR DCS [19] and was recently implemented in an OPO DCS system [21]. In fact, an independent reference is not necessary for accurate co-alignment. Instead, we achieved this by computing the misalignment between each spectrum and every other spectrum from their cross-

correlations, amounting to 23 × 23 comparisons, when self-comparisons are counted. Such a correlation method [19] is general, very reliable and automatically returns the median location around which the spectra are evenly shifted. The shifts identified in this way are shown in Fig. 4.10 for the entire dataset and exhibit a standard deviation in wavelength of 2.4 nm, or 359 mHz in the repetition-frequency difference. The error in calculating the relative shifts is estimated to be less than 0.1 nm, but for clarity no corresponding error bars have been shown in Fig. 4.10.

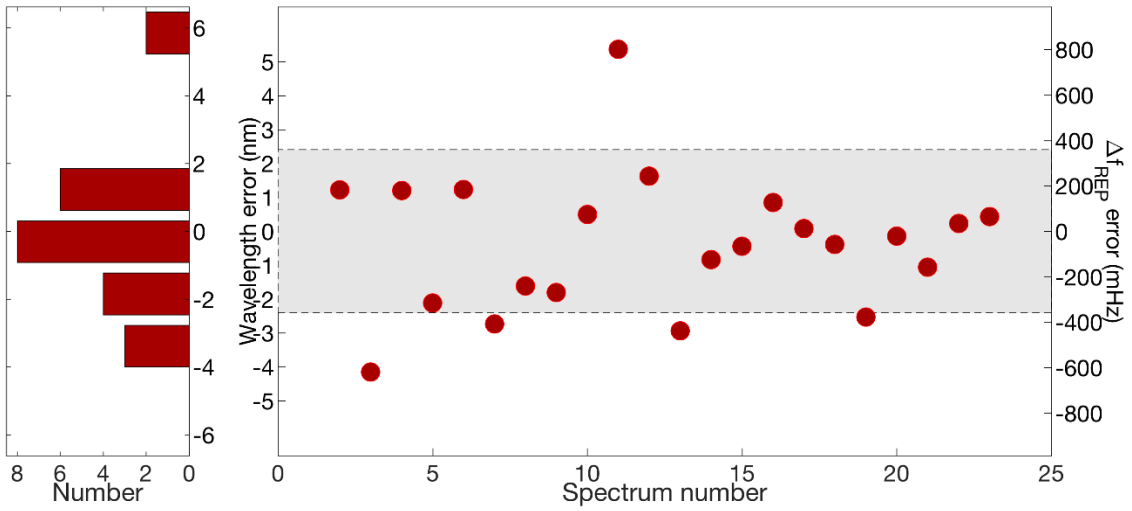

Figure 4.13: Residual shifts of the center positions of every spectrum from the median wavelength value after implementing the wavelength calibration procedure (left axis) and the equivalent error in Δf_{REP} which would lead to these deviations (right axis). The gray region indicates the standard deviation of the data and the histogram (far left) shows the frequency distribution of different wavelength shifts. The uncertainty in calculating the shifts between spectra is less than 0.1 nm (error bars not shown).

4.4 Conclusion

In this chapter, the dual-comb mid-infrared spectroscopy is firstly demonstrated using two independent MgO:PPLN based OPOs, whose high degree of passive stability provides an accessible means of implemention with high signal:noise ratio, broad bandwidth and sub-cm^{-1} resolution; necessary to resolve gas-phase ro-vibrational absorption lines. This made it possible to acquire high quality data under standard laboratory conditions without the need for active repetition-rate stabilization, demonstrating performance equivalent to that obtained using full stabilization whose performance is limited by the OPO design aspect of using a long crystal. In the first spectroscopy measurement here, only 8000 pairs of pulses contribute to each dual-comb spectrum and provide a signal:noise ratio of ~17 dB, implying that spectroscopy from single interferograms should be possible even at acquisition rates exceeding 1 kHz. In

our current system, the comb spacing of 102 MHz and the idler bandwidth limits the maximum repetition-rate difference to <700 Hz, since higher values of Δf_{REP} lead to aliasing in the RF comb.

A f_{CEO}-based wavelength calibration technique for mid-IR DCS has been also introduced to achieve the high signal:noise ratio, broad bandwidth and sub-cm^{-1} resolution necessary to resolve gas-phase ro-vibrational absorption lines. Noise reduction using averaging of multiple interferograms and balanced detection provided a high quality DCS spectrum. The calibration approach benefits from operating at a high repetition frequency difference. Doing this distributes the wavelength scale across a wider range of frequencies, so fluctuations in f_{CEO} – which only contribute additively to the interferogram frequency – have less impact. It should be possible to further improve the calibration precision by recording a very high harmonic of Δf_{REP}, either by heterodyning high harmonics of f_{REP1} and f_{REP2} or by other techniques.

4.5 References

1. Z. Zhang, T. Gardiner, and D. T. Reid, “Mid-infrared dual-comb spectroscopy with an optical parametric oscillator,” Opt. Lett. 38, 3148–3150 (2013).

2. Y. Jin, S. M. Cristescu, F. J. M. Harren, and J. Mandon, "Two-crystal mid-infrared optical parametric oscillator for absorption and dispersion dual-comb spectroscopy," Opt. Lett. 39, 3270-3273 (2014).

3. Y. Jin, S. M. Cristescu, F. J. M. Harren and J. Mandon, "Femtosecond optical parametric oscillators toward real-time dual-comb spectroscopy," Appl. Phys. B 119, 65-74 (2015).

4. Z. Zhang, X. Fang, T. Gardiner, and D. T. Reid, "High-power asynchronous mid-infrared optical parametric oscillator frequency combs," Opt. Lett. 38, 2077-2079 (2013).

5. Myhre, Gunnar; Stocker, T.F.; Qin, D.; Plattner, G.-K.; Tignor, M.; Allen, S.K.; Boschung, J.; Nauels, A.; Xia, Y.; Bex, V.; Midgley, P.M., eds., "Anthropogenic and Natural Radiative Forcing", Climate Change 2013: The Physical Science Basis. Contribution of Working Group I to the Fifth Assessment Report of the

Intergovernmental Panel on Climate Change, Cambridge, United Kingdom and New York, NY, USA: Cambridge University Press, retrieved 2016-12-22 (2013).

6. Drew T. Shindell; Greg Faluvegi; Dorothy M. Koch; Gavin A. Schmidt; Nadine Unger; Susanne E. Bauer, “Improved attribution of climate forcing to emissions”, Science 326 ed., pp. 716–718 (2009).

7. IPCC AR5 WG1. "Climate Change 2013: The Physical Science Basis Summary for Policymakers". Cambridge University Press (2013).

8. Augenbraun, Harvey; Matthews, Elaine; Sarma, David; “The Global Methane Cycle”, Global Methane Inventory, NASA (1997).

9. NIST Chemistry WebBook; www.webbook.nist.gov/chemistry/

10. SpectraPlot; www.spectraplot.com

11. Zhaowei Zhang, Jinghua Sun, Tom Gardiner, and Derryck T. Reid, "Broadband conversion in an Yb:KYW-pumped ultrafast optical parametric oscillator with a long nonlinear crystal," Opt. Express 19, 17127-17132 (2011).

12. L.S. Rothman et al , "The HITRAN2012 molecular spectroscopic database," J. Quant. Spectrosc. Radiat. Transfer 130 4–50 (2013).

13. K. Balskus, S. Schilt, V. J. Wittwer, P. Brochard, T. Ploetzing, N. Jornod, R. A. McCracken, Z. Zhang, A. Bartels, D.T. Reid, and T. Südmeyer, "Frequency comb metrology with an optical parametric oscillator," Opt. Express 24, 8370-8381 (2016).

14. G. Villares, J. Wolf, D. Kazakov, M. J. Süess, A. Hugi, M. Beck, and J. Faist, “On-chip dual-comb based on quantum cascade laser frequency combs,” Appl. Phys. Lett. 107, 251104 (2015).

15. E. Baumann, F. R. Giorgetta, W. C. Swann, A. M. Zolot, I. Coddington, and N. R. Newbury, "Spectroscopy of the methane ν3 band with an accurate mid-infrared coherent dual-comb spectrometer," Phys. Rev. A 84, 062513 (2011).

16. V. O. Smolski, H. Yang, J. Xu, K. L. Vodopyanov, " Massively parallel dual-comb molecular detection with subharmonic optical parametric oscillators," arXiv:1608.07318.

17. V. O. Smolski, K. F. Lee, C. Mohr, J. Jiang, I. Hartl, M. Fermann, and K. L. Vodopyanov, "Phase Locked System for Dual Comb Molecular Spectroscopy at 2-6 µm Based on Tm-fiber Laser," in CLEO: 2014, OSA Technical Digest (online) (Optical Society of America, 2014).

18. G. Villares, A. Hugi, S. Blaser, and J. Faist, “Dual-comb spectroscopy based on quantum-cascade-laser frequency combs,” Nat. Commun. 5, 6192 (2014).

19. A. Schliesser, M. Brehm, F. Keilmann, and D. W. van der Weide, "Frequency-comb infrared spectrometer for rapid, remote chemical sensing," Opt. Express 13, 9029-9038 (2005).

20. C. H. Knapp and G. C. Carter. "The generalized correlation method for estimation of time delay," IEEE Transactions on Acoustics, Speech and Signal Processing, 24, 320-327 (1976).

21. Y. Jin, S. M. Cristescu, F. J. M. Harren, and J. Mandon, "Dual-Frequency Comb Spectroscopy: A Digital Solution for Coherent Averaging," in Conference on Lasers and Electro-Optics, OSA Technical Digest (2016) (Optical Society of America, 2016), paper SW1H.8.

Chapter 5 - Mid-IR Dual Comb Spectrometer with OPGaP Based OPOs

Infrared spectroscopy in the spectral fingerprint region from 6–12 µm accesses the largest molecular absorption cross-sections, permitting sensitive, quantitative and species-specific measurements. This chapter explains how dual-comb spectroscopy can be extended to the 6–8-µm wavelength band using femtosecond optical parametric oscillators (OPOs) configured with OPGaP crystals.

5.1 A New and Significant Nonlinear Crystal: Orientation Patterned Gallium Phosphide

Zincblende semiconductors such as orientation-patterned gallium arsenide (OP-GaAs) and gallium phosphide (OP-GaP) are recently developed materials and the first new orientation patterned semiconductors to produce nonlinear optical frequency downconversions with significant output powers because of their high second-order nonlinearity and infrared transparency beyond 10 µm [1]. The OPGaP crystal has a band edge lying in the visible region, so two-photon absorption in this crystal becomes negligible in the convenient pumping range 1 – 1.7 µm, while its transparency extends to 12 µm, providing excellent coverage of the fingerprint region [2]. This ability to be pumped at 1 µm makes it distinct from OP-GaAs OPOs, which require pumping at wavelengths typically in excess of 1.7 µm, a spectral region where high quality laser sources are less readily available. The first OP-GaP based OPO pumped by a Yb:fibre laser was demonstrated by Maidment et al in 2016 [3] and provided an opportunity to implement such OPOs for dual comb spectroscopy in the fingerprint region.

5.1.1 *Phasematching properties of OP-GaP*

Gallium phosphide (GaP) is a polycrystalline material that is composed by semiconductor of groups “III-V” crystallize into the cubic zinc blende form whose unit cell is almost same as the diamond form [4]. The atoms of gallium and phosphide have 3 and 5 electrons which are generally bonded with covalent, ionic and neutral binding in in combination of gallium and phosphorus.

Table 5.1: Optical properties of gallium phosphide crystal

Nonlinear coefficient, d_{ij} [pm/V]	70.4 (@1 µm) [5]
Transmission range (µm)	0.57 – 12 [2]
Point group	43m (cubic) [4]
Crystal cut for QPM (µm)	800 [6]
Refractive index	3.18 (@1 µm) [7]
Walkoff (pump-signal)	268– 293 fs/mm for λ_s = 1.20 – 1.22
Walkoff (pump - idler)	892 – 863 fs/mm for λ_i = 6.50 – 7.6

Its optical properties are shown in Table 5.1. Such characteristics and its substantial nonlinearity of 70.6 pm V^{-1} allow it to be pumped directly with 1-µm Yb:fibre lasers, and the domain patterning period enables the desired tuning parameters required to cover the material's full transparency range (Fig. 5.1) [2].

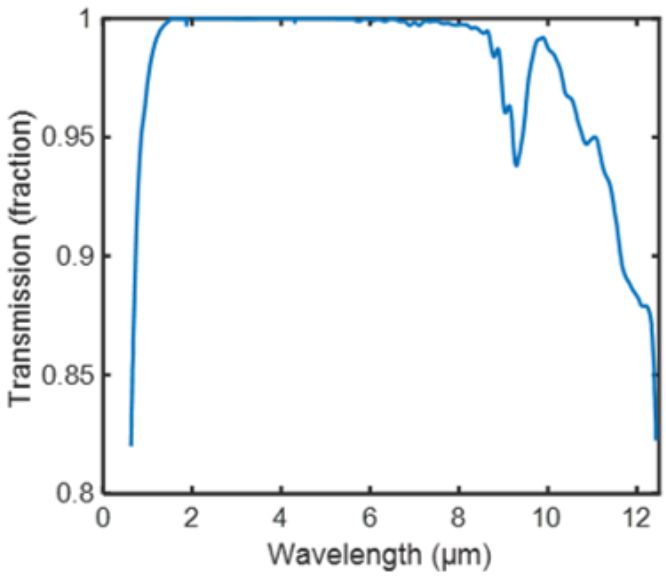

Figure 5.1: Transmission of 1 mm OP-GaP crystal [2]. Transmission window of OP-GaP crystal is between 0.56 µm and 12.3 µm.

Refractive index of GaP material is typically determined as a function of wavelength. This characterization is defined by Sellmeier equation:

$$n^2(\lambda) = 1 + \frac{A_1\lambda^2}{\lambda^2 - A_2} + \frac{B_1\lambda^2}{\lambda^2 - B_2} + \frac{C_1\lambda^2}{\lambda^2 - C_2} + \frac{D_1\lambda^2}{\lambda^2 - D_2} \qquad (5.1)$$

where n is the refractive index, and $A_{1,2}$, $B_{1,2}$, $C_{1,2}$, and $D_{1,2}$ are experimentally investigated Sellmeier coefficients. These coefficients for OP-GaP crystal are 1.39, 0.172, 4.131, 0.234, 2.57, 0.345, 2.056, and 27.52 respectively [8]. Fig. 5.2 shows refractive index of OP-GaP crystal in its transparency window.

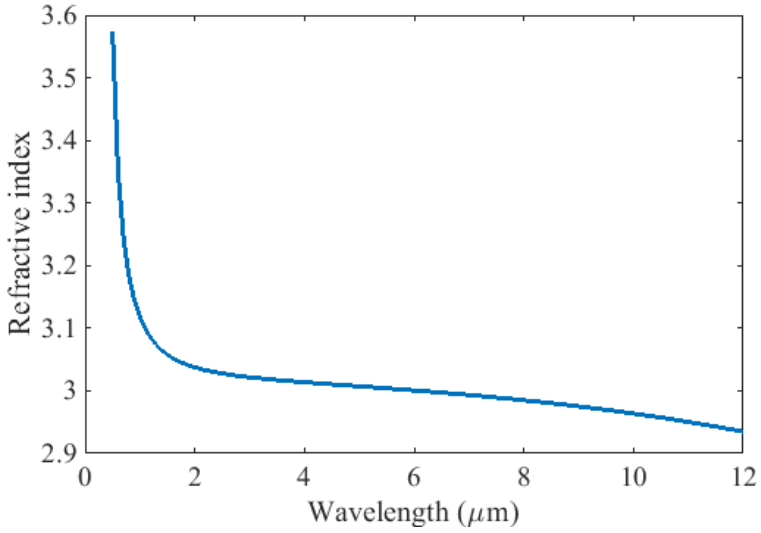

Figure 5.2: Refractive index of gallium phosphide defined by Sellmeier equation. Its refractive index becomes higher under 1 µm.

QPM in GaP material has been developed for fabricating a periodic pattern of domain orientation. This technique was firstly applied on gallium arsenide material [1]. However, OP-GaAs has a high two-photon absorption (2PA) in range of the conventional pump lasers (1-1.7 µm) [9]. On the other hand, GaP has a negligible 2PA in the same range. Fabrication technique of OP-GaP crystal will be discussed in the next section.

Interaction length of OP-GaP crystal is limited by temporal overlap between pump, signal and idler pulses in terms of their different group velocities. The temporal walk off between these wavelengths associate with the crystal length. With a 1-mm-long OPGaP, pump-signal and pump-idler walk off are presented in Fig. 5.3. By contrast with 20-mm-long PPLN crystal, 1-mm-long OPGaP crystal requires dechirped pulses in order to preserve the signal in the bandwidth of the pump to generate the idler photons efficiently.

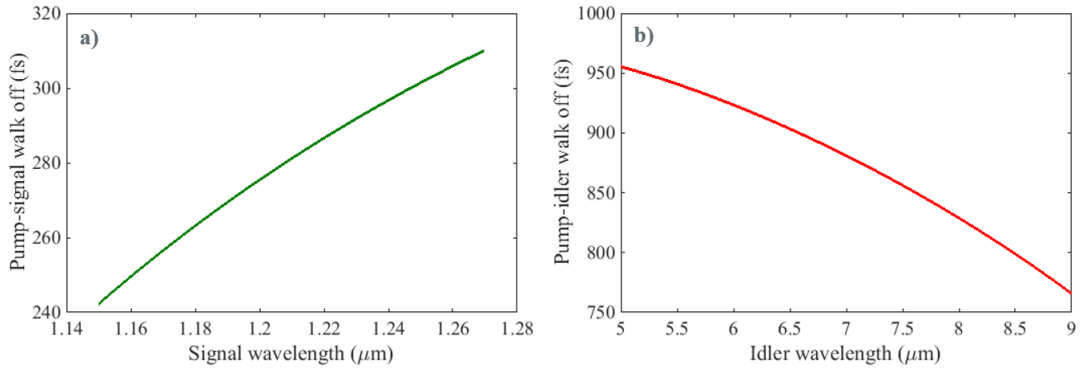

Figure 5.3: (a) Pump-signal walk off and **(b)** pump-idler walk off for signal and idler wavelengths in a 1-mm-long OP-GaP crystal respectively.

The colour-map in figure 5.4 illustrates the phase-matching efficiency for a 1-mm-long OPGaP crystal, along with the transmission spectrum of OP-GaP. The wavevector mismatch (Eq. 2.17) was calculated over a matrix of grating periods (Λ) and signal / idler wavelengths and used to provide the phasematching efficiency factor $\mathrm{sinc}^2(\Delta kL/2)$, where L is the crystal length of 1 mm. The phase-matching bandwidth was modelled for pump wavelengths from 1020–1060 nm at 1 nm intervals and its conversion efficiency was obtained for different grating periods. To specifically consider desired grating periods which are required to generate idlers (6-8 µm) for methane absorption spectroscopy, idler bandwidths were calculated using pump spectral density. According to this calculation, the optical parametric oscillation is suitable with using 1-mm-long crystals pumped by nearly bandwidth-limited pump pulses which is estimated in terms of temporal walkoff length of 1-mm-long OPGaP crystal. The idler generation is thereby possible throughout the OP-GaP transparency window by tuning the quasi-phase-matching period from 24–27 µm, values which correspond to move idler wavelengths with very broad continuous spectral bandwidth (~500 nm) into deep-infrared region.

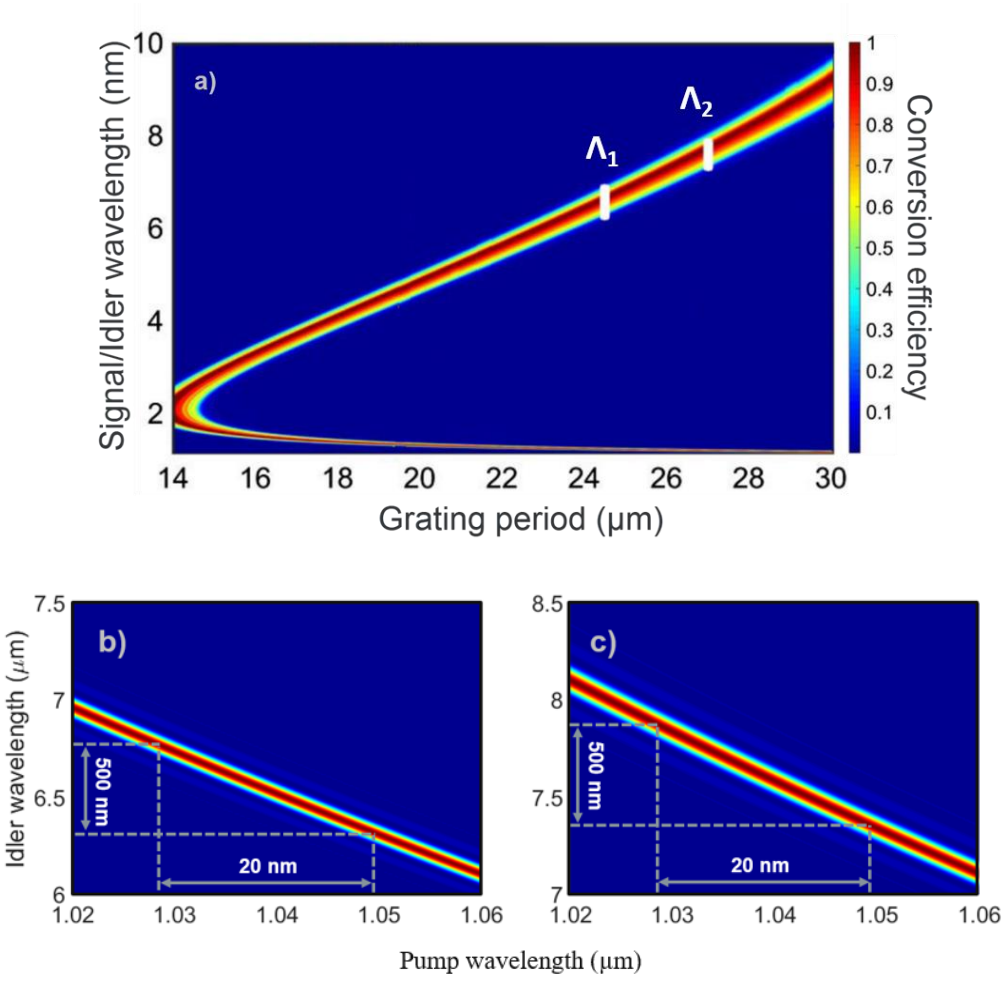

Figure 5.4: (a) Phase-matching efficiency for a 1-mm-long OP-GaP crystal, calculated using the Sellmeier equation from [9]. Idlers are obtained with grating periods of **(b)** Λ_1=24.5 µm and **(c)** Λ_1=27 µm in which DCS requires mid-infrared wavelength.

5.1.2 *Fabrication and preparation of the OP-GaP crystals*

An OP-GaP wafer was fabricated with many distinctive regions including patterning periods in the desired range by the all-epitaxial processing technique originally developed for the growth of OP-GaAs [1,11]. This method is based on the use of polar-on-nonpolar molecular beam epitaxy (MBE) to produce a III-V semiconductor layer whose orientation is inverted relative to that of the substrate [10,12]. The 75 mm wafer produced by MBE is shown in Fig. 5.5a, and presented excellent vertical, parallel domain propagation even for the smallest periods. Fig. 5.5b,c shows the polished and etched cross-section of the OP-GaP sample used in the required phase-matching conditions (1-mm-long, 24.5 and 27-µm grating period, and 800 µm QPM layer thickness) [6]. Therefore excellent parallel, vertical domain propagation was achieved up to the growth interruption at 150 microns. OP-GaP crystals with lengths of 1 mm were diced from the wafer, polished then anti-reflection (AR) coated for near- to mid-infrared wavelengths (1.02 - 1.06, 1.15 - 1.35 and 5 – 12 µm).

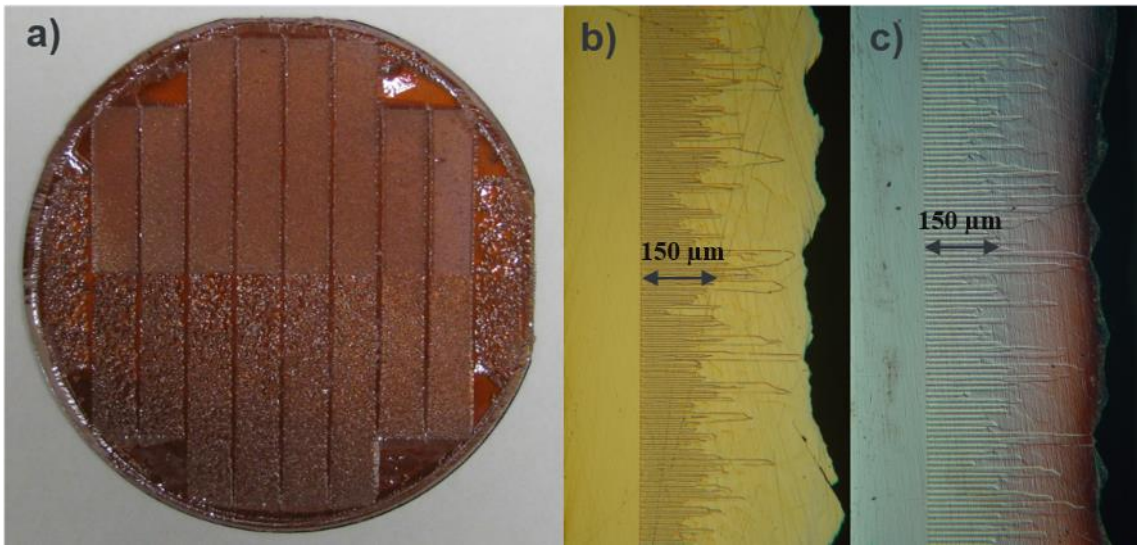

Figure 5.5: (a) The layout of the domain regions on the 75-mm OP-GaP wafer is shown together with cross sections revealing the domain-period growth. The inset on the right shows a diced and anti-reflection coated crystals with gratings of 24.5 µm **(b)** and 27 µm **(c)** which have both aperture of 150 µm.

5.1.3 *Crystal mounting*

The OP-GaP crystal for each grating was glued onto an aluminium adapter that made it possible to insert crystals of different grating periods into the main crystal mount. This mount was designed for maximum beam clearance to access both sides of the crystal and to permit the introduction of crystals with different grating periods without requiring significant cavity re-alignment (Fig. 5.6). The entire crystal mount was assembled in a lockable 1-inch optical mount to align the aperture angle of the crystal appropriately.

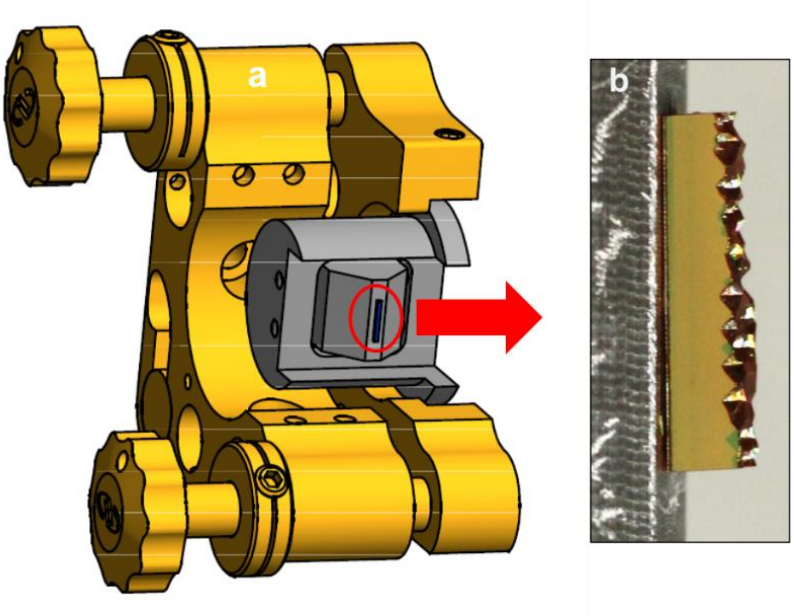

Figure 5.6: (a) The homemade crystal mount for OPGaP crystal and (b) mounted OP-GaP crystal glued on a separate aluminium base.

5.2 Singly Resonant OP-GaP based OPOs

Two identical synchronously pumped OP-GaP OPOs are configured in two independent 102-MHz ring resonator cavities with high reflectivity from 1.15–1.35 µm (Fig. 5.7), pumped with dechirped pulses (~ 170 fs) from the Yb:fibre lasers whose center wavelength of 1041 nm was shifted by an interference filter inside the oscillator cavity and compressed by a transmission grating pair after immediately chirped-pulse amplifier as mentioned in Chapter 3. As with the first generation OPO the cavity stability and beam size were modelled using the software LCav as shown in Fig. 5.8-5.9. The OPO cavity was designed in a ring resonator in order to reduce loss from optical components per round trip and the folding angle of intracavity beam was set to less than 6 degrees to avoid introducing cavity instabilities. The distance between the intracavity beam focussed by 50-mm lens and the 1-mm-long OPGaP crystal was 50.75 mm which produced a focal spot of 17.4 µm in the OPGaP crystal (Fig. 5.8). The total cavity length was calculated to be 2835 mm in order to match the repetition frequency of the pump laser (Fig. 5.9).

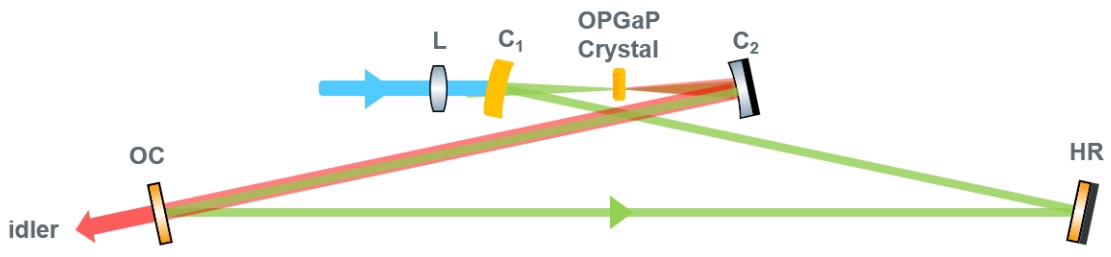

Figure 5.7: Schematic of OPGaP based OPO in ring configuration. L; lens, C_1; ZnSe spherical mirror, C_2; silver spherical mirror, OC; ZnSe output coupler, HR; ZnSe high-reflection mirror.

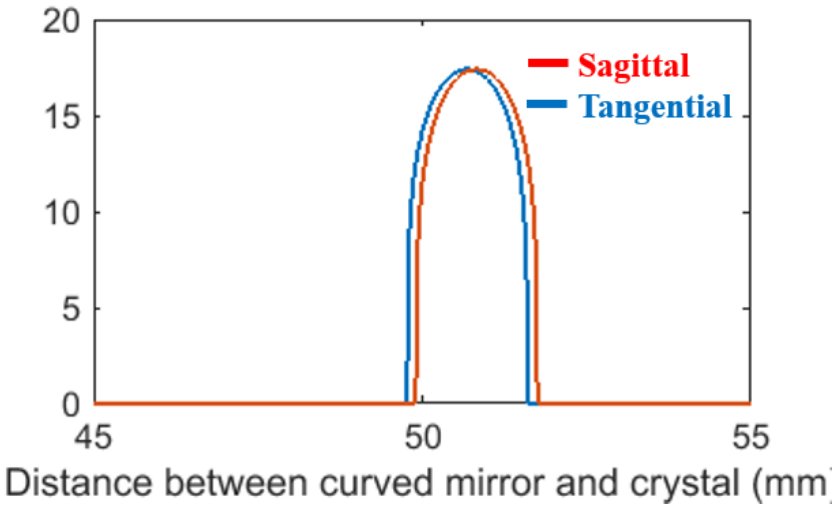

Figure 5.8: LCav model of focal spot size as a function of the curved mirror position for sagittal and tangential planes. LCav model with recent design parameters satisfies mode matching of both planes.

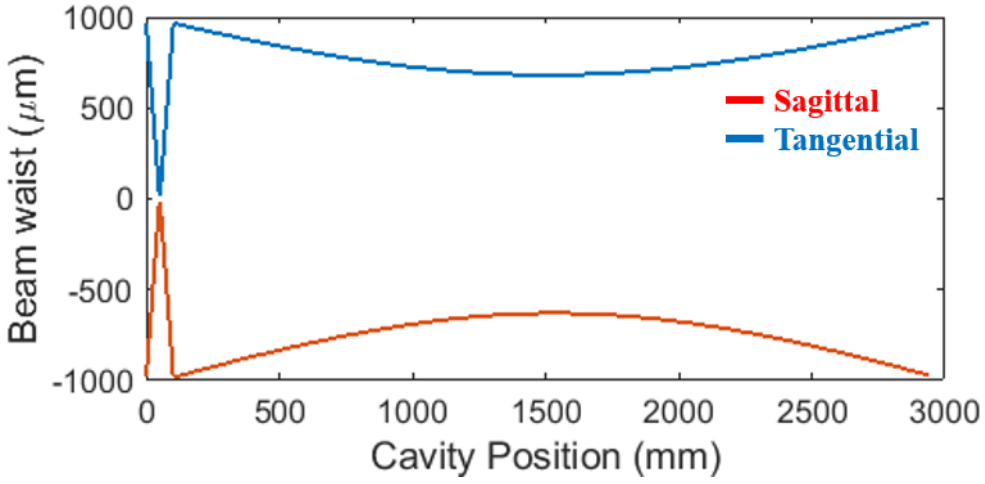

Figure 5.9: Beam profile for OPGaP OPO in ring cavity. The initial point (zero) is described as first curve mirror and the pump resonates at one round trip in the cavity length of approximately 2835 mm.

To agree with the ring cavity model from LCav, two spherical mirrors of which the first was a ZnSe mirror from TwinStar Optics and the second was a silver mirror from Thorlabs were firstly placed with a separation of 101.5 mm. Each OPGaP crystal was secured in a lockable Newport 1-inch optical mount and attached to an XYZ translation stage. Each spherical mirror was a 12.5-mm-diameter, -100 mm radius of curvature high reflector held in a Newport mirror mount that provided a clear edge for beam clearance. The coating of the first spherical mirror was designed to optimize transmission at the pump wavelength of 1041 nm and high reflectivity at the resonant signal wavelength in a range from 1.15–1.35 µm, while the other spherical mirror which was silver coated to enable high reflectivity for all idler wavelengths collimated the idler beam generated from the OP-GaP crystal. This collimated idler beam was outputted from the cavity by

transmission through a plane mirror coated with high transmission for the idler wavelengths (6–8 μm) and high reflectivity for the signal wavelengths (1.15–1.30 μm) on an infrared-transparent ZnSe substrate (Fig. 5.10). The signal output coupler and the high-reflective mirror were mounted in high-stability mirror mounts with differential micrometers to allow the intracavity beam to be walked with accuracy. The signal output coupler was then assembled on a translation stage to synchronise itself with the pump pulses by manual adjustment of the cavity length. The incorporation of a ~1 % signal output coupler, as well as the signal loss from the silver spherical mirror, improved the idler power to be maximized by reducing back-conversion within the OPGaP crystal.

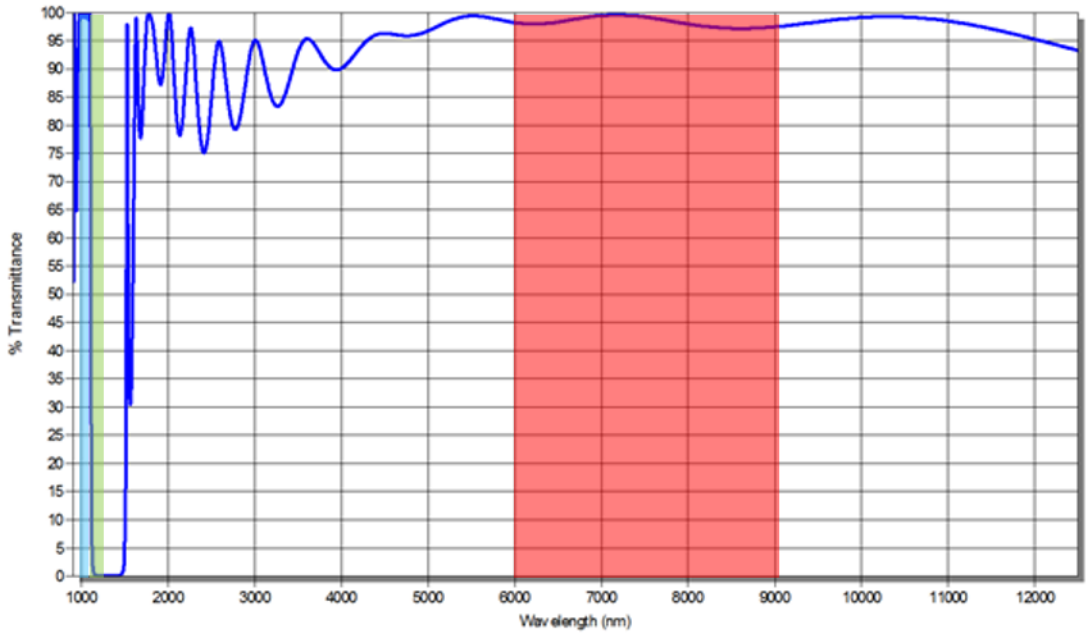

Figure 5.10: Transmission of the optical coating of the infrared transparent ZnSe mirrors from TwinStar between 1 and 12 μm [13]. Blue, green and red show pump, signal and idler windows respectively.

Each OPO was operated in turn with OPGaP crystals with grating periods of 24.5 and 27 μm. In the initial search to find oscillation the OPOs were pumped by bandwidth limited pulses delivered respectively by the two Yb;fibre oscillator/amplifiers that were described in detail in Chapter 3. Once oscillation had been obtained, the pump pulses were slightly chirped by varying the distance between the transmission gratings. As explained in Section 2.2.1, efficient parametric conversion for 1-mm-long OPGaP crystal required a longer pulse duration than bandwidth limited pulses. This arrangement was realized to optimize the idler power for each OPO. The oscillation of each OPO was obtained by moving the output coupler on the translation stage to adjust it to the length calculated by the LCav model. Both OPOs were assembled in the same area of the optical bench and enclosed in a plastic box for stability (Fig. 5.11).

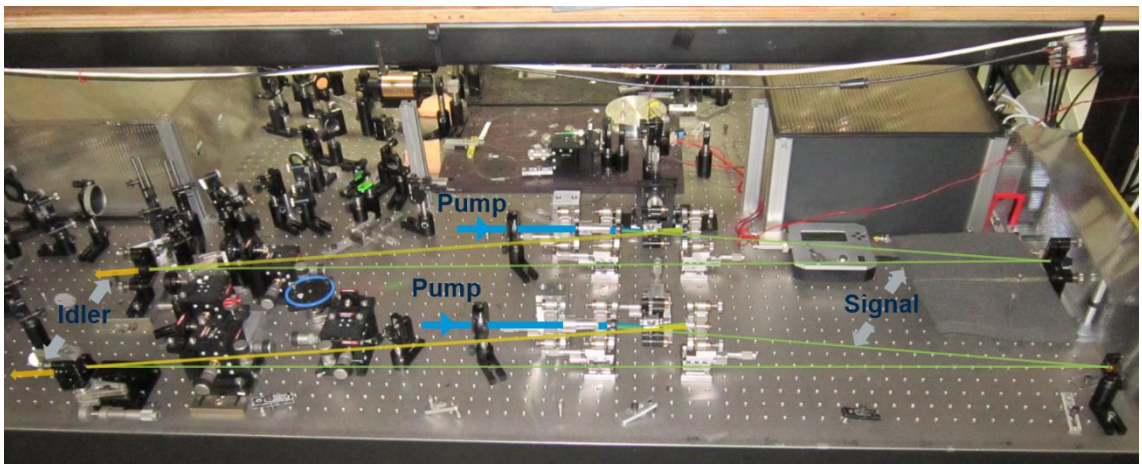

Figure 5.11: Picture of both OPGaP based OPOs in ring cavities. Each OPO was constructed using the same optical components and pumped using the same pump power.

Combined idler spectra of OPOs operated by crystals with different grating periods were measured with a homemade FTIR spectrometer with a resolution of 1.5 cm^{-1} (Fig. 5.12a,c). Idler wavelength at the center of 6.6 μm has structures due to atmospheric water absorption. Reaching oscillation threshold of each OPO for OP-GaP grating periods of 24.5 μm and 27 μm in the ring-cavity format was observed to require approximately 686 and 750 mW respectively (Fig 5.12b,d). The OPGaP crystal with 24.5 μm displayed a 7.7 % conversion efficiency from the pump to the idler, while the OPGaP crystal with 27 μm had 1% efficiency to convert idler photons from pump photons. Such lower conversion efficiency in OP-GaP OPOs compared to PPLN based OPOs is caused by lower quantum efficiency for longer wavelengths. The idler power was optimized by walking the ZnSe end-mirror and output coupler each OPO. Each idler spectrum was matched as the cavity length was tuned slightly. The low intracavity dispersion yielded a short and rapid tuning range, with high sensitivity to alignment and pump cavity length changes.

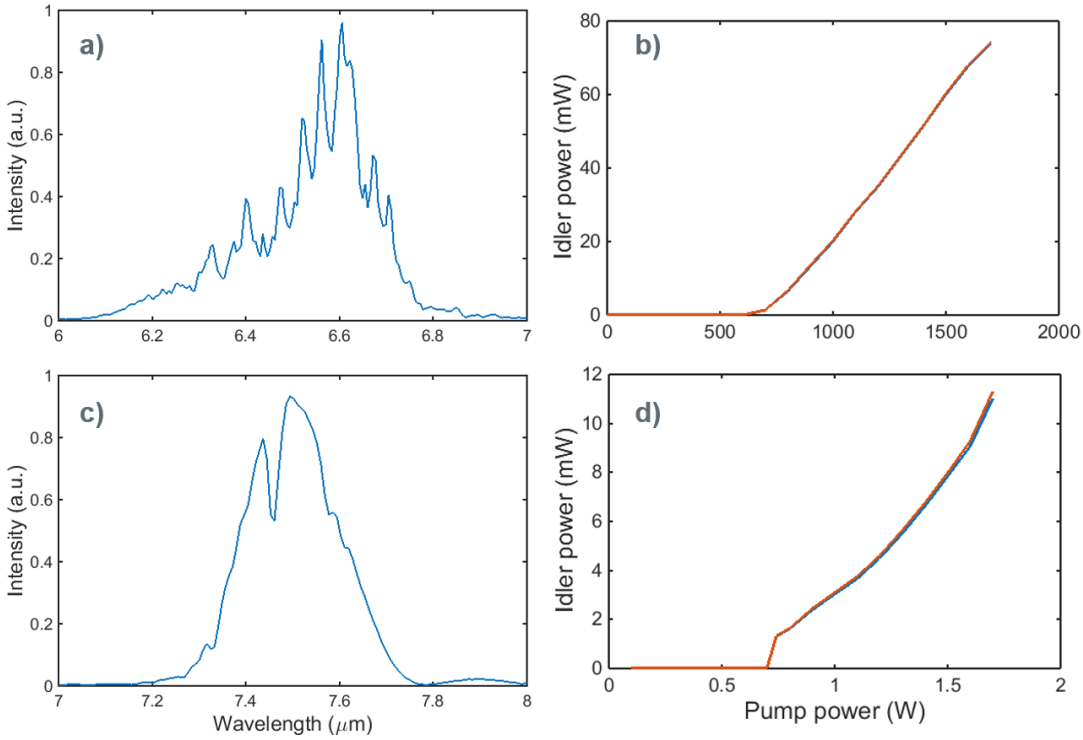

Figure 5.12: Combined idler spectrums of OPO 1 and OPO 2 measured by FTIR spectrometer for independent crystals with grating periods of 24.5 µm **(a)** and 27 µm **(c).** Idler powers of OPO 1 (red) and OPO 2 (blue) pumped with up to 1.8 W by using grating periods of 24.5 µm **(b)** and 27 µm **(d)**. The structures of combined idler spectrum in **(a)** was formed of strong water absorption in that wavelength region specifically.

5.3 Dual-comb spectroscopy in mid-infrared fingerprint region

Dual-comb spectroscopy using OPOs operating in the 3- to 4-µm region was described in Chapter 4. Obtaining high quality spectroscopy has typically required fully-locked combs [14], which provide superior performance to free-running systems, in which the carrier frequency of the DCS interferogram shifts as the comb offsets fluctuate (for example, [15]). In the following section, the results demonstrate that such fluctuations need not present a barrier to high-fidelity dual-comb spectroscopy with OPOs, so long as each interferogram is recorded on a timescale faster than the characteristic decoherence time between the OPOs, i.e. the time in which their comb-mode frequencies change significantly. The DCS system was operated with the previously described OP-GaP OPOs in a free-running mode and with a difference in pulse repetition frequencies (Δf_{REP}) exceeding 1 kHz, implying that high-resolution spectroscopy can be obtained from interferograms acquired in a few tens of microseconds.

The DCS system is presented in Fig. 5.13, and comprised the twin OPGaP OPOs resonant near 1.2 µm and generating idler pulses tunable from 6–8 µm, depending on the grating

period used. Spectroscopy was implemented in a symmetric (homodyne) configuration, in which pulses from both combs interacted with the spectroscopic sample. Each interferogram was recorded, Fourier transformed and provided with a relative optical frequency calibration obtained from concurrent measurements of Δf_{REP} and f_{REP}. An extension of the previously introduced correlation-based co-alignment algorithm (as explained in Chapter 4) was used to correct for the systematic frequency shifts between all the members of a dataset containing more than one hundred consecutively acquired spectra, following which simple averaging provided a single high-quality spectrum.

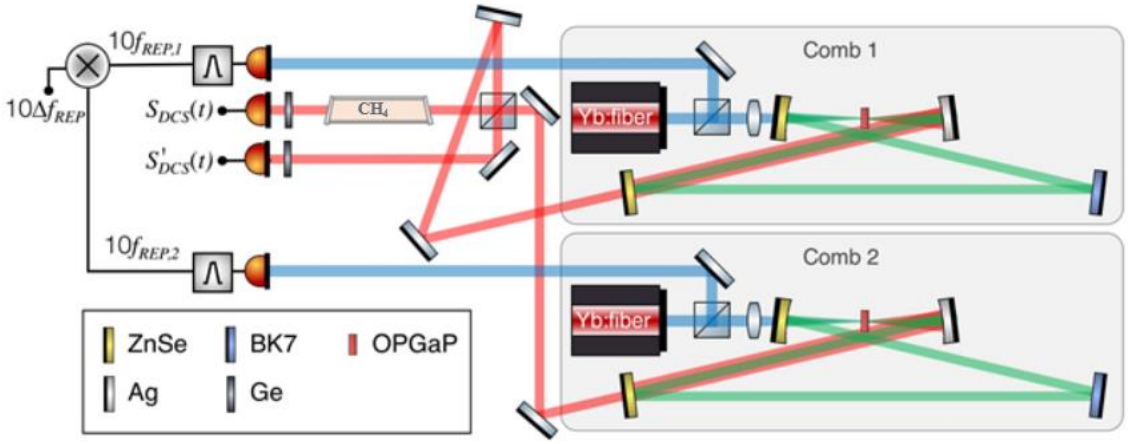

Figure 5.13: The layout of dual-comb spectroscopy using OPGaP optical parametric oscillators.

The OPGaP OPOs were operated on grating periods of 24.5 µm to obtain signal (idler) wavelengths centered around 1.25 µm (6.5 µm) and 27 µm for signal (idler) wavelengths centered near 1.22 µm (7.5 µm). The instantaneous bandwidth of the idler pulses in each case was approximately 500 nm. The idler pulses were extracted from each OPO through the ZnSe plane mirror, as described in Section 5.2. This arrangement yielded well collimated idler beams which were combined at a CaF_2 beamsplitter whose coating was approximately 50% reflecting from 2–8 µm.

Dual-comb interferograms (Fig. 5.14c) were measured from both channels of the beamsplitter using LN_2-cooled HgCdTe detectors with a bandwidth of 50 MHz (Kolmar KMPV11-0.25-J1). Up to 120 interferograms (with this number limited by the buffer size of the acquisition unit) were recorded in a single acquisition (Fig. 5.14a), following which each interferogram was automatically centered (Fig. 5.14c) and Fourier-transformed to yield its radio-frequency spectrum (Fig. 5.14b). Sample-gas spectroscopy, in this case methane, was conducted by inserting a 20-cm gas cell before one of the

detectors, while background spectroscopy, in this case water vapor, was carried out with the other detector. Both interferograms were digitized at 200 MHz and acquired on two channels of a 14-bit-resolution USB oscilloscope (TiePie HS5). A third channel recorded a signal at $10\Delta f_{REP}$, which was obtained by isolating the tenth harmonic of each pump laser's repetition frequency (RF) using a narrowband 1-GHz bandpass filter, then differencing the two repetition-frequency harmonics using a RF mixer followed by a low-pass filter. A zero-crossings algorithm [13] implemented in Matlab accurately extracted Δf_{REP} for each interferogram, following which the corresponding RF spectrum was then scaled to the optical domain by multiplying its frequency sampling interval by a factor of $f_{REP} / \Delta f_{REP}$. Finally, each spectrum obtained in this way was recorded as one row in a matrix, in preparation for subsequent spectral co-alignment and averaging with other spectra.

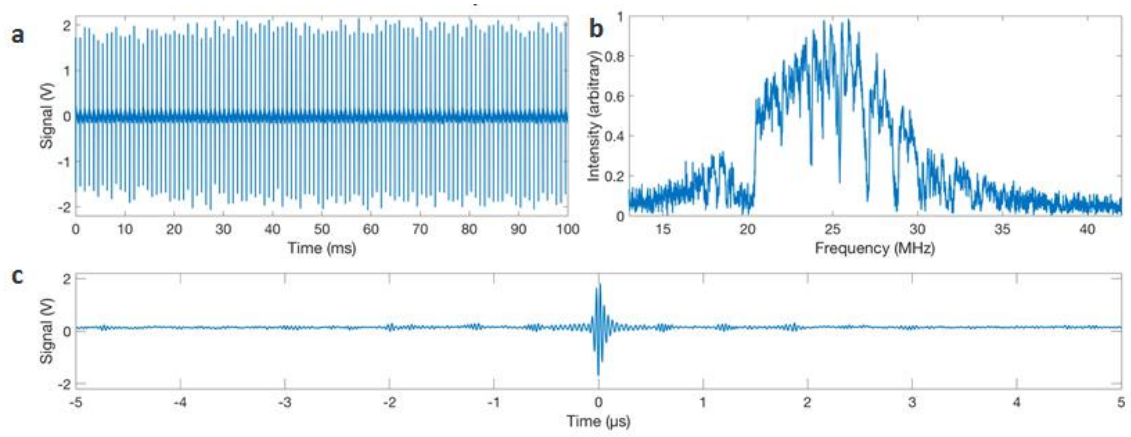

Figure 5.14: Example DCS dataset, comprising >100 interferograms acquired at ~1.1 kHz over 100 ms. (a) The apparent intensity fluctuations are due to the different carrier-envelope phases of each interferogram. (b) Detail of a single interferogram and (c) its Fourier transform.

5.3.1 *Spectral co-alignment and averaging*

Fluctuations in f_{CEO} for each of the two combs occur on millisecond timescales (the mutual decoherence times of the combs), resulting in small variations in the RF carrier frequency of each dual-comb interferogram. So long as each interferogram is recorded in a time much faster than this decoherence time then the spectral information remains intact but is simply shifted to an alternative center frequency. Spectral averaging can therefore be performed to improve the signal:noise ratio of the data, but before this can be done, each spectrum must be accurately co-aligned with every other spectrum. This was implemented using a full-spectrum cross-correlation technique and the relative shifts between any pair of spectra was calculated as explained in Section 4.3.1.

These shifts, including self-comparisons ($i = j$), are stored in an $N \times N$ matrix, illustrated for a representative 114-sample dataset in Fig. 5.15a. As an example, two typical spectra are shown in Fig. 5.15b. The shift of each spectrum relative to the average position is computed by summing its mutual shifts and normalizing the result by N. We then co-align all of the spectra to the member of the set which has the lowest deviation from the average position and perform an average. The result of co-aligning just two such spectra is shown in Fig. 5.15c, illustrating the precision available from this technique. Finally, the average spectrum is shifted so that its center position coincides with the exact average position for the entire dataset.

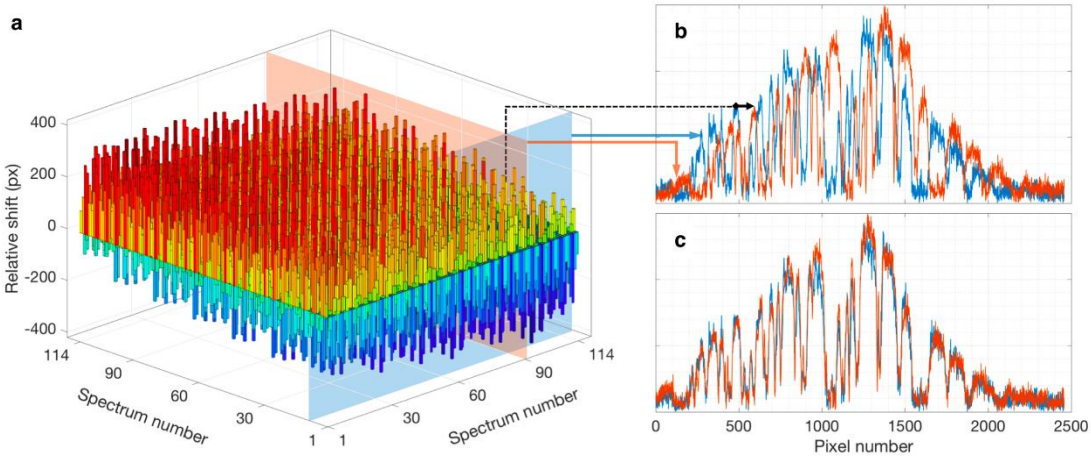

Figure 5.15: Cross-correlation protocol for co-aligning multiple DCS spectra. (a) Each member of a dataset of >100 spectra is cross-correlated individually with every other member to obtain a shift, expressed as a number of pixels and which can be visualized as an $N \times N$ matrix, where N is the original number of DCS spectra. These shifts can be used to co-align the entire dataset, with (b) and (c) illustrating, respectively, an example of two such spectra before and after co-alignment.

5.3.2 *Spectroscopic measurements of ambient water vapor*

Operating on a grating period of 27 µm, the OPOs produced pulses with spectra spanning 1280–1370 cm^{-1} and which travelled 2.5 m in air from the OPGaP crystals to the detector. Water vapour absorption is relatively weak in this region but can still be clearly seen in the spectrum shown in Fig. 5.16a. Envelope removal and fitting to the HITRAN 2012 database which will be explained in Section 5.3.4 in detail yielded the transmission spectrum in Fig. 5.16b. The regular modulations evident in the residuals of the trace (Fig. 5.16c, blue) are étalon effects which can be directly traced to parasitic reflections in the OPGaP crystals, a Ge filter and the ZnSe idler output couplers in the OPO cavities. The transmission spectrum can be corrected by removing these étalon effects, and doing this resulted in excellent agreement with HITRAN at 0.256-cm^{-1} resolution, with features and line-shapes becoming clearly resolved (Fig. 5.14d). The remaining residual (Fig. 5.16c, green) shows a standard deviation of 1.3%, implying a noise-equivalent absorption of

0.0041 $Hz^{-1/2}$. The fit to HITRAN allows quantitative determination of the water vapor concentration, yielding a mole-fraction concentration of 0.54%, consistent with our lab conditions.

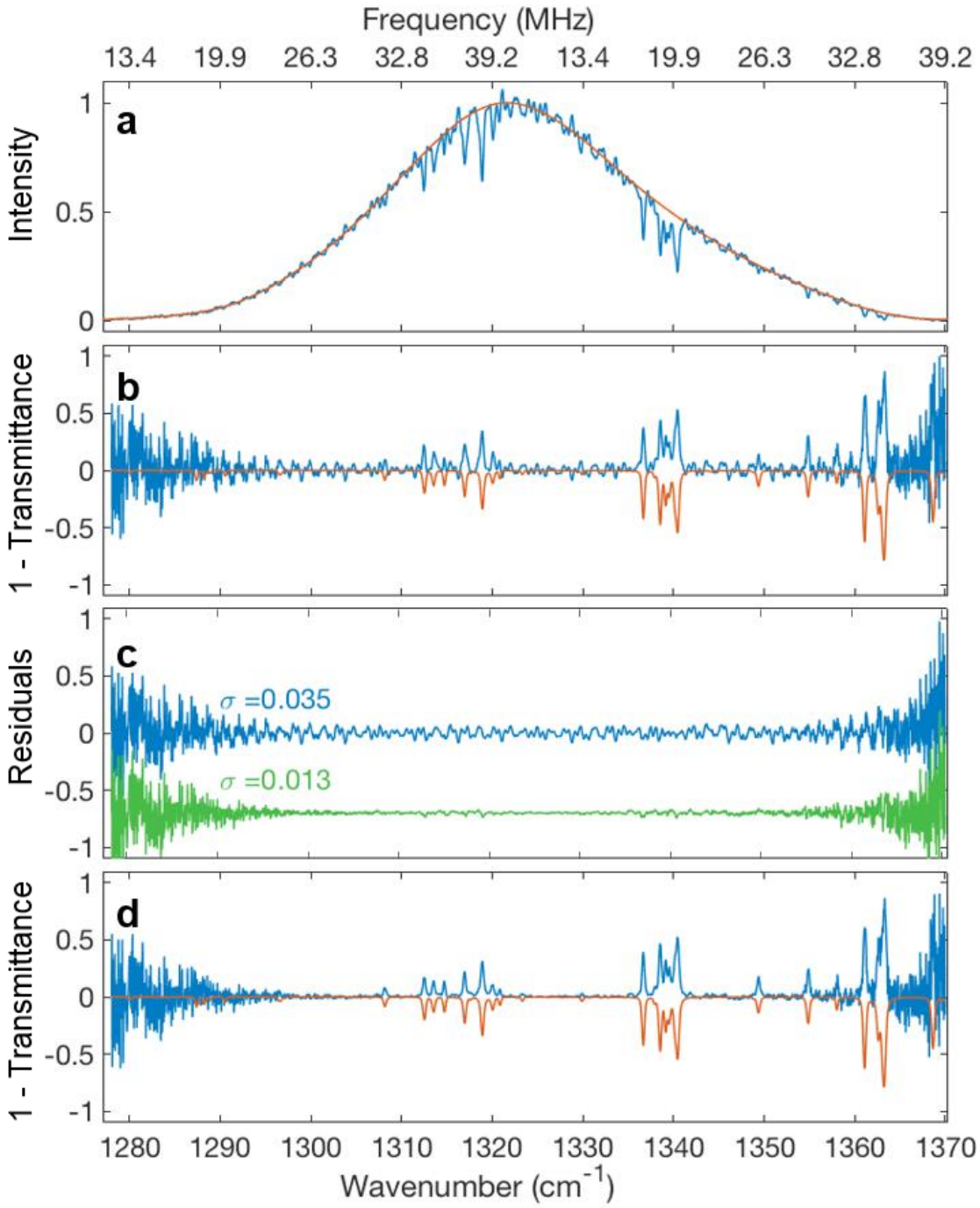

Figure 5.16: Dual-comb spectroscopy of ambient air in the 7-to 8-μm region. **(a)** Averaged dual-comb spectra (blue) and fitted envelope (red); **(b)** Extracted transmittance from the dual-comb data and comparison with a HITRAN 2012 fit for water vapor, from which the spectroscopy resolution and gas concentration was obtained. **(c)** Residuals of the original fit (blue) and after étalon removal (green,vertically displaced by -0.6 for clarity). **(d)** Transmittances after étalon removal, showing excellent agreement with the HITRAN 2012 lineshapes, magnitudes and positions.

With a grating period of 24.5 µm the OPO produced shorter idler wavelengths which spanned the 1490–1590-cm^{-1} spectral region. Performing an identical analysis gave the results in Fig. 5.17a which again show excellent agreement with the HITRAN simulation in this region (Fig. 5.17b, d). The impact of étalons is much less severe in this band because of the better performance of the long-wave IR anti-reflection coatings on our optics at these wavelengths. The fitting resolution in this case is 0.298-cm^{-1} and the mole-fraction water-vapor concentration was determined as 0.77%. The difference in ambient water-vapor concentration compared to the earlier result is not unexpected, since the lab humidity varies with time and with local atmospheric conditions. After étalon-fringe removal the residual (Fig. 5.17c, green) shows a standard deviation of 2.4%, giving a noise-equivalent absorption of 0.0076 $Hz^{-1/2}$.

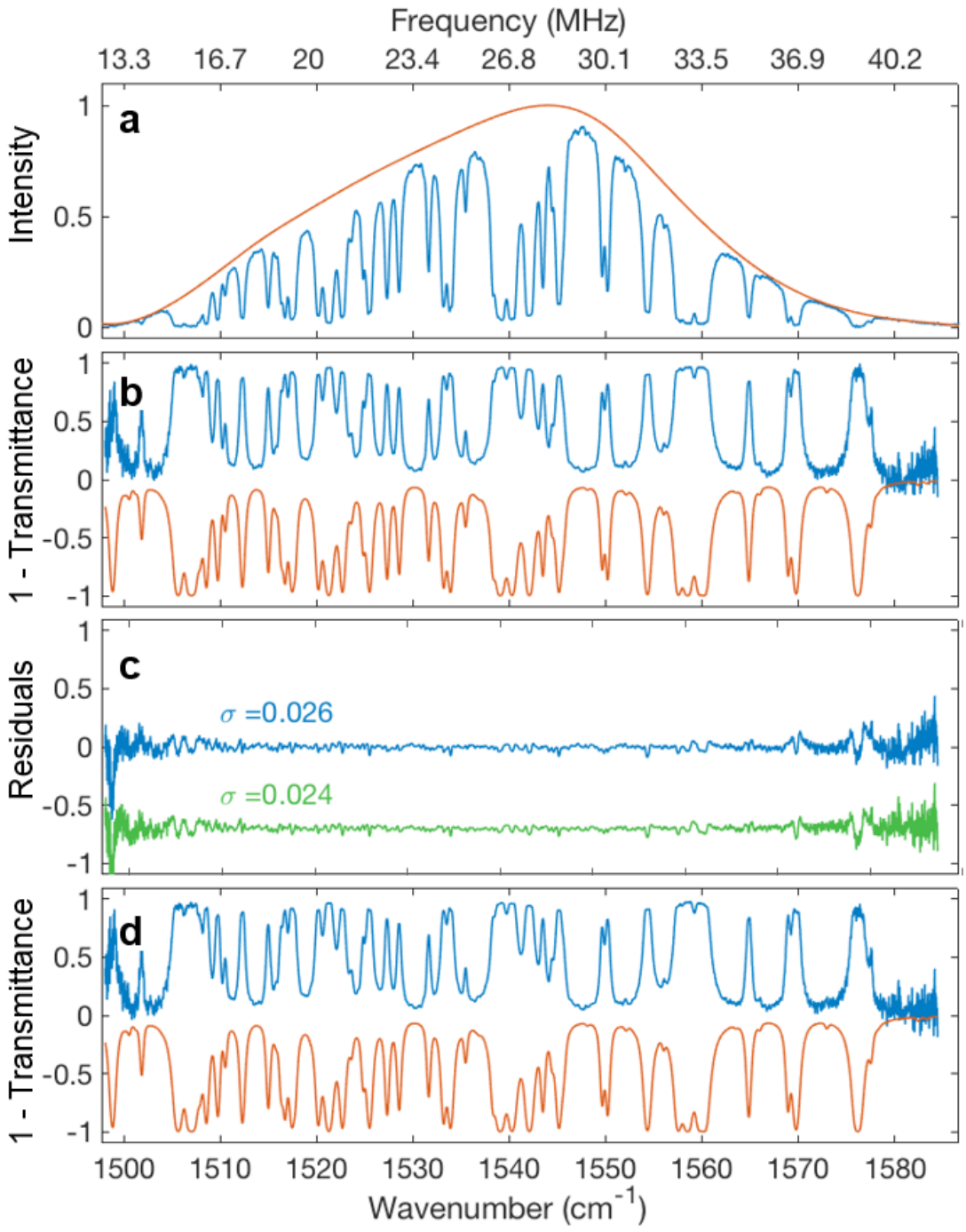

Figure 5.17: Dual-comb spectroscopy of ambient air in the 6-to7-μm region. The figure structure and labelling follow those given in Fig. 5.16.

5.3.3 *Spectroscopic measurement of methane with ambient air*

With the OPO operating in the 1280–1370-cm^{-1} band, dual-comb interferograms were acquired after introducing into both OPO beams a 20-cm gas cell containing a synthetic air mixture with nominally 2% methane. Processing the interferograms as previously described yielded the results in Fig. 5.18a, b. As the distance from the OPGaP crystals to the detector remained the same as before, a similar water-vapor contribution to the spectrum was both expected and observed. After étalon removal (Fig. 5.18c, green) the

standard deviation of the residuals of 3.5% implied a noise-equivalent absorption for methane at this concentration of 0.011 $Hz^{-1/2}$. The fitting procedure simultaneously and independently fitted for methane and water-vapor concentrations and yielded parameters of 0.68% water vapor and 2.17% methane, consistent with previous ambient air measurements and with the original filling specification of the methane gas cell. Excellent agreement was obtained (Fig. 5.18d) with the HITRAN data with a fitting resolution of 0.314 cm^{-1}.

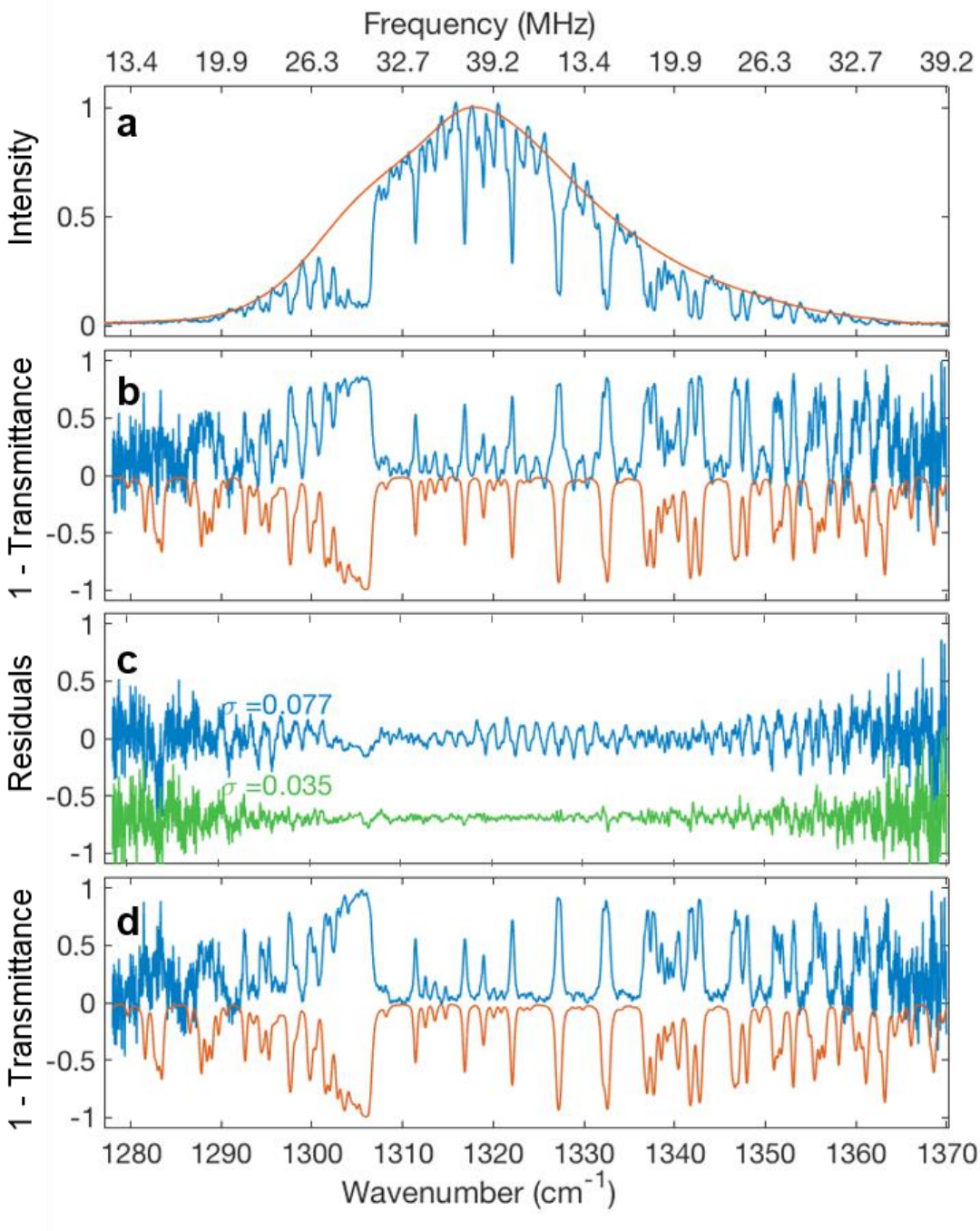

Figure 5.18: Dual-comb spectroscopy of a 20-cm methane cell in ambient air in the 7-to 8-μm region. The figure structure and labelling follow those given in Fig. 5.16, with the exception that the fitting procedure treated the water vapor and methane gas concentrations as independent variables.

5.3.4 *Hitran fitting and etalon removal from spectroscopic measurements*

The HITRAN 2012 database [16] and an online spectral simulation tool [17] provide line-by-line spectroscopic parameters of a wide range of atmospheric gases, enabling the generation of high resolution absorbance spectra for water vapor and methane, which can be transformed into transmittance spectra using the Beer-Lambert law. These spectra were convolved with a Gaussian instrument response function of adjustable full width at half-maximum (FWHM) to simulate the limiting resolution of the experimental spectra. A multi-parameter fit was carried out using the Matlab Nelder-Mead simplex algorithm [20], in which the fitting parameters were the mole-fraction concentrations of water vapor and methane, a rigid frequency shift, the FWHM of the Gaussian instrument response function and 15–20 floating points which define the smooth envelope of the incident OPO spectrum via a spline function. The following parameters were fixed: temperature, at 300 K; pressure, at 1 atm; path lengths at 20 cm for methane and 2.3 m (2.5 m) for ambient water vapor with (without) the methane cell present. In Fig. 5.16a - 5.18a the fitted envelope function is shown in red and is compared with the average DCS spectrum, which is shown in blue. The fitting results are shown in Fig. 5.16b- 5.18b and the corresponding residuals appear in the blue traces in Fig. 5.16c-5.18c. In the 7–8-μm band, parasitic étalon resonances occurring in the OPGaP crystals, a Ge filter and the ZnSe output couplers are revealed as sinusoidal oscillations in the residuals. The use of a fitting procedure which was both broadband and fits many parameters simultaneously is found to be extremely robust in the presence of these étalon effects. This is demonstrated by the immediate improvement in the fitting error after removing the étalon effects, as shown in Fig. 5.16d-5.18d and the accompanying residuals (green) in Fig. 5.16c-5.18c. Line shapes and features which are distorted or hidden before étalon-fringe removal are clearly resolved after the procedure is performed.

Étalon-fringe removal was implemented by Fourier transforming the original residuals to identify the principal frequencies present. As illustrated in Fig. 5.19 - which takes as an example, residuals from the water-vapor measurement of Fig. 5.16c - these frequencies can be presented on a scale calibrated in terms of the étalon optical thickness (nL), showing the four strongest étalons to have optical thicknesses of 3.18 mm, 8.36 mm, 0.45 mm and 7.23 mm. The first is attributed to the 1-mm OPGaP crystals (n = 3.1780); the second is due to a 2-mm Ge filter (n = 4.0058); the fourth is from the 3-mm ZnSe OPO cavity mirrors (n = 2.4087). The exact origin of the third etalon is not certain but is very likely attributable to a thin ZnSe window in the HgCdTe detector. Using a peak

detection algorithm in Matlab, the principal étalon resonances can be isolated, allowing their contributions to be subtracted from the OPO transmission spectrum. Once this was done, the agreement with the HITRAN simulation was significantly improved, as shown in Fig. 5.16d-5.18d.

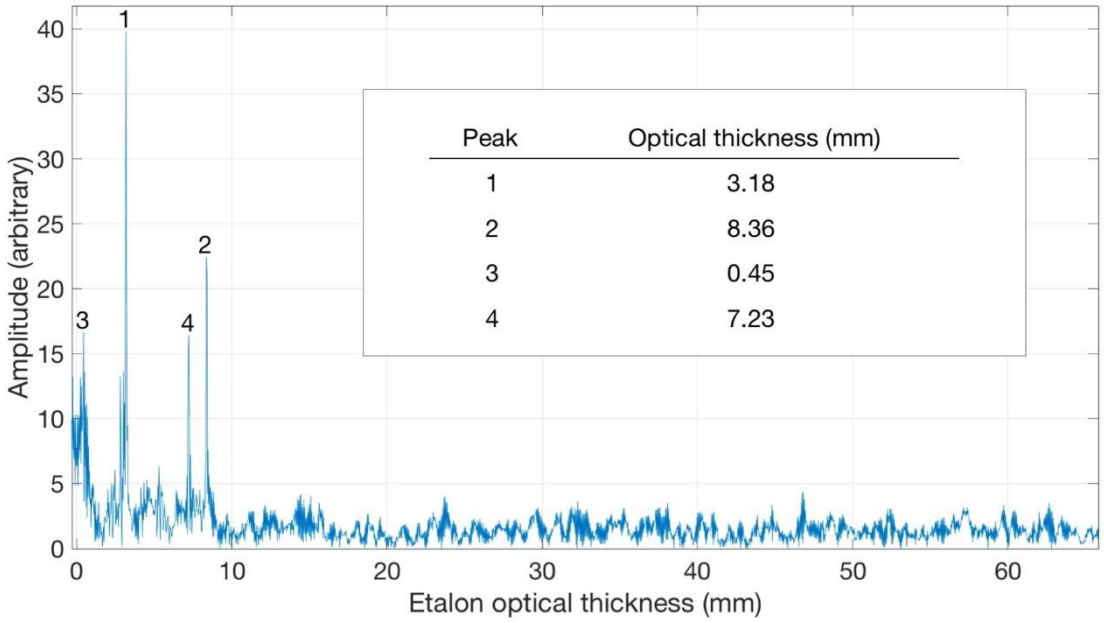

Figure 5.19: Example of étalon removal protocol. Residuals obtained from the original full-spectrum fitting procedure (Fig. 5.14c-5.16c) are Fourier-transformed and the principal frequencies expressed in terms of étalon optical thickness. Peaks 1–4 are identified, respectively, with: the 1-mm OPGaP crystals (n = 3.1780); a 2-mm Ge filter (n = 4.0058); the 3-mm ZnSe OPO cavity mirrors (n = 2.4087); a thin ZnSe window in the HgCdTe detector.

5.4 Discussion

The first demonstrations of combined broadband and high-resolution spectroscopy in the spectral fingerprint region from 6–8 μm were presented in this chapter. The results shown here represent among the highest quality dual-comb data obtained in the mid-infrared using unreferenced free-running femtosecond lasers, demonstrated by excellent agreement between the HITRAN 2012 database and the positions, relative magnitudes and shapes of the experimentally measured absorption lines. This performance has been achieved by employing a novel line-shape-preserving averaging protocol, which we demonstrated for approximately 115 spectra but that in principle could be applied to a much larger dataset without loss of fidelity. Unlike other line-by-line fitting approaches, the availability of a single broadband spectrum made it possible to conduct a full-spectrum multi-parameter fit to the HITRAN database, which the results show is robust in the presence of noise and of étalon effects, allowing these to be eliminated by post-processing.

The interferogram time window used for data processing was 40 μs, implying a limiting resolution of 0.076 cm^{-1}, a factor of 3-4 lower than the experimentally observed resolutions of 0.256-0.314 cm^{-1}. This difference is presumably caused by decoherence between the combs that occurs on the timescale of the interferogram window. Acquiring interferograms in a shorter time by operating the system at a higher value of Δf_{REP} should mitigate this problem, although steps would need to be taken to limit the optical bandwidth in order to avoid aliasing as discussed in Chapter 4.

5.5 Conclusion

Dual-comb spectroscopy (DCS) in the fingerprint region has been demonstrated across nearly 100 cm^{-1} and in 100 milliseconds acquisition time, which extends the state-of-the-art by representing the first example of simultaneously achieving high resolution and broadband DCS in the spectral fingerprint region. The use of OPGaP OPOs is important because it represents a scalable and intrinsically tunable approach, with the potential for a single OPO with suitably chosen quasi-phasematched gratings to reach as far as 13 μm and power levels of hundreds of milliwatts with readily available 1-μm pump lasers. This capability, together with the naturally high beam quality of such OPOs makes free-space implementations immediately practical and already offers performance which far surpasses that of previously reported kHz-rate supercontinuum sources.

5.6 References

1. L. A. Eyres, P. J. Tourreau, T. J. Pinguet, C. B. Ebert, J. S. Harris, M. M. Fejer, B. Gerard, and E. Lallier, "Quasi-phasematched Frequency Conversion in Thick All-epitaxial, Orientation-patterned GaAs Films", Advanced Solid State Lasers, H. Injeyan, U. Keller, and C. Marshall, eds. (Optical Society of America, 2000), paper TuA2.

2. Schunemann, P., Mohnkern, L., Vera, A., Yang, X., Lin, A., Harris, J., Tassev, V. and Snure M., "All-epitaxial growth of orientation-patterned gallium phosphide (OPGaP)," Lasers, Sources, and Related Photonic Devices Technical Digest OSA, ITh5B.5.pdf 1-3 (2012).

3. Luke Maidment, Peter G. Schunemann, and Derryck T. Reid, "Molecular fingerprint-region spectroscopy from 5 to 12 μm using an orientation-patterned gallium phosphide optical parametric oscillator," Opt. Lett. 41, 4261-4264 (2016).

4. http://www.ioffe.ru/SVA/NSM/Semicond/GaP/index.html

5. L. A. Pomeranz, P. G. Schunemann, D. J. Magarrell, J. C. McCarthy, K. T. Zawilski, and D. E. Zelmon, "1-μm-pumped OPO based on orientation-patterned GaP," Proc. SPIE 9347, 93470K (2015).

6. P. G. Schunemann, L. A. Pomeranz, and D. J. Magarrell, "First OPO Based on Orientation-Patterned Gallium Phosphide (OP-GaP)," in *CLEO: 2015*, OSA Technical Digest (online) (Optical Society of America, 2015), paper SW3O.1.

7. https://refractiveindex.info/?shelf=main&book=GaP&page=Bond.

8. D. F. Parsons and P. D. Coleman, "Far Infrared Optical Constants of Gallium Phosphide," Appl. Opt. 10, 1683_1-1685 (1971).

9. Hurlbut, W., Lee, Y., Vodopyanov, K., Kuo, P. and Fejer, M., "Multi- photon absorption and nonlinear refraction of GaAs in the mid- infrared," Opt. Lett. 32, 668-670 (2007).

10. G. Schunemann, L. A. Pomeranz, Y. E. Young, L. Mohnkern and A. Vera, "Recent advances in all-epitaxial growth and properties of orientation-patterned gallium arsenide (OP-GaAs)," *2009 Conference on Lasers and Electro-Optics and 2009 Conference on Quantum electronics and Laser Science Conference*, Baltimore, MD (2009)

11. C. B. Ebert, L. A. Eyres, M. M. Fejer, and J. S. Harris, "MBE growth of antiphase GaAs films using GaAs/Ge/GaAs heteroepitaxy", J. Cryst. Growth 201, 187 (1999).

12. K. Termkoa, S. Vangala, W. Goodhue, R. Peterson, R. Bedford, V. Tassev, C. Lynch, and D. Bliss, "Orientation-patterned GaP using wafer fusion technique", Opt. Materials 34, 30-35 (2011).

13. Twinstar Optics, Coatings and Crystal; http://www.twinstaroptics.com.

14. E. Baumann, F. R. Giorgetta, W. C. Swann, A. M. Zolot, I. Coddington, and N. R. Newbury, "Spectroscopy of the methane ν3 band with an accurate midinfrared coherent dual-comb spectrometer," Phys. Rev. A 84, 062513 (2011).

15. A. Schliesser, M. Brehm, F. Keilmann, and D. W. van der Weide, "Frequency-comb infrared spectrometer for rapid, remote chemical sensing," Opt. Express 13, 9029-9038 (2005).

16. L.S. Rothman, I.E. Gordon, Y. Babikov, A. Barbe, D. Chris Benner, P.F. Bernath, M. Birk, L. Bizzocchi, V. Boudon, L.R. Brown, A. Campargue, K. Chance, E.A. Cohen, L.H. Coudert, V.M. Devi, B.J. Drouin, A. Fayt, J.-M. Flaud, R.R. Gamache, J.J. Harrison, J.-M. Hartmann, C. Hill, J.T. Hodges, D. Jacquemart, A. Jolly, J. Lamouroux, R.J. Le Roy, G. Li, D.A. Long, O.M. Lyulin, C.J. Mackie, S.T. Massie, S. Mikhailenko, H.S.P. Müller, O.V. Naumenko, A.V. Nikitin, J. Orphal, V. Perevalov, A. Perrin, E.R. Polovtseva, C. Richard, M.A.H. Smith, E. Starikova, K. Sung, S. Tashkun, J. Tennyson, G.C. Toon, V.G. Tyuterev, G. Wagner, The HITRAN2012 molecular spectroscopic database, J. Quant. Spectrosc. Radiat. Transf. 130, 4-50 (2013).

17. http://spectraplot.com.

18. Gander, Walter, Martin J. Gander, and Felix Kwok. *Scientific computing-An introduction using Maple and MATLAB*. Vol. 11. Springer Science & Business, 2014.

Chapter 6 – Conclusions and Future Perspectives

In this thesis, advances of OPOs applied to DCS have been highlighted in the context of several different requirements. The first challenge was to develop a rapid, robust instrument to address the requirements of molecular spectroscopy in the mid-infrared. For this wavelength region, OPOs are easily accessible with sufficient maturity to provide broad spectral bandwidths comb performance [1]. The design aspects of OPOs here were optimised in order to reduce the constraints, which typically arise from thermal variations, mechanical vibrations etc whilst avoiding excessive complexity in the design criteria. A second requirement was to implement this system for infrared spectroscopy to investigate its feasibility and limitations. As mentioned frequently, the mid-infrared region provides an opportunity to explore DCS for several molecules, including greenhouse and hazardous gases in particular. A major goal for spectroscopic purposes was to focus on gas absorption spectroscopy, for which the methane was selected as a candidate gas for its simple structural characteristics.

In the first part (Chapter 3) of this doctoral thesis, the design of OPO-based DCS was initialized by employing two identical Yb:fibre lasers to form a composite pump source for two prospective MgO:PPLN based OPOs designed to operate independently. Two identical and independent ANDi Yb:fibre oscillators were established with chirped pulses at repetition rate of 102 MHz and then amplified up to 2.5 W average power in two separate cladding-pumped polarization-maintaining Yb:fiber amplifiers. The naturally, chirped pulse output of each oscillator meant that it was not necessary to stretch the pulses in order to reduce pulse distortion or prevent destruction of the gain medium of the fibre amplifier. These chirped pulses were generated with durations of 3.9 ps and −3 dB bandwidths of 18 nm. The repetition frequency of each laser was controlled with a PZT assembled inside each oscillator cavity and its control unit was designedimplemented through the technique of direct digital synthesis to generate a low-noise phase-locked loop for repetition frequency stabilization. According to the first demonstration of OPO based DCS, an OPO with a long nonlinear crystal had worked well to efficiently transfer the pump spectral bandwidth into the mid-IR idler output and was passively stable against OPO cavity instabilities [2]. As a consequence of that, each OPO was built in a linear cavity configuration, with a 20-mm-long-MgO:PPLN crystal. Both identical OPOs generated idler pulses at 3.3 μm and with a spectral bandwidth of 180 nm specifically optimised for methane spectroscopy. Two separate nonlinear interferometers were

constructed to determine the offset frequencies of both OPOs independently. Relative intensity noise measurements showed that the OPOs were comparable in performance but that CEO stabilization did not improve their amplitude stabilization as had been reported for OPOs using shorter PPLN crystals [3]. This analysis showed improvements from stabilizing the systems, but the stability performance of the free-running systems was found to be only slightly poorer, even without mechanical noise arising during phase-locked loop in the stabilization. As expected from OPOs designed with high cavity dispersion, both OPOs were inherently stable in the short term.

Chapter 4 presented mid-infrared dual-comb spectroscopy using two independent OPOs, whose high degree of passive stability provides an accessible means of implementing dual-comb mid-infrared spectroscopy with high signal:noise ratio, broad bandwidth and sub-cm^{-1} resolution necessary to resolve gas-phase ro-vibrational absorption lines. The spectroscopic measurements were performed with free-running OPOs and idler f_{CEO}-stabilized OPOs. For a measurement with an offset stabilized system, the data quality was limited and averaging was not applicable in order to improve signal:noise in the stabilized system, where the interferograms in the data set were not coherent. In situations where dual-comb spectroscopy is performed with a fully stabilized system using phase-locked loops (PLL), it has been noted that interferograms can be distorted due to servo bumps and capture limits in the PLL electronics. Data acquired under standard laboratory conditions with stabilization activated presented the same performance as was obtained using only the free-running OPOs. Noise reduction using averaging of multiple spectra was achieved in the free-running system by automatically re-centering the data around the median wavelength value. Cross-correlations between spectra obtained by Fourier transforming individual interferograms were used to determine the relative shifts between spectra making it possible to align each spectrum to the member of the set which had the lowest deviation from the median position and then perform an average. This technique enabled alignment of all the recorded spectra to an absolute wavelength scale with sub-nm precision and after averaging improved the signal:noise ratio by ×5. After background subtraction, excellent agreement with the Hitran absorbance simulation was obtained. The calibration approach benefits from operating at a high repetition frequency difference. It should be possible to improve the precision of the calibration further by recording a very high harmonic of Δf_{REP}, by heterodyning high harmonics of the repetition frequencies.

Finally, in Chapter 5, DCS was extended to the 6–8-μm wavelength band by implementing dual OP-GaP based OPOs. Each OPO was designed in a ring cavity configuration and pumped with nearly fully dechirped pulses reflecting the use here of only a 1-mm-long crystal. Unlike the MgO:PPLN OPOs, the OP-GaP based OPOs had a relatively high oscillation threshold. The spectroscopic performance with this system was investigated across the 6-8 μm region, where methane has a strong ro-vibrational absorption structure as well as there being strong atmospheric water-vapour absorption. A novel line-shape-preserving averaging protocol was applied and spectroscopy results from methane and water vapour were presented for approximately 115 spectra. In principle, this protocol could be applied to a much larger dataset without loss of fidelity. Unlike other line-by-line fitting approaches, the availability of a single broadband spectrum made it possible to conduct a full-spectrum multi-parameter fit to the HITRAN database, which our results showed was robust in the presence of noise and of étalon effects, allowing these to be eliminated by post-processing. The robustness of the fit in the presence of étalon effects was confirmed by re-running the fit after removing the étalon fringes, which led to no significant change in the best-fit parameters. However, the spectral resolutions were limited to around 0.2 cm^{-1} by decoherence between the combs that occured on the timescale of the interferogram window. The decoherence of comb modes can be reduced by acquiring interferograms in a shorter time provided that the optical bandwidth can be limited.

The performance of OPO based DCS must be improved to achieve sufficiently coherent comb modes for very high resolution spectroscopy. Despite good stability performance of individual ANDi fibre lasers, the comb-mode instabilities of these pump lasers may present a problem for OPOs. Because OPOs have separate cavities and comb mode decoherence in DCS arises from intracavity instabilities, this means that comb mode coherence is related to four degrees of freedom. Firstly, this problem can be solved by stabilizing the pump offset frequency. In other words, the OPO is pumped by a laser comb and the OPO follows the same fluctuations as the pump source. Such an approach could provide full coherence between the pump, signal and idler pulses [4]. As an alternative to high performance stabilization, direct phase correction techniques have already been applied to DCS in the near-infrared [5-7]. The challenge in the mid-infrared to approach real-time correction is the limited availability of stable narrow-linewidth lasers. Since the significant development of QCL technology, commercially available distributed feedback QCLs can deliver up to 11 μm with a spectral bandwidth of less than 1 nm. Such narrow-

linewidth mid-infrared lasers might be used to sample frequency fluctuations, allowing such fluctuations to then be compensated directly by electronic signal processing [5] or referenced to correct the acquired data continously [6,7].

The implications of extending DCS into the spectral fingerprint band, and in a manner not requiring stabilization of either f_{REP} or f_{CEO}, are significant. In addition to the organic fingerprints, many pollutant gases also exhibit high absorption cross sections in this region (e.g. NH_3, CH_4, N_2O), meaning that sensitive and quantitative free-space detection for the purposes of environmental monitoring is possible, without the need for complex phase-locked systems. The potential of DCS for multi-kHz data rates means that chemical reactions could be monitored directly in real time, and the specificity of the fingerprint region to molecular isomers could provide new insights into the dynamics of chemical bonding [8]. Similar advantages apply to nano-Fourier transform infrared spectroscopy (FTIR) [9], in which scanning near-field optical microscopy is implemented with mid-IR illumination of a metallic tip, enabling nanoscale chemical mapping of polymer blends, organic fibers, and biomedical tissue. Dual-comb illumination could dramatically increase the acquisition rate of nano-FTIR spectra, potentially even enabling a form of nanoscale hyperspectral imaging.

References

1. Y. Kobayashi, K. Torizuka, A. Marandi, R. L. Byer, R. A. McCracken, Z. Zhang, and D. T. Reid, “Femtosecond optical parametric oscillator frequency combs”, *Journal of Optics*, *17*(9), 094010 (2015).

2. Zhaowei Zhang, Tom Gardiner, and Derryck T. Reid, "Mid-infrared dual-comb spectroscopy with an optical parametric oscillator," Opt. Lett. 38, 3148-3150 (2013)

3. Zhaowei Zhang, Xiaohui Fang, Tom Gardiner, and Derryck T. Reid, "High-power asynchronous midinfrared optical parametric oscillator frequency combs," Opt. Lett.38, 2077-2079 (2013).

4. J. Sun and D. T. Reid, "Coherent ultrafast pulse synthesis between an optical parametric oscillator and a laser," Opt. Lett. 34, 854-856 (2009)

5. T. Ideguchi, A. Poisson, G. Guelachvili, N. Picque, T. W. Hänsch, "Adaptive real-time dual-comb spectroscopy." *Nature communications* 5 (2014).

6. P. Giaccari, J. Deschênes, P. Saucier, J. Genest, and P. Tremblay, "Active Fourier-transform spectroscopy combining the direct RF beating of two fiber-based mode-locked lasers with a novel referencing method," Opt. Express 16, 4347-4365 (2008).

7. J. Roy, J. Deschênes, S. Potvin, and J. Genest, "Continuous real-time correction and averaging for frequency comb interferometry," Opt. Express 20, 21932-21939 (2012).

8. I. Marziano, D. C. A. Sharp, P. J. Dunn and P. A. Hailey, "On-Line Mid-IR Spectroscopy as a Real-Time Approach in Monitoring Hydrogenation Reactions," Org. Process Res. Dev. **4**, 357–361 (2000).

9. F. Huth, A. Govyadinov, S. Amarie, W. Nuansing, F. Keilmann, and R. Hillenbrand, "Nano-FTIR Absorption Spectroscopy of Molecular Fingerprints at 20 nm Spatial Resolution," Nano Letters **12**, 3973–3978 (2012).